공학박사학위논문

시간-주파수 기법을 활용한 변속 조건 유성기어의 고장 진단 기법 개발

Fault Diagnostics of Planetary Gears under Variable-speed Conditions Using Time-frequency Analysis

2019 년 8 월

서울대학교 대학원

기계항공공학부

박 정 호

Abstract

Fault Diagnostics of Planetary Gears under Variable-speed Conditions Using Time-frequency Analysis

Jungho Park
Department of Mechanical and Aerospace Engineering
The Graduate School
Seoul National University

Unexpected failures of a planetary gear may result in substantial economic losses and safety problems. Therefore, extensive prior studies have been performed to develop diagnostic methods for planetary gears. However, most of the studies assumed that the planetary gears operate under constant speed condition although many planetary gears in practical application rotate under variable speeds. Therefore, in this dissertation, fault diagnosis methods are developed for planetary gears under variable-speed conditions. In developing the methods, time-frequency analysis is used to reveal time-varying spectral behaviors of planetary gear vibration signals. However, there are several challenges in developing the fault diagnosis methods for planetary gears under variable speeds: 1) fault sensitivity, 2) computation time, and 3) complex speed profile. To cope with these challenges, this dissertation is composed of three research thrusts. The first thrust proposes a fault diagnosis method with enhanced sensitivity. The method could improve fault sensitivity of the diagnostic method by minimizing effects from variable-speed conditions using the time-frequency analysis. Further, the faulty signals in the time-frequency analysis are enhanced in the developed method. Next, the second research thrust presents a time-efficient fault diagnosis method. In the method, time-efficient time-frequency analysis is used to reduce computation time. However, the fault sensitivity is inherently reduced by using the time-efficient time-frequency analysis. Therefore, in the proposed method, the reduced fault sensitivity from the time-efficient time-frequency analysis is compensated by utilizing characteristics of signal and system. Finally, the third research thrust develops an image-based fault feature, which could extract fault-related characteristics independent of speed profiles. In the method, only faulty components are exploited from the time-frequency image data. The feature is independent of other components using the image analysis technique. Therefore, the proposed method could be applied to planetary gears under complex speed profiles. Validity of the proposed methods is demonstrated using planetary gears of simulation and experiment signals. Each developed method could be used for planetary gears under variable-speed conditions for their use, i.e., fault sensitivity, time-efficiency, and complex speed profiles.

Keywords: Fault diagnosis
Planetary gear
Variable speed
Time-frequency analysis
Signal processing
Prognostics and health management

Student Number: 2012-23166

Table of Contents

List of Tables

List of Figures

Nomenclatures

A_n	Amplitude coefficient of the random noise
A_r	Amplitude coefficient for the resonance vibration
A_v	Amplitude coefficient due to variable-speed conditions
D	Diameter
$E[\cdot]$	Expectation
ER	Energy residual
F_{jk}	Fourier coefficient for the *k*th harmonic of the *j*th planet gear dynamic force
$GP(\cdot,\cdot)$	Gaussian process
$\boldsymbol{I}$	Identity matrix
$\boldsymbol{K}(\boldsymbol{t}, \boldsymbol{t})$	Covariance function for vector
P	Planet gear number
M_s	Whole number of scale parameters
N	Number of observation
N_s, N_e	Starting and ending numbers of the sequence for the selected frequency range
P	Planet gear number
STFT	STFT coefficient
$\overline{\mathrm{STFT}}_{\mathrm{sel.}}$	Selectively averaged STFT coefficient
T_c	Period of a carrier in a planet gear
U_j	Unit step function in the *j*th planet gear considering the effect of the transducer
WT	Wavelet coefficient
$\overline{W}_j$	Coefficient of the *j*th planet weighting functions for unequal load sharing in the carrier and gear manufacturing error
$Y(t)$	Stochastic process
Z_{sun}, Z_{planet}, Z_{ring}	Sun, planet, and ring gear tooth number

$\mathcal{D}$	Noisy observation
a_i	ith data sample
$f(t)$	Time-domain signal
f_n	Resonance frequency
g	Window function
$k(t,\ t')$	Covariance function
$m(t)$	Mean function
r	Noncoherent random noise
s	Scale parameter
t	Time
$\boldsymbol{t}$	Time vector
u	Translation parameter
v	Vibration signal
v_j	Vibration signals from the jth planet gear
w	Noise
wt	Wavelet coefficient
$\overline{wt}$	Averaged wavelet coefficient
y	Time-domain signal
$\boldsymbol{y}$	Time-domain signal vector
δ_{ij}	Kronecker delta function
σ	Standard deviation
σ_f and σ_t	Hyper-parameters of Gaussian process
ϕ_j	Planet position angle at the jth planet
σ_w	Standard deviation of noise
μ	Mean
$\psi(t)$	Wavelet function

ω_c	Angular carrier velocity

Chapter 1

Introduction

1.1 Motivation

Planetary gears are widely used in many engineering applications, such as wind turbines, excavators, industrial robots, and helicopter transmission systems. As multiple planet gears can share a load, a planetary gear has a unique advantage in systems, where the intensity of transmitted loads is extremely high. Therefore, planetary gears are usually exposed to severe loading conditions, which could lead to failures such as fatigue crack and pitting [1]. For example, 59.4% and 19.1% of the whole failures in wind turbines and helicopter transmission are from the gearbox failures [2, 3]. Unexpected failures of a gear may result in substantial economic losses and safety problems. Thus, fault detection and diagnosis for planetary gears has received significant attention in recent decades. Most currently available techniques were developed by analyzing data from either vibration sensors or acoustic emission (AE) transducers. In addition, other fault diagnosis techniques that used different physical quantities than acceleration, such as strain, acoustic emission, or transmission error signals, were also conducted [4-7].

However, previous studies have mainly focused on fault diagnosis under constant speed conditions, despite the fact that many practical applications operate under variable speeds [8-10]. To date, studies on fault diagnosis methods for planetary gears under variable speeds are very limited. Recently, a signal selection method based on two order-tracking techniques (i.e., the computed order tracking and the Vold-Kalman filter order tracking [11]), was developed to deal with diagnosing planetary gear faults under non-stationary conditions. However, those methods that are based on order-tracking techniques required synchronized angular information in addition to acceleration signals. This necessitates measurement devices other than accelerometers and requires additional signal processing.

Thus, this doctoral dissertation aims at developing fault diagnosis methods for planetary gears under variable-speed conditions that uses only acceleration signals. In this regard, time-frequency analysis is exploited to observe time-varying spectral behaviors of the vibration signals. The previous studies that uses time-frequency analysis for fault diagnosis have several drawbacks in their application to acceleration signals of the planetary gear. First, fault sensitivity values of the previous methods could be limited. Previous techniques simply distinguish between normal and faulty states using time-frequency coefficients. Therefore, the methods could not effectively highlight the fault features represented on the time-frequency axis. Second, the previous techniques could require huge computation time. For example, wavelet transform often needs a lengthy computation time due to its high resolution at high frequency regions. Third, the previous techniques cannot be applied to complex speed profiles. The effects of speed profiles on the fault diagnosis methods are minimized in the previous techniques. However, the performance of the previous method could be limited if the system operates under complex speed profiles.

1.2 Research Scope and Overview

This doctoral dissertation thus aims at developing three essential techniques for fault diagnosis of the planetary gears under variable-speed conditions: (1) Research Thrust 1 – positive energy residual (PER) method for enhance fault sensitivity by minimizing effects of variable-speed conditions; (2) Research Thrust 2 – variance of energy residual (VER) method for computational efficiency using time-efficient time-frequency analysis; and (3) Research Thrust 3 – image-based fault feature for complex speed profiles.

Research Thrust 1: Positive energy residual (PER) method for enhanced fault sensitivity by minimizing effects of variable-speed conditions

Research Thrust 1 proposes a positive energy residual (PER) method, for fault diagnosis of planetary gears under variable-speed conditions with enhanced sensitivity. The proposed PER algorithm is based on two techniques, the wavelet transform (WT) and the Gaussian process (GP), which are used to remove the variability of the signals while extracting the faulty signals. Further, a fault feature is presented that is able to effectively quantify the characteristics of faulty signals. The performance of the proposed method is demonstrated using two case studies: vibration signals from a simulation model and vibration signals from a real test-bed.

A comparison study with other methods, WT and energy residual (ER), is also presented to clarify the performance of the proposed PER algorithm.

Research Thrust 2: Variance of energy residual (VER) method for computational efficiency using time-efficient time-frequency analysis

Research Thrust 2 proposes a variance of energy residual (VER) method for more time efficiency based on time-efficient time-frequency analysis. The proposed VER method offers the potential to reduce computation time by using short-time Fourier transform (STFT) instead of other time-frequency techniques. Then, GP technique is used in the method similarly with the PER method. In addition, system and signal characteristics are exploited to compensate fault sensitivity, which is reduced due to STFT. To demonstrate the performance of the proposed VER method, we calculate the fault sensitivity and computation time of the VER method using both simulation and experimental signals.

Research Thrust 3: Image-based fault feature for complex speed profiles

Research Thrust 3 proposes an image-based fault feature, which is independent of speed conditions. Therefore, the feature could be applied to planetary gears under complex speed profiles. First, time-frequency analysis is performed using vibration signals of normal and fault planetary gears. Then, 2-dimensional Fourier transform is used to represent faulty behaviors in time-frequency data. In the spatial frequency domain, which is results of 2-D FT, the vertical lines of time-frequency image data are transformed in the horizontal center components. Finally, mean square values are calculated in the horizontal center components from spatial frequency domain to quantify faulty severity. The fault feature is also validated using the simulation model and experiment signals of the planetary gear.

1.3 Dissertation Layout

The layout of this doctoral dissertation is organized as follows. Chapter 2 reviews the literature regarding fault diagnosis methods for the planetary gear. Chapter 3 describes the data used for validation of each proposed research thrust. Chapter 4 proposes a positive energy residual (PER) method to enhance fault sensitivity (Research Thrust 1). Chapter 5 presents a variance of energy residual (VER) method for time-efficient fault diagnosis method. (Research Thrust 2). Chapter 6 addresses an image-based fault feature for complex speed profiles (Research Thrust 3). Then, Chapter 7 summarizes the dissertation with its contributions and suggested future research.

Chapter 2

Literature Review

This chapter intends to provide previous studies about fault diagnosis techniques of planetary gears. First, I review the fault diagnosis methods for the gears under constant condition. Then, the limitations of the previous methods in applying to the variable speed cases are presented. Next, fault diagnosis methods for the planetary gears under variable-speed conditions are investigated. I also summarize the previous health data that are used to quantify health states of planetary gears. Finally, we discuss limitations of the previous studies, and present how each research thrust is presented in the following sections.

2.1. Fault Diagnosis of a Planetary Gear under the Constant-speed Conditions

Previously, many studies have been conducted to diagnose the faults of the gear systems under constant-speed conditions [12-17]. First, fault diagnosis methods were developed using time-domain signals for nomal and two different types of faults as shown in Figure 2-1 [12]. In the figure, normal and two different types of faults (distributed and local) signals are shown. We could differentiate faulty states from the normal state if there are small noise sources. Wang and Wong [13] developed fault diagnosis of the gear using an autoregressive (AR) model in the time-domain. An optimal sinusoidal modelling technique was developed based on a batch learning of the least squares techniques to simulate the time-domain gear mesh signals [14]. A minimum entropy deconvolution (MED) tehcnique was further combined with the previous AR model to signify the fault signals in the gear signals by Endo and Randall [15]. The MED technique could enhance the fault signals by using phase information from higher-order statistical characteristics.

However, if the time-domain signals are covered by severe noises, as can be seen in the second row of the figure, we could not differentiate the faulty states from the normal state. Therefore, many methods have been developed using the vibration

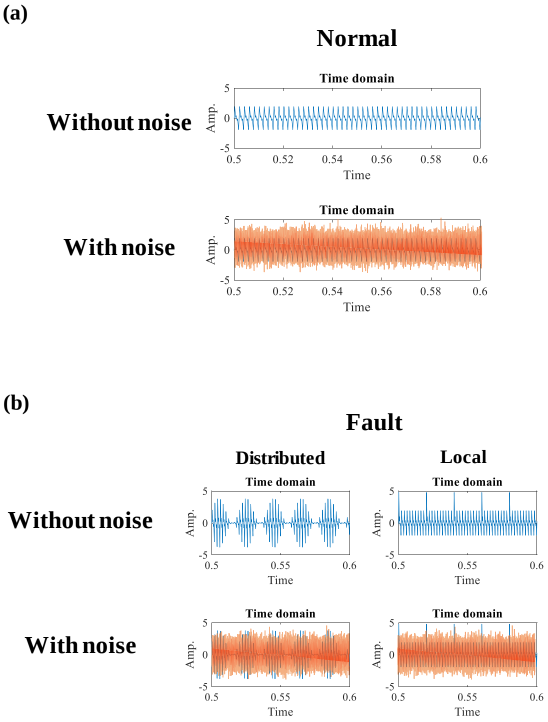

Figure 2-1 Fault diagnosis of gears under constant-speed conditions using time-domain data: (a) Normal signals, and (b) faulty signals

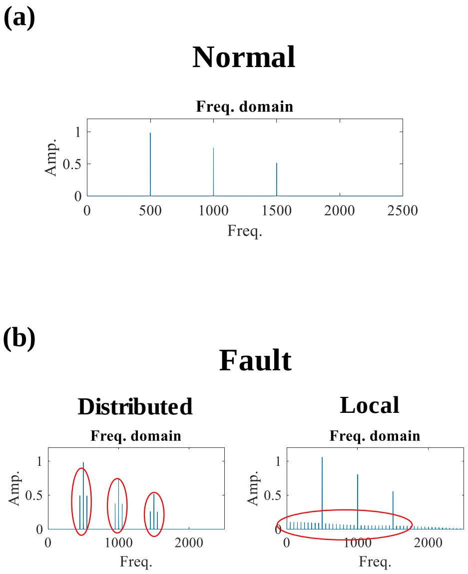

Figure 2-2 Fault diagnosis of gears under constant-speed conditions using frequency-domain data: (a) Normal signals, and (b) faulty signals

signals of the gear system in the frequency domain. Figure 2-2 shows the normal and two different types of faults in the frequency domain.

As can be seen, we could observe side-band behaviors, or other frequency components other than normal gear signals in the frequency domain. Mcfadden and Smith [18] investigated the side-band behaviors of the planetary gear, which were induced by modulated vibration characteristics. Bi et al. [19] developed a fault feature named slice spectral correlation density (SSCD). The feature could quantify the faulty vibration behaviors from amplitude- and frequency modulation. Ratios of rotational-harmonic amplitudes in the frequency domain of the vibration signals were proposed [20]. The method could detect the fault in the ring gear tooth in the planetary gear by considering noises and manufacturing errors. Lei et al. developed the normalized summation of positive amplitudes of the difference spectrum between the unknown signal and the healthy signal (NSDS) in the frequency domain to sensitively diagnose the faults in the planetary gear. Mark investigated the fault diagnostic method that could minimize the effects of transducers and transmission path [21]. However, the previous methods were basically only applicable to the gear system under constant-speed conditions, and could not be applied to the planetary gears under variable-speed condition because the frequency-domain signals would be changing continuously at each time in varying speed conditions.

There have been also other methods that use other various signal processing methods using vibration signals [22-35]. Zhang et al. used a blind deconvolution denosing method to diagnose the fault of the gear in the helicopter [22]. Barszcz and Randall introduced a spectral kurtosis technique for planetary gear fault detection [23]. The technique could find the spectral band that contain the most impulsive signals. Zimroz and Bartelmus studied cyclostionarity of the planetary gear vibration signals to develop a diagnostic feature [24]. Lei et al. investigated use of a stochastic resonance technique in the field of diagnosing the planetary gear faults [25].

Simulation models of the planetary gear also have been used to investigate dynamic behaviors of the planetary gear, and extract fault-related feature [1, 36-41]. Parra and Vicuna compared the two methods, phenomenological model and lumped parameter model, used for modelling vibration signals of the planetary gear [36]. Liang et al. studied the effects of crack in the gear tooth for the gear mesh stiffness [37]. Feng et al. developed the models for the vibration signals of the planetary gear under faulty conditions [38]. Chen and Shao developed a simulation model to investigate a planetary gear with tooth root crack in the ring gear [39].

Additionally, other physical quantities like strain, displacement, current, and acoustic emission signals have been used to diagnose the fault of the planetary gear [4, 5, 42-45]. Yoon et al. analyzed strain sensor signals, which is free from modulation effects due to planetary gear transmission effects [4]. Park et al. constructed a dynamic model of the planetary gear, and calculated the transmission error based on rotational displacement of the planetary gear. They could find that the transmission error signals could detect fault of the planet gear [5]. Induction motor current signals were also used to avoid modulated behaviors in the planetary gears [42]. Acoustic emission signals were used to incipient faults of the wind turbine gearbox based on the time of arrival (TOA) [43].

2.2. Fault Diagnosis of a Planetary Gear under the Variable-speed Conditions

This section will review the fault diagnosis techniques developed for the planetary gears under variable-speed conditions. As mentioned in the first section, the previous frequency-domain method could not be used for time-varying vibration signals of the planetary gears. Therefore, the fault diagnosis methods have been developed so that variability in the vibration signals from the variable speed could be reduced. In this section, 1) angular resampling, 2) time-frequency analysis, and 3) image-based approach will be reviewed.

2.2.1. Angular Resampling

This sections will review the previous studies about the angular resampling technique. Figure 2-3 shows the basic principle of the angular resampling technique. Figure 2-3(a) show how the angle and vibration shows when the speed of the gear is increasing.

As can be seen, the angular speed is getting larger, and the periods in the vibration is getting shorter. Basically, the angle and vibration values are sampled by the encoder and accelerometer at the same time interval . The idea of the angular resampling is to resample the measured data at the same angle. After resampling, we could observe how the vibration signals behave in the angular domain.

Then, many studies have been performed based on the angular resampling techniques [46-50]. He et al. developed a new order tracking method for angular resampling based on discrete spectrum correction [46]. The method could improve

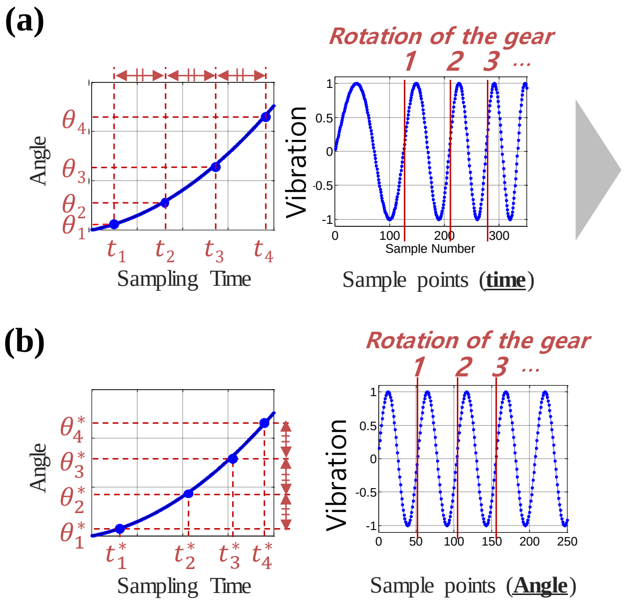

Figure 2-3 Transformation of vibration data using angular resampling: (a) before and (b) after angular resample

robustness of the previous using the meshing frequency characteristics of the planetary gearbox in the wind turbine. A signal selection method based on two order-tracking techniques (i.e., the computed order tracking and the Vold-Kalman filter order tracking [47]), was developed to deal with diagnosing planetary gear faults under non-stationary conditions. The time-domain features calculated after order-tracking techniques showed about an eight-fold difference for the tooth wear case. Li et al. extracted fault features using signal sparse decomposition and order tracking [48]. However, those methods that are based on order-tracking techniques using angular resampling required synchronized angular information in addition to acceleration signals. This necessitates measurement devices other than accelerometers and requires additional signal processing

2.2.2. Time-frequency Analysis

In this chapter, I will review the time-frequency analysis techniques used for fault diagnosis of the planetary gear under variable-speed conditions. Figure 2-4 shows the basic principle of the time-frequency analysis. There are two different time-varying vibration signals in the left hand sided of the figure. In the upper one, 50 Hz of the signals come first, and 400 Hz of the signals come later. In the lower one, 400 Hz of the signals come first, and 50 Hz of the signals come later. In the frequency analysis which can be observed by right upper figure, the two different signals cannot be differentiated, because the frequency analysis only could quantify the frequency component in the signals. However, In the time-frequency analysis which can be observed by right lower figure, we could also observe how each frequency components behave along the time. Therefore, there have been several attempts to

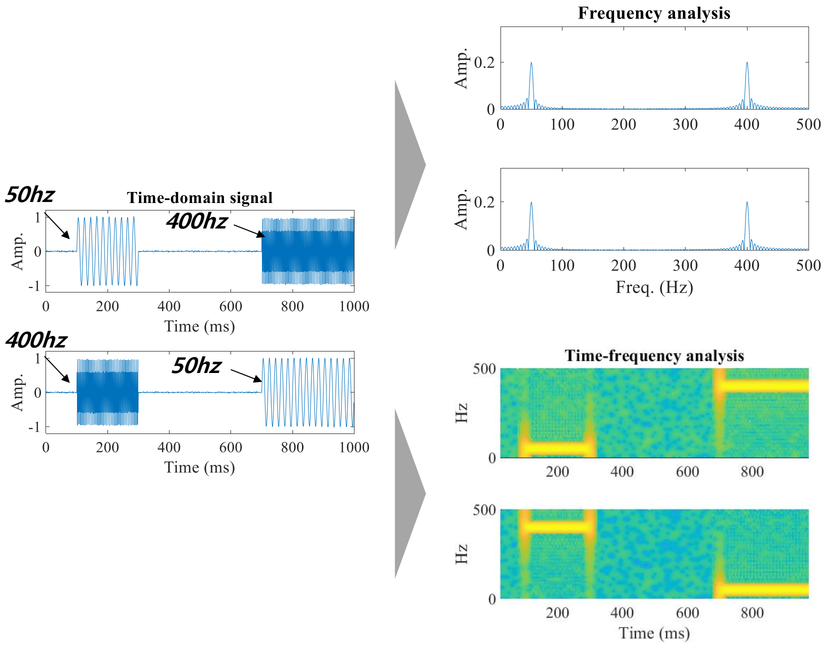

Figure 2-4 Frequency analysis and Time-frequency analysis for the two different time-varying vibration signals

diagnose the fault of the planetary gear under variable-speed conditions using time-frequency analysis [1, 33, 51-62]. Feng and Liang exploited adaptive optimal kernel method to show time-frequency behaviors of the faulty planetary gear [51]. The method showed better time-frequency resolution than previous approaches, and was free from cross-term. The method was validated using planetary gears in experiment setup and a real wind turbine. Chen and Feng used the torsional vibration signals for time-frequency analysis, and observed resonance regions to find faulty characteristic component in the time-frequency domain [52]. Morelet wavelet and singular value decomposition (SVD) were combined to extract fault features of a wind turbine planetary gearbox [53]. However, huge computation time is usually required for the wavelet method. This is especially true when WT is performed for vibration data with wider frequency ranges. Wide frequency ranges are mandatory for successful fault detection; thus, use of WT as part of the PER method requires huge computation power [63].

2.2.3. Image-based Approach

There have been fault detection methods that consider 2-dimensional time-frequency coefficients as image data. These approaches particularly have been developed in medical applications for human disease detection [64-69]. Boashash et al. analyzed nonstationary electroencephalogram (EEG) signals using time-frequency image data from Wigner-Ville distribution (WVD), Gaussian Kernel distribution (GKD), and modified-B distribution (MBD). In the image data, morphometric features were proposed based on the geometric shapes of the data [64]. Boashash and Ouelha combined statistical features obtained from time-frequency image data with machine learning techniques [65]. Then, they used the developed method to detect abnormality in the newborn EEG seizure case. Boashash et al. [66] also used the texture-based features from the time-frequency image data for the EEG seizure detection of the newborn. Figures 2-5 (a) and (b) show how the texture-based features, Haralick and local binary pattern (LBP) [70, 71].

In the Haralick feature, the technique first transforms the data into 4 levels of data. Then, gray-level co-occurrence matrix (GLCM) is constructed based on the adjacent values of each elements in the 4-level image data. After normalizing the GLCM matrix, the Haralick features could be calculated. For the LBP feature, the image data are transformed into zero or one after comparing the magnitudes of each adjacent values of image data with the center values of matrix. Then, the center values are transformed based on binary calculation of the each adjacent. For the LBP feature, the image data are transformed into zero or one after comparing the magnitudes of each adjacent values of image data with the center values of matrix. Then, the center values are transformed based on binary calculation of the each adjacent values. Then various LBP features could be derived based on histogram of

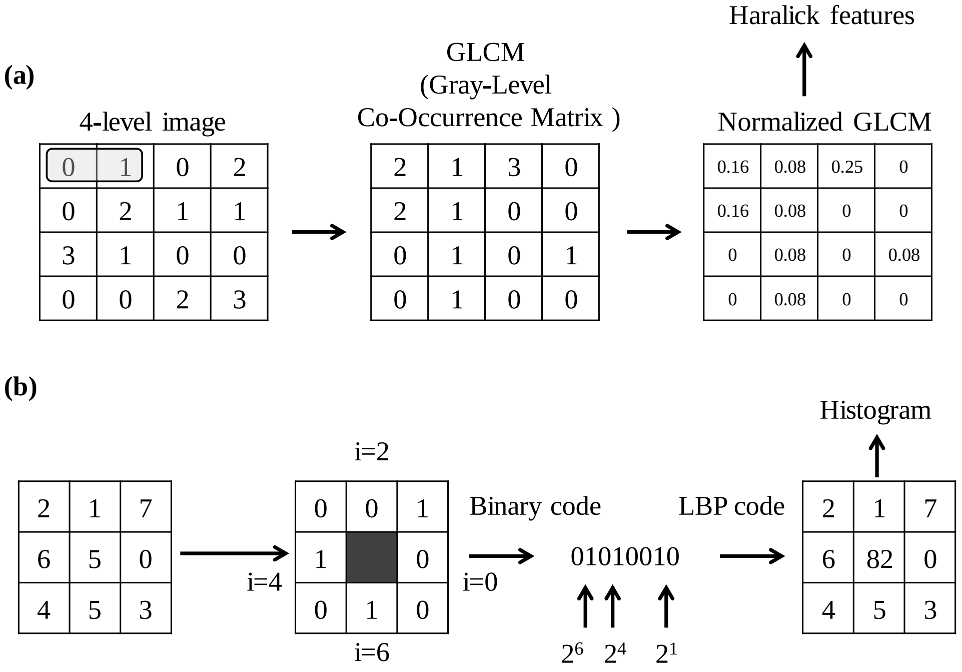

Figure 2-5 Basic principles of the texture-based features, (a) Haralick and (b) local binary pattern (LBP)

the transformed data.

Above-mentioned methods are basically based on extracting features from the image data of the time-frequency analysis, like short-time Fourier transform (STFT), wavelet transform (WT), and WVD. Recently, deep learning techniques have shown good performances in image data classification [72-80]. In the methods, the user does not have to extract features based on the domain knowledge, and the features could be calculated autonomously during executing the method. Therefore, the fault diagnosis methods using the techniques have been extensively used for fault diagnosis of the planetary gears and other rotating machinery [81-83]. Zhao et al. used deep residual networks (DRN) and dynamically weighted wavelet coefficients (DWWC) for fault diagnosis of planetary gears [81]. In the method, they could improve the diagnostic performance, and find the frequency zones with the most faulty information. Oh et al. used deep belief networks with vibration image measured from journal bearings of rotor systems [82]. In the method, they could improve diagnostic accuracy, and the fault features were extracted automatically. A Gaussian-Bernoulli deep Boltzmann machine (GDBM) was also employed for time-frequency data of the vibration signals from the gearboxes [83]. Especially, convolutional neural networks (CNN) have been widely used for time-frequency image data because the technique is known to show good classification results in image data [31, 84, 85]. Figure 2-6 shows the basic principles of the CNN. The most important property of the CNN is that it uses convolution operation for the image data. The feature maps could be constructed from convolution process of the image data. Then, the sizes of the feature maps could be reduced by subsampling. By repeating these procedures, the output of the CNN could be calculated as can be seen

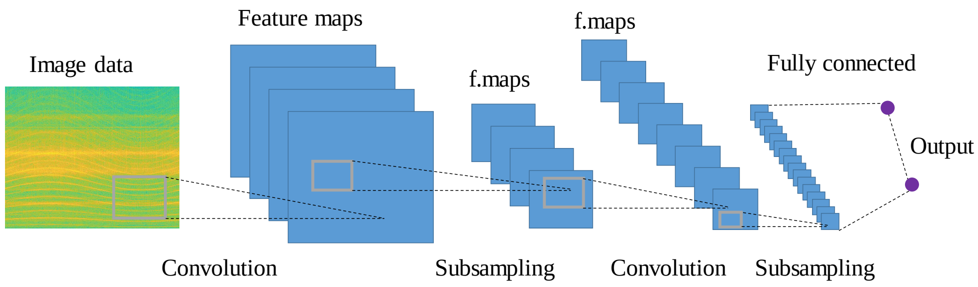

Figure 2-6 Basic principles of convolutional neural networks (CNN)

in the Figure 2-6. Jing et al. developed a CNN based feature learning method using time-frequency image data of the gearbox vibration signals [84]. They compared the effectiveness of the proposed method with previous features from time-domain, frequency-domain, and wavelet method, and confirmed that the proposed method showed the best performance. And, an adaptive data fusion method was developed for multi-sensor data based-on deep convolutional neural networks (DCNN) [85]. The method, could extract optimal fault features without domain knowledge and human labor. Liu et al. combined variational mode decomposition (VMD) with the CNN for fault feature extraction of the planetary gear [31]. The method could not only enhance fault sensitivity, but also identify different types of faults in the planetary gear. However, most of the methods could not present exact physical relationship of the proposed fault features with actual faults. Although there have been several approaches using simulation models of the planetary gears under variable-speed conditions, physical meanings of the faults were difficult to reveal under the variable-speed conditions [86-92].

2.3. Health Data

Appropriate selection of health data is crucial in the field of prognostics and health management [93-100]. There have been many attempts to summarize the health data employed for fault diagnosis of the gears [101-105]. In this section, I will review the widely used health data, which are used to quantify health states of the rotating machinery including planetary gears.

RMS

The RMS is well-known for quantifying the overall degradation degree of the system in the time domain , albeit insensitive to incipient failure [102]. The measure could quantify overall kinetic energy level in the measured vibration signals, and can be expressed as below equation,

$$\mathrm{RMS} = \sqrt{\frac{1}{n}\sum_{i=1}^{n} v_i^2} \tag{2.1}$$

where v_i is the *i*th time data point, n is the total number of data samples.

Kurtosis

The kurtosis measures the peakedness of a distribution with respect to normal distribution and the tail thickness [106]. Kurtosis is used to show degree of the vibration signal’s deviation from the mean value due to the fault of the gear. The kurtosis values could be calculated as below equation,

$$\text{Kurtosis} = \frac{\sum_{i=1}^{n}[v_i - \mu]^4}{n \times (\sigma^2)^2} \tag{2.2}$$

where μ is the mean of the data, σ is the standard deviation of the data.

<u>Frequency center (FC)</u>

FC calculates the mean of the frequency component and is used to observe the transition of the main frequency components. As gear faults are known to induce phase modulation [107], the FC can show how the faults affect the frequency components of the system. We can express FC as

$$\text{FC} = \frac{\int_0^{+\infty} f \cdot s(f) df}{\int_0^{+\infty} s(f) df} \tag{2.3}$$

where f is the frequency of the data, $s(f)$ is the amplitude of the frequency components.

<u>Figure-of-merit zero (FM0)</u>

The FM0 is calculated by dividing the peak-to-peak (P2P) value of the signals by the sum of the amplitude of the gear mesh frequency. The FM0 is known to detect localized faults in the measured signal [108]. The FM0 indicates the increase of magnitude of TE by calculating P2P values and the reduction in amplitude of the main frequency due to the fault signal. It can be formulated as

$$\mathrm{FM0} = \frac{\mathrm{P2P}}{\sum_{j=1}^{l} s(f_i^g)} \tag{2.4}$$

where P2P is the peak-to-peak value of the data, f_i^g is gear mesh frequency and its jth harmonics, and l is the total number of harmonics.

Variance

The variance value could quantify the spread of the data from the mean values. The equation for the variance value for the data v_i

$$\text{variance} = \frac{1}{n-1}\sum_{i=1}^{n} |v_i - \mu|^2 \tag{2.5}$$

It can be treated as the second statistical moment of the probability distribution.

***SER* (Sideband energy ratio)**

Sideband energy ratio (*SER*) is defined to quantify the faulty components of the spectrum of the vibration signals, which are represented in vicinity of the gear main harmonics. The health datum can be expressed as

$$\mathrm{SER} = \frac{\sum_{i=1}^{N_{sideband}} A(s_i^{f1})}{A(f_1)} \tag{2.6}$$

where $A(s_i^{\mathrm{f1}})$ is amplitude of i^{th} sideband of fundamental gear mesh frequency, $N_{sidebands}$ is the number of sidebands. The SER have been widely used to detect faults in the wind turbine gearboxes [109].

2.4. Summary and Discussion

First of all, in this dissertation, I focus on fault diagnostics of planetary gears under variable -speed conditions. In real-world situations, planetary gears are usually operated under varable-speed conditions. Therefore, I intend to develop fault diagnostic methods that can be also applied to variable-speed conditions. In addition, the method would not need other measurement devices than acceleration signals. Although many diagnostics methods based on the angular resampling technique showed good performance, additional devices are need to measure angular data, and they also need additional signal processing. In this context, we focus on below three points.

Fault sensitivity enhancement by minimizing effects of variable-speed conditions

The angular resampling technique could reduce the effects of variable-speed in the measured vibration signals by resampling the data in the angular domain as mentioned in 2.2.1. However, the use of angular data is only possible by using additional measurement devices. Although time-frequency analysis could be used to investigate time-varying behaviors of the vibration signals, fault sensitivity of the method could be limited when the effects of variable speed in the results of the time-frequency analysis are not removed [51, 52]. Therefore, in this dissertation, I intend to minimize the effects of variable speed by only using vibration signals for fault diagnosis of the planetary gears under variable-speed conditions. In this regard, we could enhance fault sensitivity of the diagnostic method for the planetary gear under variable-speed conditions. In addition, we would not need any other measurement devices other than an accelerometer.

Time efficiency of the diagnostic method

As mentioned in Section 2.2.2, the use of time-frequency analysis for vibration data often results in huge computation time, and it could not be used for real-time monitoring [63]. In this regard, time efficiency of the diagnostic method is also an important issue. However, when we choose the other time-frequency methods to reduce computation time, the fault sensitivity could be reduced [110]. Therefore, in this dissertation, I intend to develop time-efficient diagnostic method for planetary gears under variable-speed conditions while compensating reduced fault sensitivity by exploiting signal and system characteristics.

Image-based features for complex speed profiles

In Section 2.2.3, I reviewed the image-based method that used time-frequency analysis. First, image-based features have been developed for medical applications. Although they showed good performance in the medical field, the features could be limited to fault diagnosis of the planetary gears because they do not fully utilize faulty characteristics of the planetary gears. In addition, recently, deep learning techniques have been actively employed to train the fault features of the time-frequency image data. Especially, the CNN technique has been extensively used when the image data are used for training data, as the method is known for its good classification ability for image data. However, the deep learning techniques do not have close physical relationship with faulty characteristics of the planetary gear. In this regard, I will develop an image-based fault feature, which could extract faulty information of the planetary gear. Further, the feature would be independent of speed profiles of the planetary gear, and could be applied to the gear with complex speed profiles.

Chapter 3

Data Description

In this chapter, I will describe the data I used to validate the proposed method. I used the two types of data, simulation data and experiment data. First, I will explain how the simulation model was constructed including planetary gears under normal and faulty states. Then, descriptions about experimental setup for the planetary gear will be presented.

3.1. A Simulation Model for a Planetary Gear

This chapter will explain the details about the simulation models for a planetary gear, which will be used for demonstrating the performance of the proposed methods in this dissertation. The basic parameters of the planetary gear is shown in Table 3-1, and they are same as the ones in the experimental setup, which will be given in the Section 3.2.

Table 3-1 Basic parameters of the planetary gear

Parameter	**Value**
Ring gear tooth number, Z_{ring}	95
Planet gear tooth number, Z_{planet}	31
Sun gear tooth number, Z_{sun}	31
Planet gear number, P	3

3.1.1. A Simulation Model for a Planetary Gear in a Normal State

Figure 3-1 shows the common configuration for measurement of planetary gear vibration. The accelerometer is mounted on the outer ring gear. In this configuration, the measured vibration signals would be modulated like those shown in Figure 3-1(b) because the multiple planet gears pass through the mounted accelerometer. In [111], Inapolat and Kahraman developed a model that simulates the modulated vibration signals of the planetary gear; this is called a phenomenological model. The phenomenological model is able to simulate the actual vibration signals measured from the transducer on the planetary gear; whereas, the lumped-parameter model can only explain the dynamic behaviors of the planetary gear observed by a ground-based reference [36]. Therefore, in this research, we adopted the phenomenological model based on the previous paper.

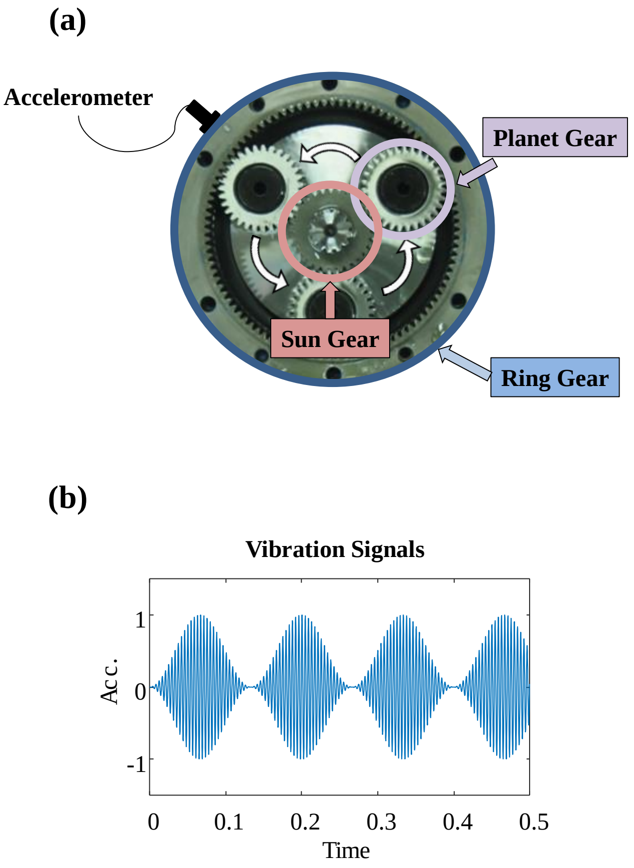

Figure 3-1 (a) A cross-sectional view of a planetary gear with an accelerometer mounted on the ring gear; and (b) vibration signals of the simulation model developed by Inapolat and Kahraman [111]

In the modulated vibration signals, white noise was added to reproduce more realistic signals. The variable-speed condition was given as $(-300(t-3)^2 + 2800)$ rpm of the sun gear rotation as shown in the Figure 3-2. Amplitudes of the vibration signals varied in proportion to a magnitude of speed in this case [112]. Consequently, the equation of the vibration signal of the jth planet $v_j(t)$ is as follows:

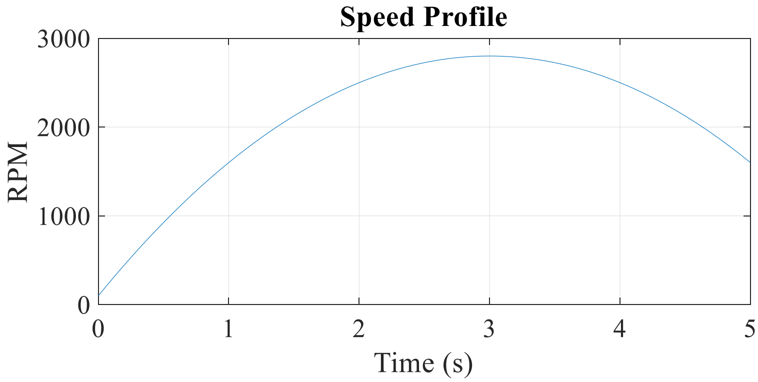

Figure 3-2 The variable speed profile used in the simulation.

$$v_j(t) = A_v(t)\overline{W}_j w\left(t - \frac{\phi_j}{2\pi}T_c\right) U_j(t) \sum_{k=1}^{K} F_{jk} \cos\left(kZ_r\omega_c t + kZ_r\phi_j\right) + A_n r(t) + A_r \cos(2\pi f_n t) \tag{3.1}$$

where A_v, A_n, and A_r are amplitude coefficients for variable-speed conditions, random noise, and resonance vibration; $\overline{W}_j$ is a coefficient of the jth planet weighting function for unequal load sharing in the carrier and gear manufacturing error; $w(t)$ is a window function based on a Hanning function; ϕ_j is a planet position angle at the jth planet; Tc is a period of a carrier in a planet gear; $U_j(t)$ is a unit step function in the jth planet gear considering the effect of a transducer; F_{jk} is a Fourier coefficient for the kth harmonic of the jth planet gear dynamic force; ω_c is an angular carrier velocity; $r(t)$ is noncoherent random noise; and f_n is a resonance frequency. In this study, we assumed that the whole load sharing would be same among the planets, and all $\overline{W}_j$ values were set to 1. The total vibration signal $v(t)$ is then

$$v(t) = \sum_{j=1}^{P} v_j(t) \tag{3.2}$$

where *P* is a planet gear number. More details about the model can be found in [111]. In the model, seven harmonic components were considered. In addition, four levels of planet gear local faults were added to observe the performance of the proposed methods. The resonant frequency of this system was imposed as 10 kHz, and the sampling rate of the vibration signal was 25,000Hz.

3.1.2. A Simulation Model for a Planetary Gear in a Faulty State

There could be planet, sun, ring gear fault types in the planetary gear. Additionally, the fault could happen in the single side of the gear tooth, both sides of the gear tooth, or the fault could be distributed cases [113]. Table 3-2 shows the characteristic faulty frequencies which could happen in the planetary gear. In this dissertation, we assume a planet gear singe fault in the planetary gear.

Table 3-2 Characteristic faulty frequency of the planetary gear

Type		**Frequency**
Planet fault	Single	$f_{\mathrm{planet},1} = \frac{f_{\mathrm{mesh}}}{Z_{\mathrm{planet}}}$
	Double	$f_{\mathrm{planet},2} = 2\frac{f_{\mathrm{mesh}}}{Z_{\mathrm{planet}}}$
	Distributed	$f_{\mathrm{planet,dist.}} = \frac{f_{\mathrm{mesh}}}{Z_{\mathrm{planet}}}$
Sun fault	Single	$f_{\mathrm{sun}} = \frac{f_{\mathrm{mesh}}}{Z_{\mathrm{sun}}} N_{\mathrm{planet}}$
	Distributed	$f_{\mathrm{sun,dist.}} = \frac{f_{\mathrm{mesh}}}{Z_{\mathrm{sun}}}$
Ring fault	Single	$f_{\mathrm{ring}} = \frac{f_{\mathrm{mesh}}}{Z_{\mathrm{ring}}} N_{\mathrm{planet}}$
	Distributed	$f_{\mathrm{ring,dist.}} = \frac{f_{\mathrm{mesh}}}{Z_{\mathrm{ring}}}$

Figure 3-3 shows how the vibration signals are simulated in this study. Figure 3-3(a), (b), and (c) show the vibration signals from 1st, 2nd, and 3rd planet gears indicated with black solid lines in the figure. Although all the gears are meshing with other gears, the measured vibration signals from the accelerometer would be like Figure 3-3(d) due to the signal transfer function of the planetary gear indicated as red dotted line in the figure. Then, I will assume that the 3rd planet gear is a faulty gear. Then, the faulty tooth of the gear would mesh with other gear periodically, and the sequences are marked as red circles as shown in the figure. However, all the faulty signals could be measured by accelerometers due to the signal transfer function. Therefore, only one of the faulty meshes could be measured from the accelerometer. The vibration signals are simulated using this principle, and we assumed four different levels of faults in this cases. Figure 3-4 shows the simulated vibration signals calculated from the described model of normal and four different levels of faults.

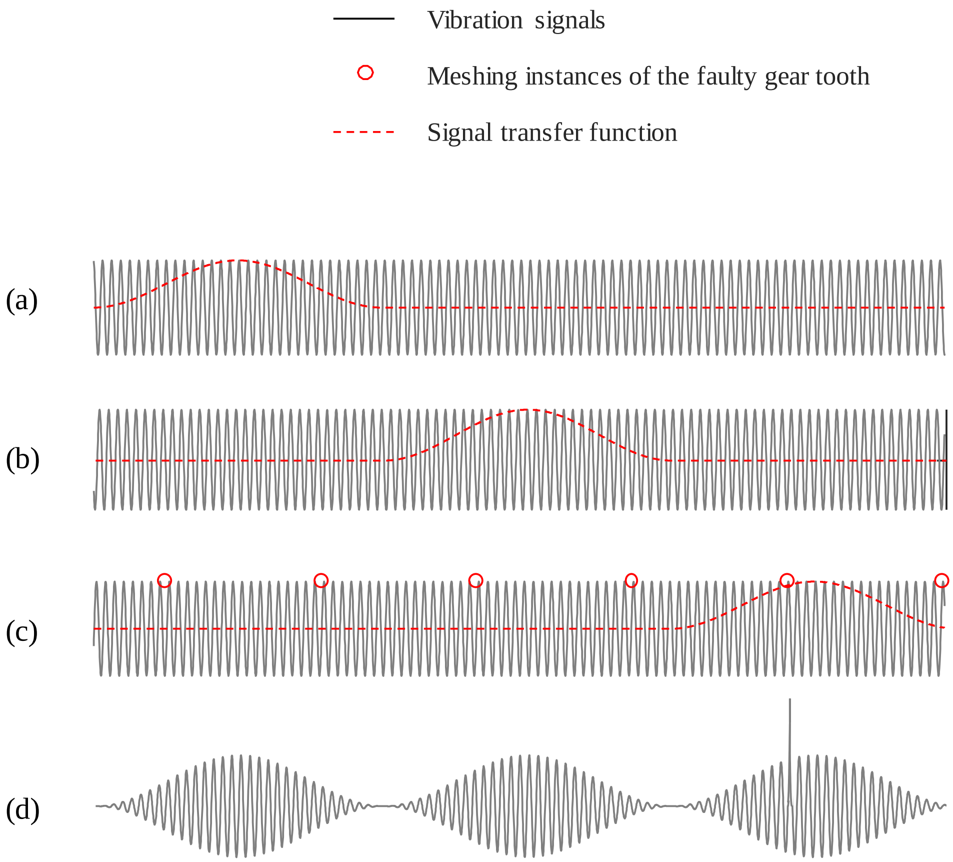

Figure 3-3 Meshing of a single faulty planet gear: (a) 1st planet gear vibration signals, (b) 2nd planet gear vibration signals, (c) 3rd planetary gear vibration signals, and (d) resultant vibration signals measured from an accelerometer

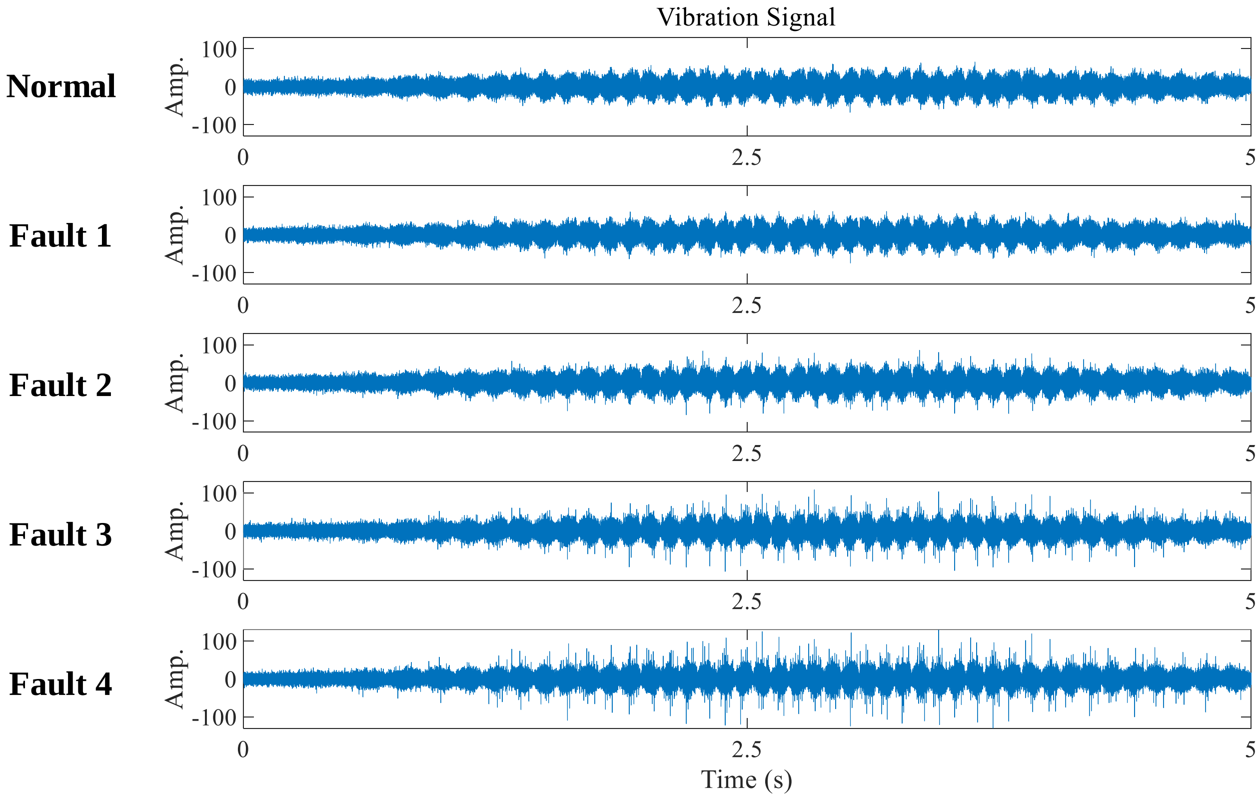

Figure 3-4 Simulated vibration signals in normal and four different levels of faults

3.2. Experimental Setup for a Planetary Gear

This chapter will describe the experiment setup to measure the vibration signals of the planetary gear. The overall configuration of the testbed is shown in Figure 3-5(a) and the cross-section of the target planetary gearbox is shown in Figure 3-5(b). The target for the experiment was a 2nd stage planetary gearbox. The specifications of the planetary gear were same as those in the simulation study, where Z_{sun} is 95, Z_{planet} is 31, Z_{ring} is 31, and P is 3. Three levels of faults were seeded artificially on the planet gear, as shown in Figure 3-6, where the shapes of the faults are semicircles with diameters of 0.75, 1, and 1.25mm, respectively.

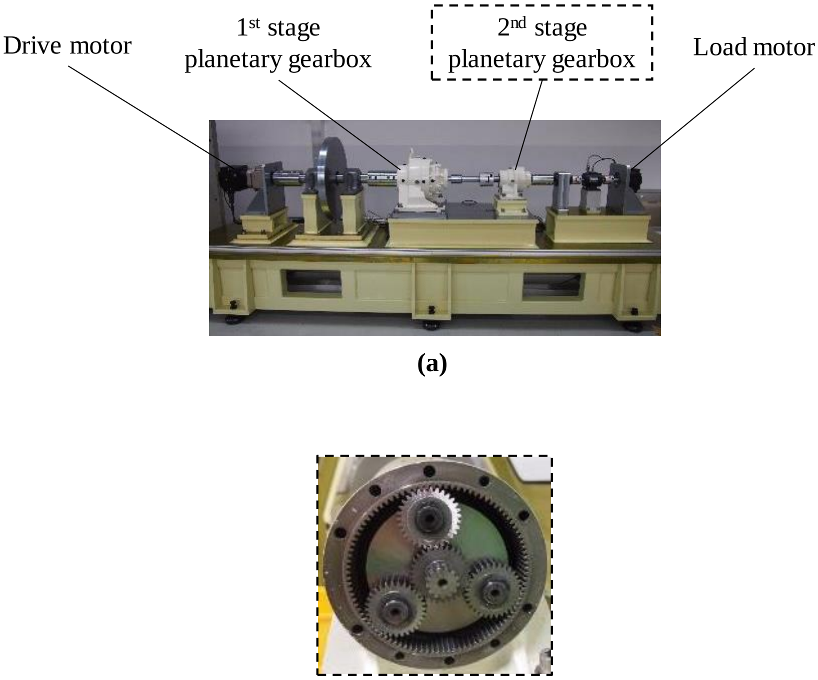

(a)

(b)

Figure 3-5 (a) Overall configuration of the testbed, and (b) the cross-sectional view of the target planetary gearbox (i.e., 2nd stage planetary gearbox)

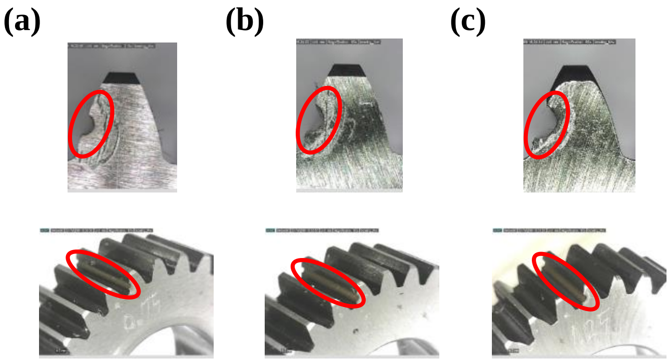

Fault Level 1 (*D*= 0.75mm)

Fault Level 2 (*D*= 1.0mm)

Fault Level 3 (*D*= 1.25mm)

Figure 3-6 Gear tooth profiles for three levels of half-circle-shaped faults: (a) level 1 (D = 0.75mm), (b) level 2 (D = 1.0mm), and level 3 (D = 1.25mm)

In the experiment setting, I measured the acceleration signals 25,600Hz, and the six accelerometers were attached around the planetary gearbox as can be seen in Figure3-7. The accelerometers are mounted on the gearbox using the stud mounting method as can be seen in the Figure 3-8.

Figure 3-9 shows measured vibration signals from the six accelerometers attached to the planetary gearbox from normal and faulty states. The kurtosis ratios between signals of each accelerometers from normal and faulty states are 1.06, 1.01, 1.16, 1.29, 1.10, and 1.15, respectively from 1st to 6th accelerometer. Based on these results, we could find that the 4th accelerometers have the most sensitive results to the gear fault. This results is expected to happen due to transmission path effect in the planetary gear [114].

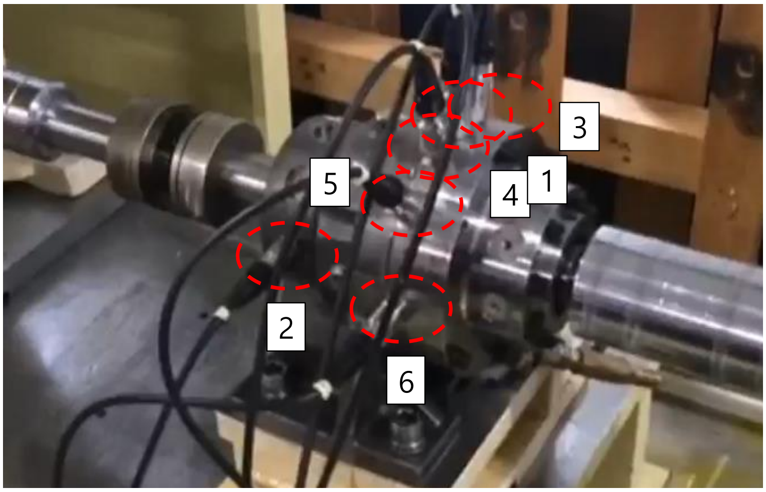

Figure 3-7 Accelerometers attached to the planetary gearbox

(a)

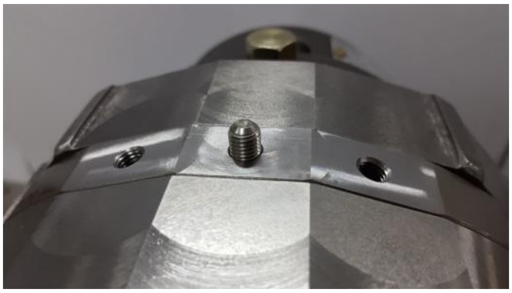

(b)

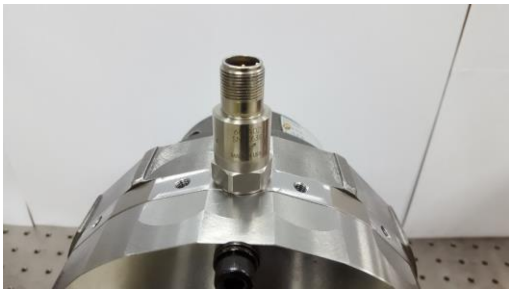

Figure 3-8 (a) Stud mounting of the gearbox, and (b) an accelerometer attached to the gearbox

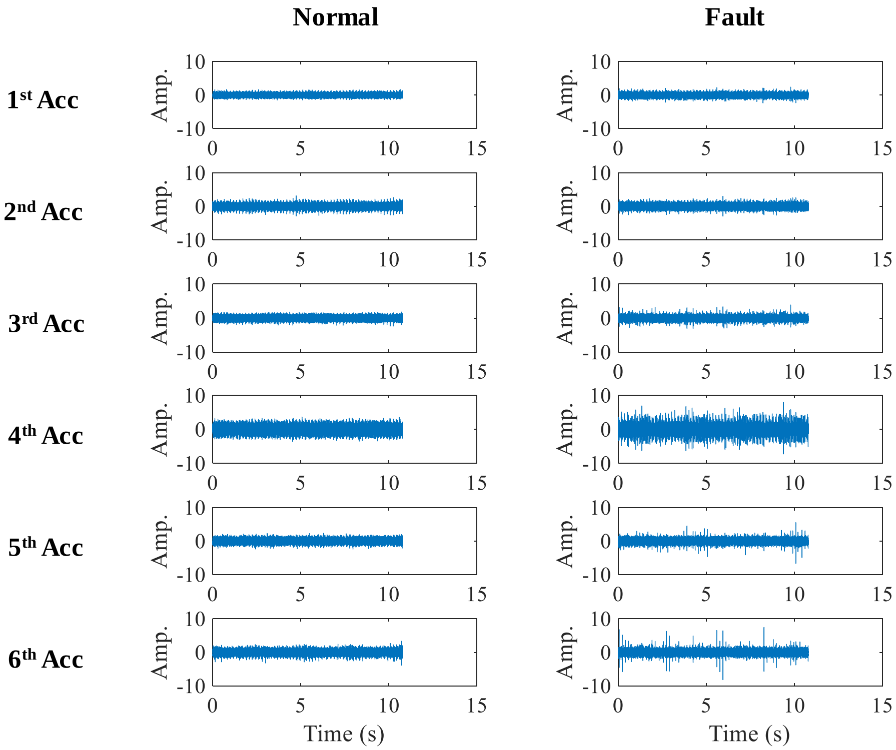

Figure 3-9 Vibration signals from the six accelerometers attached to the planetary gearbox from normal and faulty states

The variable speed profile was considered to validate the proposed method, while the torque and temperature were maintained constant at 4 Nm and 60°C, respectively. Previous literature adopted different speed profiles to validate each method [115-119]. In the variable speed profile, the speed was fluctuating from 1100 to 1500 rpm with a sinusoidal curve with a period of 20 seconds as shown in Figure 3-10. Figure 3-11 shows the measured vibration signals from planetary gears of normal and three different levels of faults.

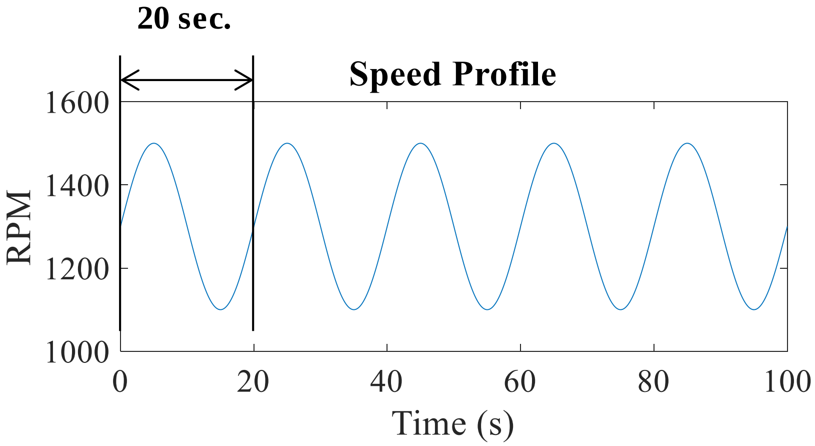

Figure 3-10 The variable-speed profile used in the experiment

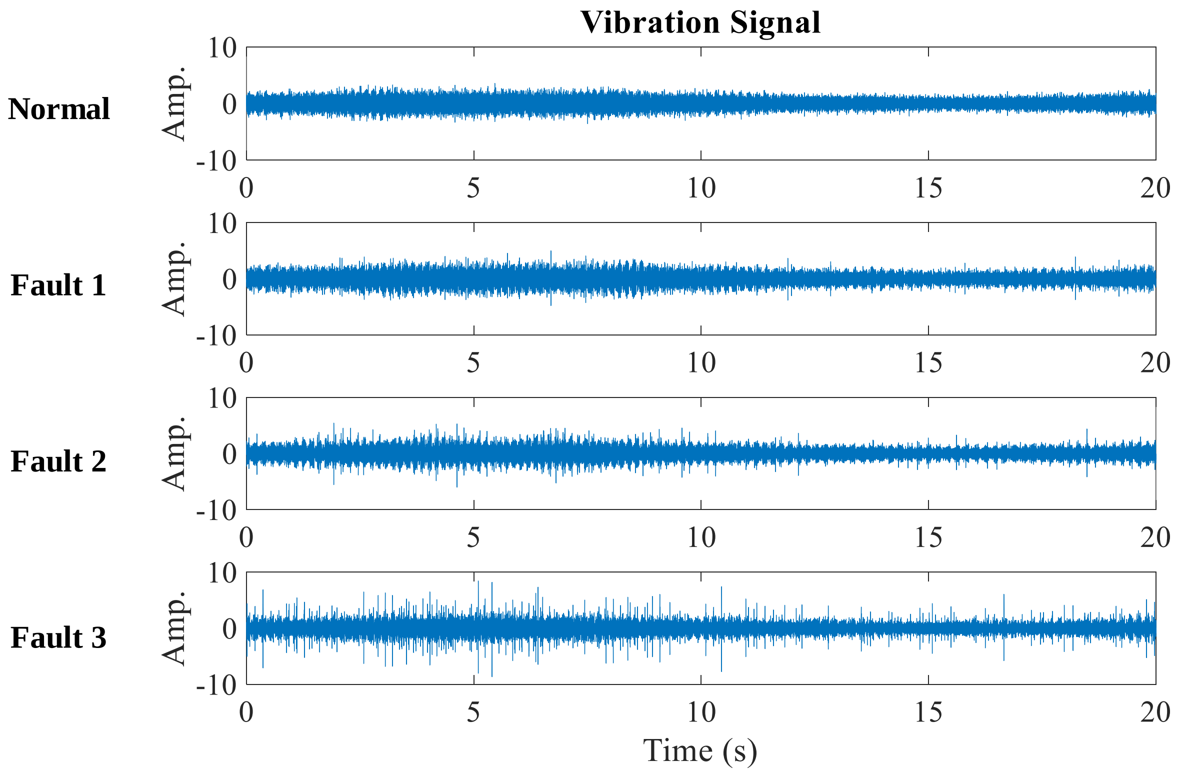

Figure 3-11 Experiment vibration signals in normal and three different levels of faults

Sections of this chapter have been published or submitted as the following journal articles:

1) **J. Park**, M. Hamadache, J. M. Ha, Y. Kim, K. Na, and B. D. Youn, "A positive energy residual (PER) based planetary gear fault detection method under variable speed conditions," *Mechanical Systems and Signal Processing*, vol. 117, pp. 347-360, 2019.

Chapter 4

A Positive Energy Residual (PER) Method for Enhanced Fault Sensitivity

The proposed PER method, which uses only the vibration signals acquired from accelerometers, will be explained in detail in this section. As described in the introduction, the proposed PER method was developed with the aim to detect faults of planetary gears under variable-speed conditions. And, it aims at enhancing fault sensitivity by minimizing the effects from the variable-speed conditions. In this chapter, we first review the wavelet transform (WT), which is one of time-frequency analysis techniques. Next, I will describe the details of the proposed PER method. Then, performance of the proposed method will be demonstrated using two case studies, a simulation model and experiment data. Finally, I will summarize and discuss the results.

4.1. Review of Wavelet Transform and a Gaussian process

In this section, we review the WT and GP regression techniques that we used to develop the new planetary gear fault diagnosis algorithm. First, basic principles of

WT are reviewed. In addition, we investigate previous studies using WT for fault detection and their limitations when applied to variable speed conditions. Next, we explain how a GP is formulated and how it can be used for regression. Then, we describe how GP regression can be used to quantify the statistical quantity in the continuous domain.

4.1.1 Wavelet transform

WT decomposes time-domain signals $v(t)$ at time t, like Fourier transform (FT). While FT uses sinusoidal basis functions in decomposing the signals, WT uses a wave-like function $\psi(t)$ called a wavelet [120]. WT can be expressed as

$$wt(u,s) = \frac{1}{\sqrt{s}}\int v(t)\psi^{*}(\frac{t-u}{s})dt \tag{4.1}$$

where u and s are the translation and the scale parameters, respectively; the superscript * stands for a complex conjugate. The wavelet coefficient $wt(u,s)$ calculated from WT represents the degree of correlation between signals $v(t)$ and the wavelet at translation u and scale s [121]. The coefficients in the time-scale domain can be interpreted into ones in the time-frequency domain as the relationship between scale and frequency is inversely proportional. Various kinds of wavelets like Hermite, Morlet, and Daubechies have been used to extract specific features in the time-frequency domain according to the characteristics of the signals [120].

WT has been widely used for fault detection in various engineering applications either solely or combined with other techniques [81, 122-128]. Wang et al. [129] showed that WT could visually represent faulty symptoms of spur gears in the time-frequency domain. Wang et al. [121] proposed a unified framework that used FT with WT to effectively process periodic fault features from wavelet coefficients. Many studies combined WT with machine learning (ML) methods like support vector machine and neural networks [130-133]. However, the previous studies are limited to fault diagnosis under constant speeds because features extracted from FT and ML techniques may vary according to speed conditions [115].

4.1.2 Gaussian Process

A GP can be defined as a collection of random variables at time t, while any of the random variables are jointly Gaussian distributions [134]. The GP technique has been widely used to predict system behaviors from the non-linear data [135-141]. A GP is fully determined by its mean function $m(t) = \mathrm{E}[Y(t)]$ and covariance function $k(t, t') = \mathrm{E}[Y(t)Y(t')]$ for a stochastic process $Y(t)$, where $Y(t)$ can be represented as

$$Y(t) \sim GP(m(t), k(t, t')) \tag{4.2}$$

The mean function is assumed to be a zero-mean function in most studies [142]; a squared exponential covariance function is commonly used for the covariance function, as shown below

$$k(t, t') = \sigma_f^2 \exp(-\frac{\|t-t'\|^2}{2\sigma_t^2}) \tag{4.3}$$

where σ_f^2 and σ_t^2 are hyper-parameters, which can be learned by maximizing the likelihood function [134].

Suppose that there are N noisy observations $\mathcal{D} = \{(t_i,\ y_i) | i = 1, \dots, N\}$ from $y_i = f(t_i) + w_i$, where w_i is $\mathcal{N}(0, \sigma_w^2)$. Then, the covariance between y_i and y_j is computed as shown below

$$\operatorname{cov}(y_i, y_j) = k\left(t_i, t_j\right) + \sigma_w^2 \delta_{ij} \tag{4.4}$$

where δ_{ij} is the Kronecker delta function. Alternatively, it can be expressed in matrix form as

$$\operatorname{cov}(\boldsymbol{y}) = K(\boldsymbol{t}, \boldsymbol{t}) + \sigma_w^2 \boldsymbol{I} \tag{4.5}$$

where vectorized forms are used for the identity matrix, I, $\boldsymbol{t} = (t_1, \dots, t_N)^{\mathrm{T}}$, and $\boldsymbol{y} = (y_1, \dots, y_N)^{\mathrm{T}}$. Then, GP regression could predict the distribution for a new observation $(t_{\text{new}}, y_{\text{new}})$. The conditional distribution for the predictive output is defined as

$$y_{\text{new}} | \mathcal{D} \sim \mathcal{N}(m(t_{\text{new}} | \mathcal{D}), \sigma_{\text{new}}^2(t_{\text{new}} | \mathcal{D})) \tag{4.6}$$

where

$$m(t_{\text{new}} | \mathcal{D}) = \ k(t_{\text{new}}, \boldsymbol{t})^{\mathrm{T}} (K(\boldsymbol{t}, \boldsymbol{t}) + \sigma_w^2 I)^{-1} \boldsymbol{y} \tag{4.7}$$

And

$$\sigma_{\text{new}}^2(t_{\text{new}} | \mathcal{D})) = \sigma_f^2 - k(t_{\text{new}}, \boldsymbol{t})^{\mathrm{T}} (K(\boldsymbol{t}, \boldsymbol{t}) + \sigma_w^2 I)^{-1} k(t_{\text{new}}, \boldsymbol{t}) \tag{4.8}$$

In equations (4.7) and (4.8), $k(t_{\text{new}}, \mathbf{t})$ is a covariance vector that calculates the covariance that includes the new observation data.

As can be seen above, GP regression could predict statistical quantities (i.e., mean and standard deviation) in the continuous domain along the time. In addition, GP regression is a nonparametric method that uses only observations, not parameters. Therefore, it is suitable for predicting non-linear behaviors of time-varying data. In addition, it could consider the uncertainties in the observed data.

4.2. The Proposed PER Method

The proposed PER method, which uses only the vibration signals acquired from accelerometers, will be explained in detail in this section. As described in the introduction, the proposed PER method was developed with the aim to detect faults of planetary gears under variable speed conditions. The flowchart of the proposed PER algorithm is shown in Figure 4-1, and as can be seen, the proposed PER method is composed of six steps aimed for testing vibration signals. After the six steps, the ratios of fault features are calculated between training normal and testing data. Then, the ratios are compared with the threshold value, which can be defined by training normal and fault signals. The proposed PER method steps are described in detail as following.

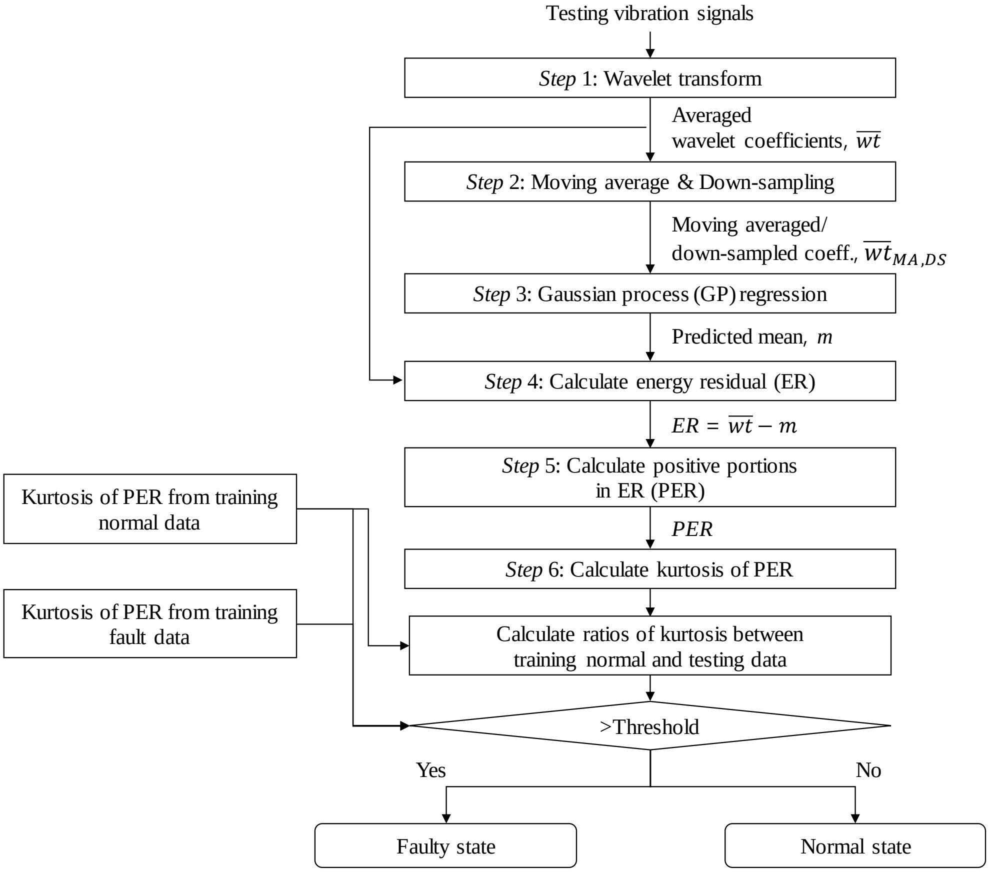

Figure 4-1 A flowchart of the proposed PER method

4.2.1. Wavelet Transform

As explained in Section 2, WT is used to decompose the raw vibration signals in the time domain to the time-frequency domain. For gear fault detection, wavelets like Morlet and Daubechies [129, 143] are widely used for extracting faulty features from the vibration signals. In this paper, Morlet wavelet is used as it is known to give superior results as compared to other wavelets used for gear fault detection [129].

Extracted Morlet wavelet coefficients from WT are represented in the time-scale domain, as

$$wt(u,s) = \frac{1}{\sqrt{s}} \int v(t)\psi^*_{Morlet}(\frac{t-u}{s})dt \tag{4.9}$$

where *v*(*t*) is the raw vibration signal and $\psi_{Morlet}(t)$ is the Morlet wavelet. Then, all the wavelet coefficients *wt*(*u*, *s_i*) from the scale-domain are averaged at each time-domain *u* as follows:

$$\overline{wt}(u) = \frac{1}{M_S}\sum_{i=1}^{M_S}|wt(u,s_i)| \tag{4.10}$$

where M_S is the whole number of scale parameters. The averaging is performed based on same weights at each coefficient. $\overline{wt}(u)$ can also be expressed as $\overline{wt}(t)$ because it is represented in the time-domain. From the averaged coefficients $\overline{wt}(t)$, we can observe how the energy of the signal fluctuates through time due to speed variation [144]. These coefficients could also express faulty behaviors, as the damaged gears induce abrupt increases of the energy in the vibration signals.

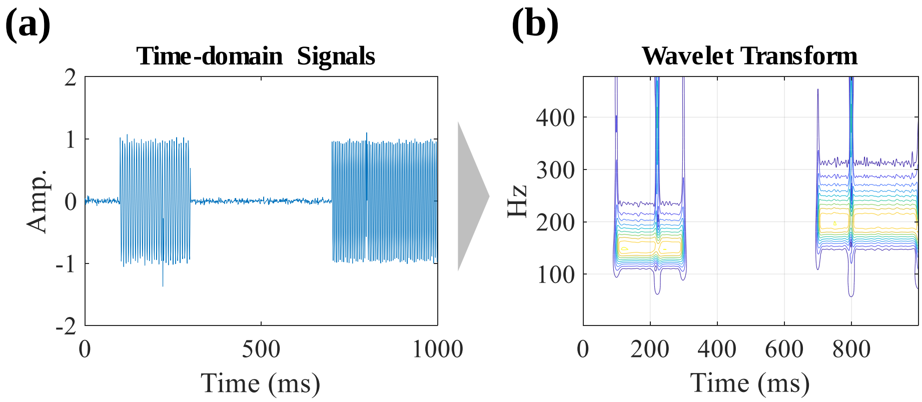

Figure 4-2 (a) Time-domain signals and (b) wavelet transform of the signals

Figure 4-2 shows how WT could express time and frequency information of the time-domain signals in the time-frequency domain. First of all, WT could express time-varying spectral information as can be seen in the figure. We could see that the two components have different frequency components. In addition, we could observe that WT could extract singular behaviors in the middle of the two components. Although the singularities are not clearly seen in the time-domain signals, we could obviously see the singularity behaviors in the high-frequency regions of the WT results.

Figure 4-3 shows how the shapes of the signals change along the proposed ideas. Figure 4-3(a) represents the averaged wavelet coefficients with faulty signals under variable speeds with a frequency of 1 Hz. In this state, the averaged coefficients $\overline{wt}(t)$ are not enough to be solely used for fault detection because the coefficients also fluctuate due to the variable speeds. Therefore, additional steps are needed. The averaging process could also be considered as marginalization without loss of generality [145].

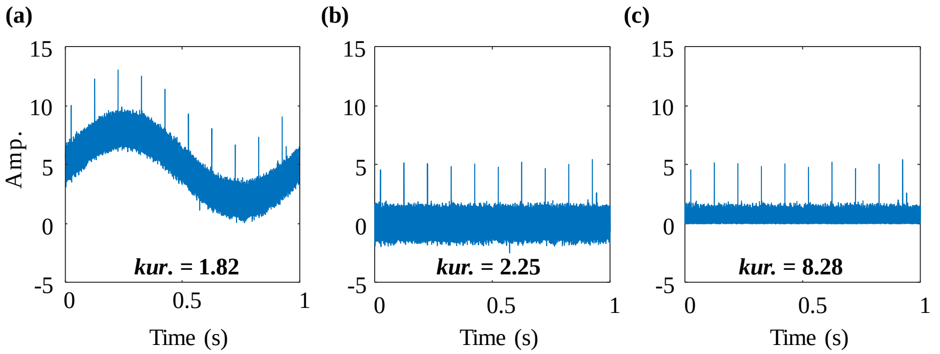

Figure 4-3 Changes of the shapes and kurtosis values at each step of the proposed method: (a) $\overline{\boldsymbol{wt}}$, (b) ER, and (c) PER

4.2.2. Moving Average and Down-sampling

The averaged wavelet coefficients $\overline{wt}(t)$ calculated from the previous step could have inherent uncertainty from noise, or other disturbances. Therefore, the $\overline{wt}(t)$ are moving-averaged to get smoothed, and time-varying behaviors of energy flow. The moving-averaged coefficients for pth time data t_p can be defined as

$$\overline{wt}_{\mathrm{MA}}(t_p) = \frac{1}{n}\sum_{i=1}^{n} \overline{wt}(t_{p-(i-1)}) \tag{4.11}$$

where *n* is the number of periods in the moving average. To reduce the computational cost in calculating the inverse of the covariance matrix in the next step, the moving-averaged coefficients $\overline{wt}_{\mathrm{MA}}(t)$ are down-sampled, and they become $\overline{wt}_{\mathrm{MA,DS}}(t)$, which results in down-sampled, moving-averaged wavelet coefficients. Down-sampled samples with down-sampling rate *d* have every *d*th sample from original ones, and have *d* times smaller samples than original samples *N*.

4.2.3. Gaussian Process (GP) Regression

The moving-averaged and down-sampled wavelet coefficients $\overline{wt}_{\mathrm{MA,DS}}$ are then processed with GP regression. In this paper, the zero-mean function and the squared exponential covariance function are used as explained in Section 4.1.2. Then, a GP model is fully defined by learning the hyper-parameters of the covariance function (i.e., σ_f^2 and σ_t^2). In this step, the accuracy of the regression model can be evaluated using mean square error or other metrics [140]. Next, the predictive mean value for down-sampled observation $\mathcal{D}_{\mathrm{DS}} = \left\{\left(t_i,\ \overline{wt}_{\mathrm{MA,DS}}(t_i)\right) \middle| i = 1, \dots, N_{\mathrm{DS}}\right\}$ is calculated using equation (4.7) with a developed GP regression model, as

$$m_{\mathrm{DS}}(t) = m(t|\mathcal{D}_{\mathrm{DS}}) = k(t, \boldsymbol{t}_{\mathbf{DS}})^{\mathrm{T}} (K(\boldsymbol{t}_{\mathbf{DS}}, \boldsymbol{t}_{\mathbf{DS}}) + \sigma_w^2 I)^{-1} \overline{\boldsymbol{wt}}_{\mathrm{MA,DS}} \quad (4.12)$$

where vectorized forms are used for down-sampled observations, $\boldsymbol{t}_{\mathbf{DS}} = (t_1, \dots, t_{N_{\mathrm{DS}}})^{\mathrm{T}}$ and $\overline{\boldsymbol{wt}}_{\mathrm{MA,DS}} = (\overline{wt}_{\mathrm{MA,DS}}(t_1) \ \dots, \overline{wt}_{\mathrm{MA,DS}}(t_{N_{DS}}))^{\mathrm{T}}$. From these mean values, we can estimate how the averaged wavelet coefficients behave under variable speeds. Then, the predicted mean values $m_{\mathrm{DS}}(t)$ are up-sampled to be in the same number of samples with wavelet coefficients. Then the up-sampled predicted mean value is defined as $m(t)$.

4.2.4. Energy Residual (ER) Computation

The ER is defined to remove the time-varying effects of wavelet coefficients from variable speeds. ER values $ER(t)$ can be calculated by subtracting the predicted mean values $m(t)$ from the averaged wavelet coefficients $\overline{wt}(\mathrm{t})$, and can be expressed as

$$ER(t) = \overline{wt}(t) - m(t) \quad (4.13)$$

The calculated $ER(t)$ could express residual energy in the vibration signals by subtracting the mean energy flow from the oscillating energy behaviors. The ER values have peaked behaviors due to the large wavelet coefficients produced from faulty vibration signals. Therefore, the ER values can express faulty behaviors when the time-varying behaviors of vibration signals are excluded. In addition, the calculation does not need any assumption of limited speed fluctuation. Figure 4-3(b) represents ER signals, which indicate energy behaviors when the variable speed condition is subtracted from the wavelet coefficients using GP regression. Therefore, the ER signals oscillate around a zero value. However, ER values are not sensitive enough to detect faults of small sizes. As can be seen in Figure 4-3(a) and (b), the kurtosis value is not significantly enhanced using the ER values. Therefore, we proposed the PER method, which can enhance the sensitivity of fault detection.

4.2.5. Positive Energy Residual (PER) Computation

In this step, the negative portions of ER are neglected, and only the positive portions are taken. The faulty behaviors in ER appear as increases of the wavelet coefficient *wt*(t), not as decreases. This is because the wavelet coefficients calculate the degree of correlation between vibration signals and the pre-defined wavelet. Therefore, only positive portions of the ER values are significant in quantifying the faulty behaviors. As a result, taking only the positive portions enhances the sensitivity of the proposed method to the presence (or not) of the faults. Figure 4-3(c) represents the PER signal, which takes only the positive portions in the ER signals in Figure 4-3(b).

4.2.6. Kurtosis from the PER Values

Next, a fault feature is calculated to quantify the faulty behaviors using PER. In this study, kurtosis is used to effectively highlight the abrupt increase of fault detecting capability [5] that arises from using the proposed PER method, which is defined as

$$kurtosis = \frac{E[(a_i-\mu)^4]}{\sigma^4} \tag{4.14}$$

where μ and σ are the mean and standard deviation of the data samples ai, and E[·] is the expectation. The kurtosis values calculated from the signals of averaged wavelet coefficients $\overline{wt}$, ER, and PER shown in Figures 4-3(a), (b), and (c) are 1.82, 2.25, and 8.28, respectively. The main reason for the differences in the kurtosis values is the variance value of each signal, which is the denominator in equation (14). The variance values of $\overline{wt}$, ER, and PER are 5.09, 0.59, and 0.15, respectively. For averaged wavelet coefficients, they fluctuate along the variability of the speeds, and the variance values are larger than the other cases. This results in the smallest kurtosis value and makes it difficult to detect faults using only the averaged wavelet coefficients $\overline{wt}$. In the case of ER, as variability of the signals is subtracted, kurtosis can better quantify the effect of fault signals. However, the kurtosis value does not increase significantly when the fault symptoms are not severe. Therefore, the effects of fault signals are enhanced in kurtosis values of PER by taking only the positive portions of ER. In this case, the kurtosis values increased more than three times in PER compared to those in ER. Figure 4-4 shows the overall procedure for the proposed PER method.

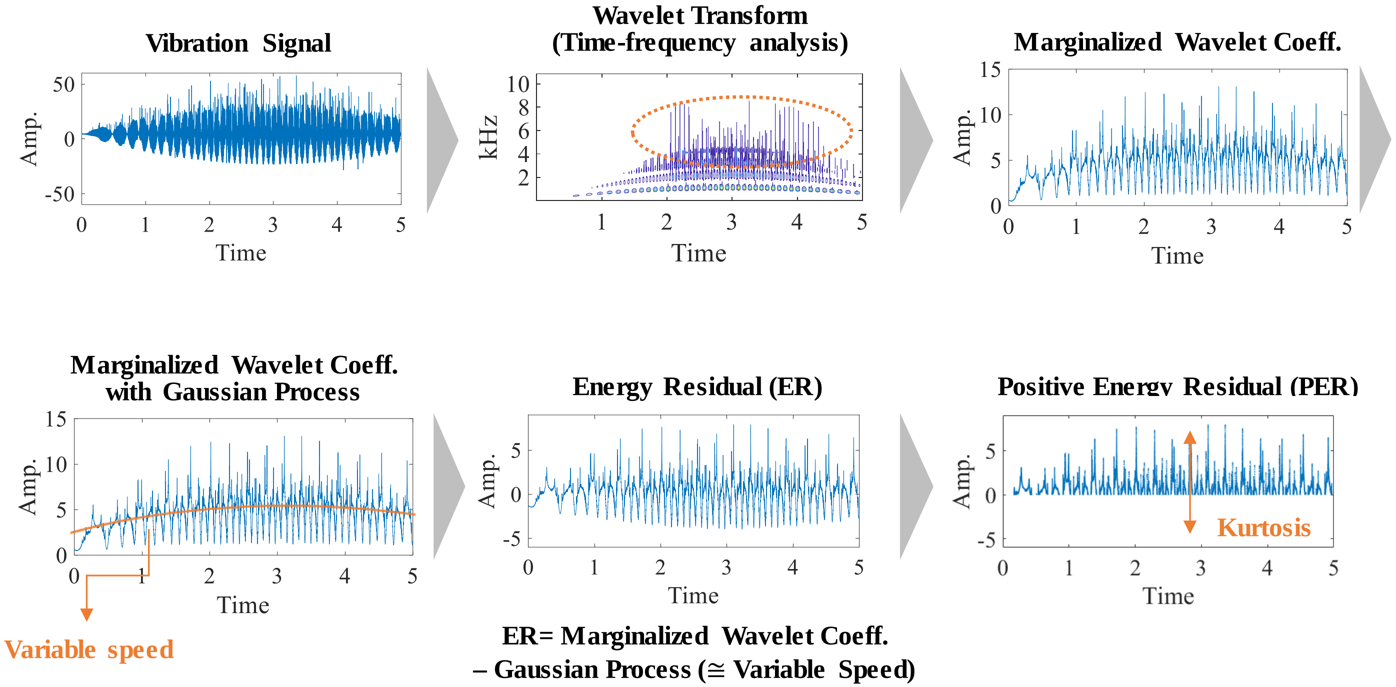

Figure 4-4 Overall procedure of the proposed PER method

4.3. Case Studies

This section will demonstrate the proposed PER method using the case studies. In Section 4.3.1, we will first use a simulation model of the planetary, which is explained in Section 3.1. Then, the demonstration would be performed using the experiment signals, which we explained in Section 3.2.

4.3.1. Case Study with the Simulation Model

In this section, we demonstrate the effectiveness of the proposed PER method using the simulation models developed in Section 3.1. Figure 4-4 shows the results from each step of the proposed method in a normal condition and through the four levels of faults. Figure 4-4(a) shows the averaged wavelet coefficients $\overline{wt}$ calculated from the Morlet wavelet. The coefficients were averaged from all the scales, as described in Section 4. As can be seen, the averaged wavelet coefficients fluctuate along the time due to variable speed conditions. In addition, the modulations of vibration signals arising from contacts of planet gears make oscillations of these coefficients. For the fault cases, the peaked vibration signals appeared all around the signals, and they get larger for the larger sizes of faults. Figure 4-4(b) shows GP regression results. The blue solid lines are averaged wavelet coefficients $\overline{wt}$ calculated from previous steps and the green dotted lines are the predicted mean values m calculated from the GP regression. Next, ER values were calculated by subtracting predicted mean values $m(t)$ from the averaged wavelet coefficients $\overline{wt}(t),$ as defined in Eq. (4.5), and shown in Figure 4-4(c). Therefore, the ER values oscillated around zero values. Finally, only positive values of the ER values were taken to determine PER, as shown in Figure 4-4(d). By following these procedures, the effects from variable-speed condtions could be minimized while enhancing fault sensitivity.

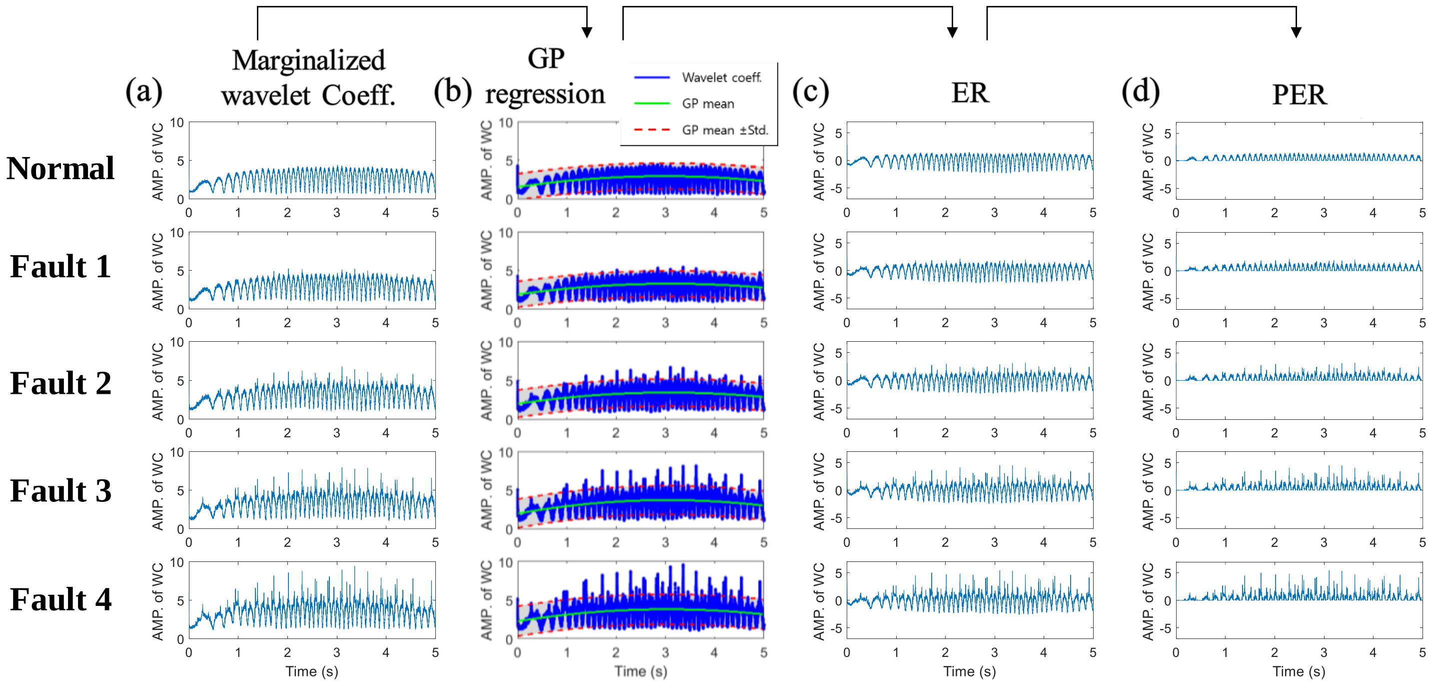

Figure 4-5 The results of the proposed PER method using the simulated vibration signals in normal and four levels of faulty states: (a) averaged wavelet coefficients, (b) GP regression, (c) ER, and (d) PER

Figure 4-6 and Table 4-1 show the ratios of kurtosis between normal and each fault level (F1 = level 1, F2 = level 2, F3 = level 3, and F4 = level 4) using WT, ER, and our newly proposed PER. In this procedure, kurtosis values were calculated using all samples from zero to five seconds. For all fault levels, the proposed PER method performed better than both the WT method and the ER method. In particular, the proposed PER method could differentiate the smallest fault level (i.e., level 1) while other methods could not. It should be noted that the ER method showed slightly better performance than WT.

In Figure 4-7, we compared the performance of the proposed PER method with the order-tracking method using the resampling technique. In the result, we could see that the proposed PER method shows similar performance with the order-tracking method. And, as noticed in the chapter 2, the proposed PER method does not need angular measurement while the order-tracking method need angular measurement.

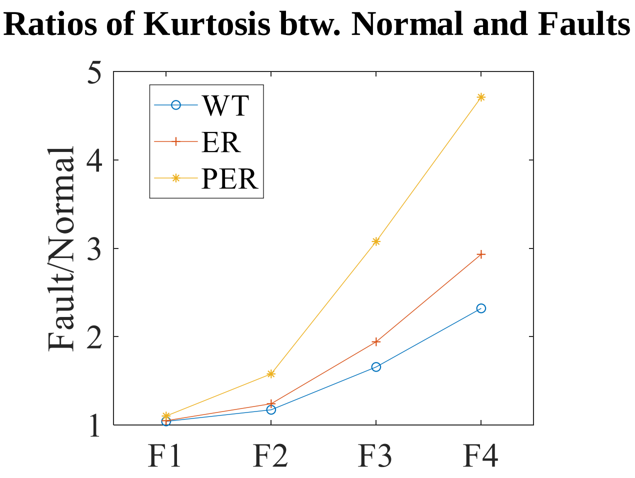

Figure 4-6 Ratios of kurtosis between normal and each fault level using WT, ER, and PER methods with simulation signal

Table 4-1 Summary results of the ratios of kurtosis from normal and each fault level using WT, ER, and PER methods with simulation signals

	F1	**F2**	**F3**	**F4**
WT	1.03	1.20	1.56	2.18
ER	1.05	1.27	1.82	2.73
PER	1.07	1.70	2.86	4.35

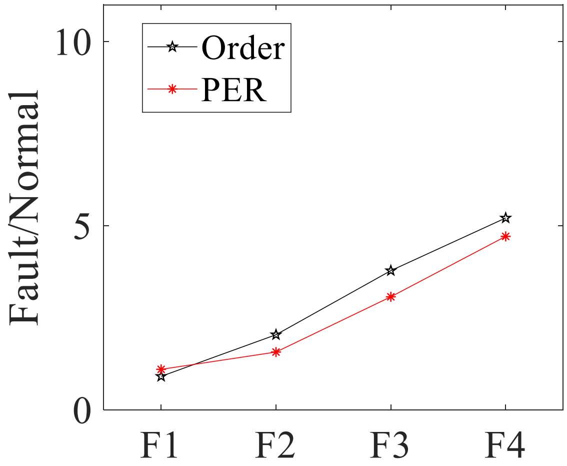

Figure 4-7 Fault sensitivity results of the order-tracking method and the proposed PER method for simulated vibration signals

Figure 4-8 shows ratios of kurtosis between normal and each fault level using the proposed PER methods under different noise levels. We could see that the proposed PER method shows less sensitive results as the noise level gets higher.

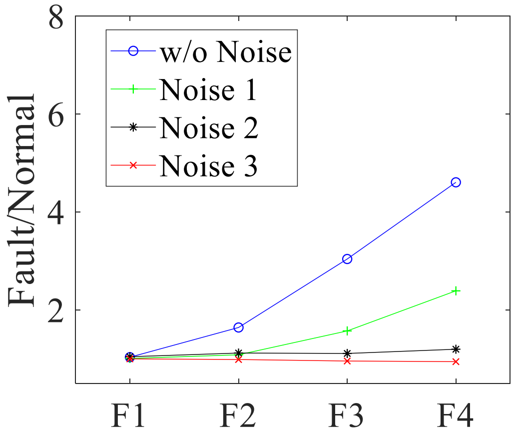

Figure 4-8 Ratios of kurtosis between normal and each fault level using the proposed PER methods with simulation signals under different noise levels

Next, we also observed the online monitoring capability of the PER method by injecting the fault in the middle of the signals. Figure 4-9 shows the simulated vibration signals from the normal condition and the four levels of faults. The peaks arising from the faults get larger as the fault gets more severe from levels 1 to 4. The magnitudes of each fault are about 25, 50, 75, and 100% of the maximum amplitudes of the normal vibration signals.

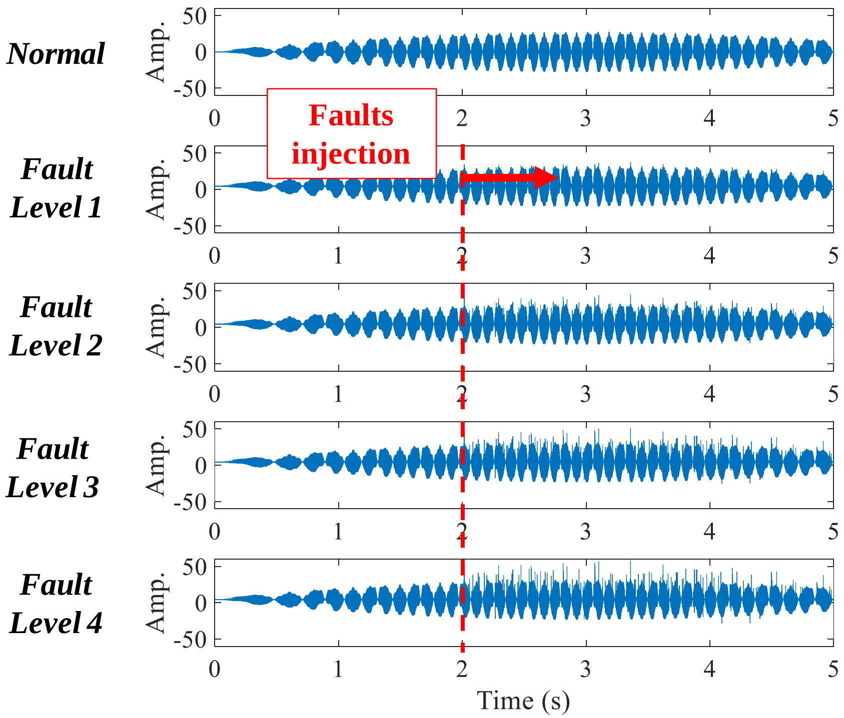

Figure 4-9 Simulated vibration signals in a normal condition and with four levels of faults that start from 2 seconds

Figure 4-10 shows the results from each step of the proposed method in a normal condition and through the four levels of faults. Figure 4-10(a) shows the averaged wavelet coefficients $\overline{wt}$ calculated from the Morlet wavelet. The coefficients were averaged from all the scales, as described in Section 3. As can be seen, the averaged wavelet coefficients fluctuate along the time due to variable speed conditions. In addition, the modulations of vibration signals arising from contacts of planet gears make oscillations of these coefficients. For the fault cases, the peaks appeared after two seconds, and they get larger for the larger sizes. Figure 4-10(b) shows GP regression results. The blue solid lines are averaged wavelet coefficients $\overline{wt}$ calculated from previous steps and the green dotted lines are the predicted mean values m calculated from the GP regression. Next, ER values were calculated by subtracting predicted mean values m from the averaged wavelet coefficients $\overline{wt}(t)$, as defined in Eq. (4.5), and shown in Figure 4-10 (c). Therefore, the ER values oscillated around zero. Finally, only positive values were taken to determine PER, as shown in Figure 6(d).

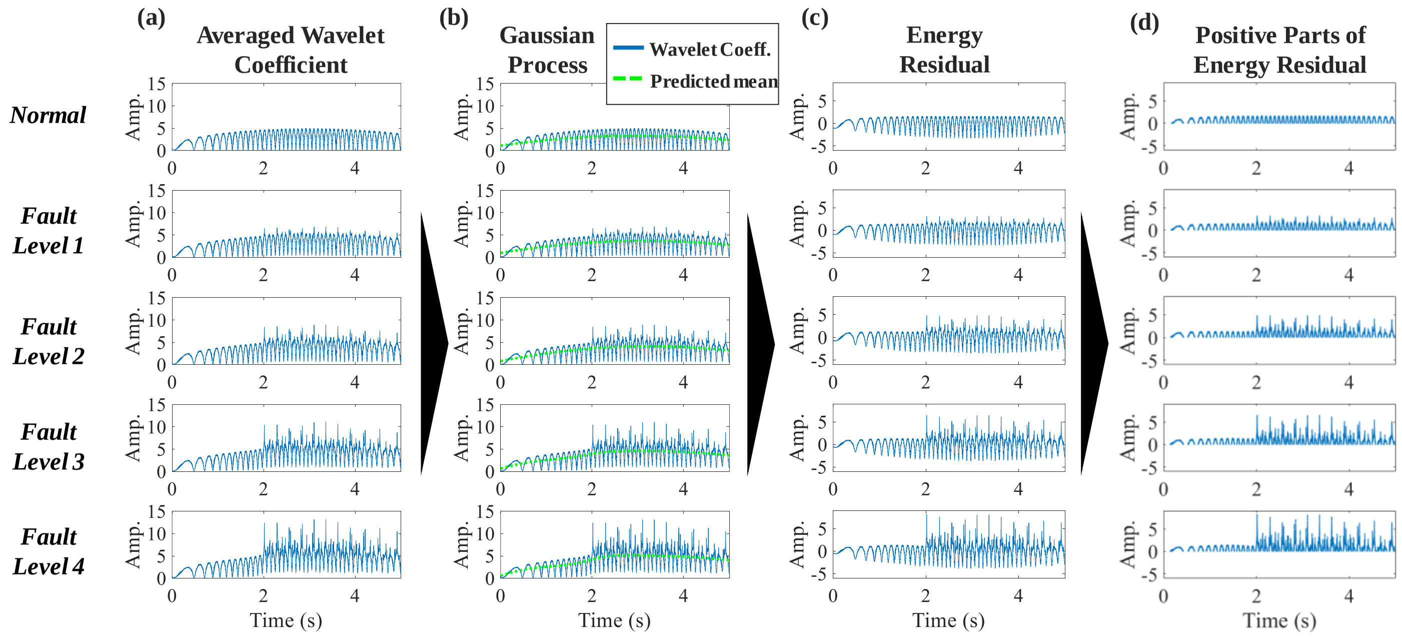

Figure 4-10 The results of the proposed PER method using the simulated vibration signals with faults that starts from 2 seconds in normal and four levels of faulty states: (a) averaged wavelet coefficients, (b) GP regression, (c) ER, and (d)

Next, we calculated the differences of kurtosis between normal and faulty states from PER values, to quantify the degradation level. In the calculation, we used differences of kurtosis instead of ratios to observe the change of the kurtosis at the fault injection time. The kurtosis values were calculated at each time sequence for a normal condition and for each fault level. Figure 4-11 shows the cumulative sums of the kurtosis differences between normal and each faulty state. We also calculated the kurtosis values using WT and ER methods to compare the performance of the proposed PER method. For all of the fault cases, the cumulative sums of kurtosis were nearly zero from all the methods until the time of two seconds, when the faults were injected. Then, the cumulative sums of kurtosis differences started to increase for all cases. As can be seen in Figure 4-11, the fault detection performance was slightly better when using ER than when using WT, however, the sensitivity of the proposed PER method for fault detection was better than either of the previous two methods, WT and ER.

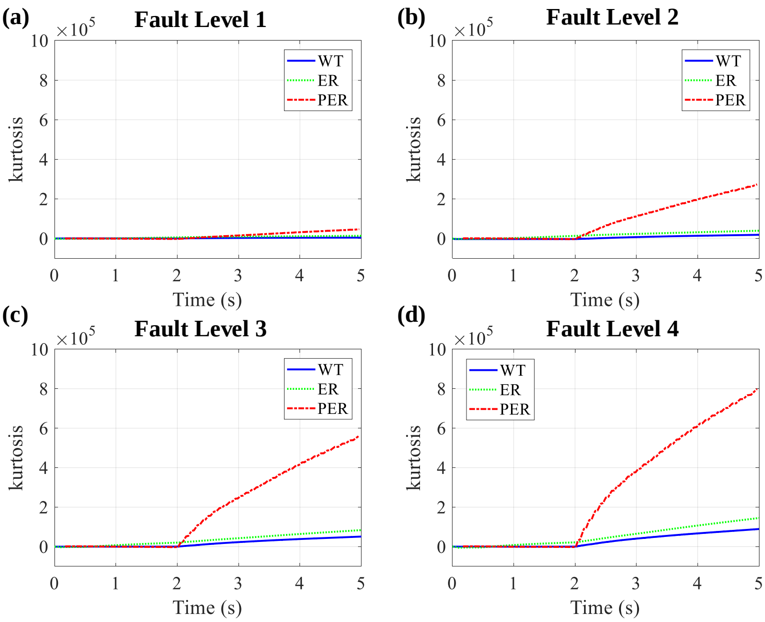

Figure 4-11 Cumulative sums of kurtosis differences using simulation signals with WT, ER, and PER for (a) fault level 1, (b) fault level 2, (c) fault level 3, and (d) fault level 4

4.3.2. Case Study with the Experiment Data

The proposed PER method was also applied to experimentally measured acceleration signals from a planetary gearbox in a variable speed condition explained in Section 3.2. Figure 4-12 shows the results from each step of the proposed PER method when using the signals in a sinusoidal speed profile. WT could extract faulty characteristics, but the behaviors were not significant due to the variable speed conditions, as shown in Figure 4-12(a). GP regression could predict behaviors of variable speeds, as shown in Figure 4-12(b). In Figure 4-12(c), ER values were calculated by subtracting the predicted mean values from the averaged wavelet coefficients. Then, only positive portions were used to enhance sensitivity of the PER, as shown in Figure 4-12(d).

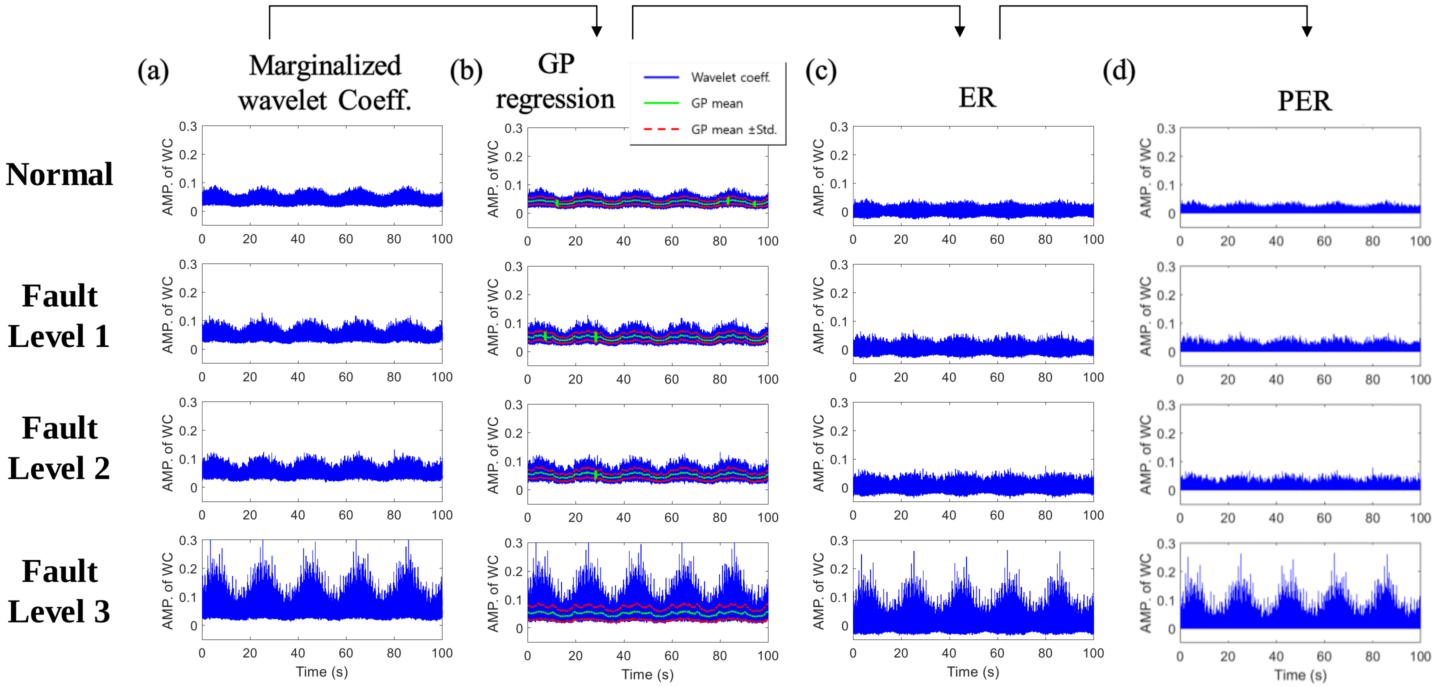

Figure 4-12 The results of the proposed PER method using the sinusoidal speed signals from the experiment in a normal and three levels of faulty states: (a) averaged wavelet coefficients, (b) GP regression, (c) ER, and (d) PER

Figure 4-13 and Table 4-2 show the ratios of kurtosis between the normal condition and each fault level (F1 = level 1, F2 = level 2, and F3 = level 3) using WT, ER, and the newly proposed PER from the sinusoidal and the linearly decreasing speed profiles. For all fault levels, the PER method outperformed the other methods, WT and ER. For fault level 1, the performances of the ER and PER were similar. However, as fault levels go higher to levels two and three, the performace of the proposed PER method gets better than the other two methods, wavelet coeffcients and energt residual. Therefore, we could conclude that the proposed PER method enhance the fault sensitivity for the planetary gears under variable-speed conditions from the previous methods that only use wavelet coefficients. Further, the fault feature behaviors using kurtosis show linear behaviors along the fault level.

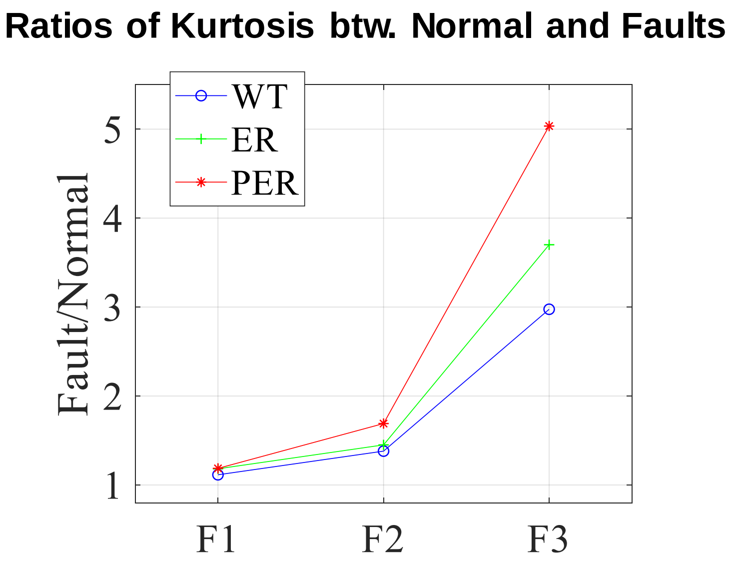

Figure 4-13 Ratios of kurtosis between normal and each fault level using WT, ER, and PER methods with simulation signal

Table 4-2 Summary results of the ratios of kurtosis between normal and each fault level using WT, ER, and PER methods for signals from the experimental setup

	F1	**F2**	**F3**
WT	1.11	1.38	2.98
ER	1.18	1.45	3.70
PER	1.19	1.69	5.04

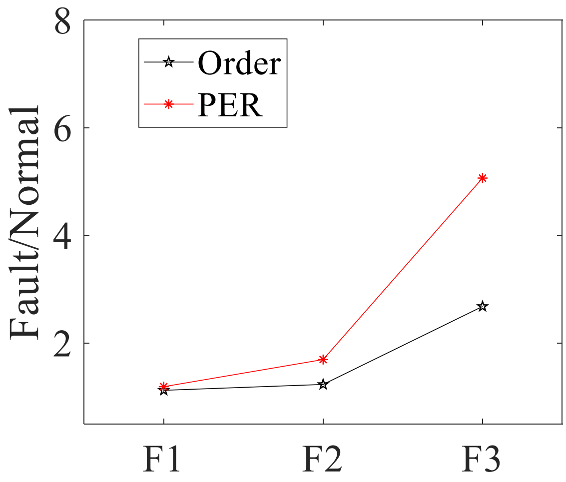

Figure 4-14 Fault sensitivity results of the order-tracking method and the proposed PER method for experiment vibration signals

In Figure 4-14, we show the performance of the proposed PER method for the experiment signals with the order-tracking method. We could find that the proposed method shows better performance than the order-tracking method.

Figure 4-15 shows ratios of kurtosis between normal and each fault level using the proposed PER methods with the experiment signals under different noise levels. We could see that the proposed PER method shows less sensitive results as the noise level gets higher.

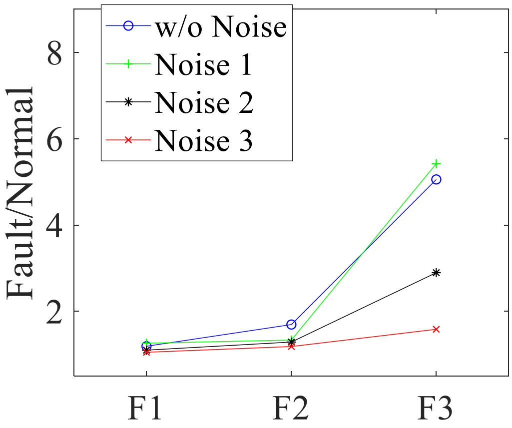

Figure 4-15 Ratios of kurtosis between normal and each fault level using the proposed PER methods with experiment signals under different noise levels

4.4. Summary and Discussion

In this paper, a new, positive energy residual (PER) method was proposed to detect faults in a planetary gear under variable speed conditions. In the proposed method, WT was performed to extract both varying speeds and faulty characteristics from the vibration signals. Then, GP regression was used to predict averaged variable speeds, which were then subtracted from wavelet coefficients to obtain energy residual (ER). Then, only the positive values of ER (PER) were taken to enhance the sensitivity of the proposed method. Finally, kurtosis values were calculated to effectively quantify the peaked signals in PER. From the two case studies, which used simulated and experimental acceleration signals from a planetary gear, it was demonstrated that the proposed PER method could detect faults of a planetary gear under variable speeds while showing better performance than both the WT and the ER methods in terms of sensitivity to the presence of faults. The benefits of the proposed PER method are that it can be applied to large fluctuations of speeds, and it does not need angular information of the gears, unlike other methods based on the order tracking algorithm. Future work can be conducted to validate the proposed PER method to detect other types of planetary gear faults, such as tooth root crack, tooth breakage, or pitting. Further, PER will be investigated and applied to other rotating machinery like bearings, rotors, and electrical motors. However, one drawback of the proposed method is that the method could require huge computation time for analyzing wider frequency regions. Therefore, time-efficient fault diagnosis methods are required.

Sections of this chapter have been published as the following journal articles:

1) **J. Park**, M. Hamadache, J. M. Ha, Y. Kim, K. Na, and B. D. Youn, "A positive energy residual (PER) based planetary gear fault detection method under variable speed conditions," *Mechanical Systems and Signal Processing*, vol. 117, pp. 347-360, 2019.

Chapter 5

Variance of Energy Residual (VER) Method for Computational Efficiency

The proposed VER method is described in detail in this section. The VER method offers the potential to reduce computation time by using STFT, rather than the WT approach used in the PER method. We first review basic principles of the STFT technique, and explain how the technique is different from WT. We also show a simple example to compare the characteristics of the STFT and WT techniques. Then, detailed procedures for the proposed VER method are outlined. Finally, we will present two case studies, a simulation model and experiment data, to demonstrate the performance of the proposed VER method.

5.1. Review of Short-time Fourier Transform

Similar to WT, STFT is also a TFA technique that observes vibration signals in the time-frequency domain. The computation time of STFT can be less than that needed for WT due to the averaging effect from the chosen window function [146]. The basic formulation for STFT is as follows:

$$\mathrm{STFT}(\tau, f) = \int v(t) g(t-\tau) e^{-i2\pi f t} dt \tag{5.1}$$

where $g(t-\tau)$ is a window function centered at $t = \tau$, and f is frequency. Therefore, STFT can be considered to be a windowed Fourier transform (FT) over time. Although STFT requires less computation time due to the averaging from the window function, the peak detectability is less than that of WT. Figure 5-1 shows an example that compares the computation time and peak detectability of STFT and WT.

Figure 5-1(a) shows the sinusoidal signals of 1,500 Hz and 2-second samples at 10,000 Hz, where the signal-to-noise (SNR) ratio is about 17 dB. In the vibration signals, a singularity is added at 0.5 seconds to compare the peak detection performance of STFT and WT. Figure 5-1(b) and Figure 5-1(c) show STFT and WT results from the vibration signals. As can be seen, the main component can be observed near 1,500 Hz in both STFT and WT results. However, the singularity component at 0.5 seconds is less clearly represented in the STFT results than in the WT results. In other words, the singularity is illustrated with more blurred images in STFT than in WT. From the results we can see that WT has better fault diagnostic

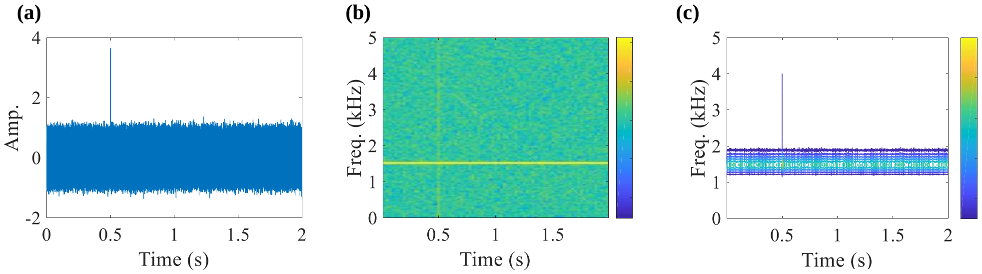

Figure 5-1 Comparison of computation time and peak detectability between STFT and WT: (a) vibration signals with peak at 0.5 seconds, (b) STFT of the vibration signals, and (c) WT of the vibration signals

capability than STFT in this case. However, STFT requires less computation time. In this case, it takes 0.13 seconds for the STFT analysis, while it takes 3.56 seconds for the WT analysis. Therefore, from this example, we can conclude that STFT has less fault sensitivity than WT, while it shows better computational efficiency. One more thing of particular note is the fault symptom in both STFT and WT. In Figure 5-1(b), the fault symptom of STFT appears as spread in all the frequency regions. However, in Figure 5-1(c), the fault symptom of WT appears as abrupt increases of the wavelet coefficients.

5.2. The Proposed VER Method

The overall procedures used for the VER method for fault detection of planetary gears under variable-speed conditions are shown in Figure 5-2. The flowchart in Figure 5-2 is composed of four steps. The procedures are developed to determine whether the testing signals are in a faulty state (or not) by comparing the VER values with training normal and faulty VER values. As shown in Figure 5-2, the proposed VER method only uses the vibration signals measured from accelerometers; it does not need the angular information that is needed by order-tracking based methods. In addition, the VER method could reduce computation time by adopting STFT for TFA, instead of WT. A detailed description of each step is provided below.

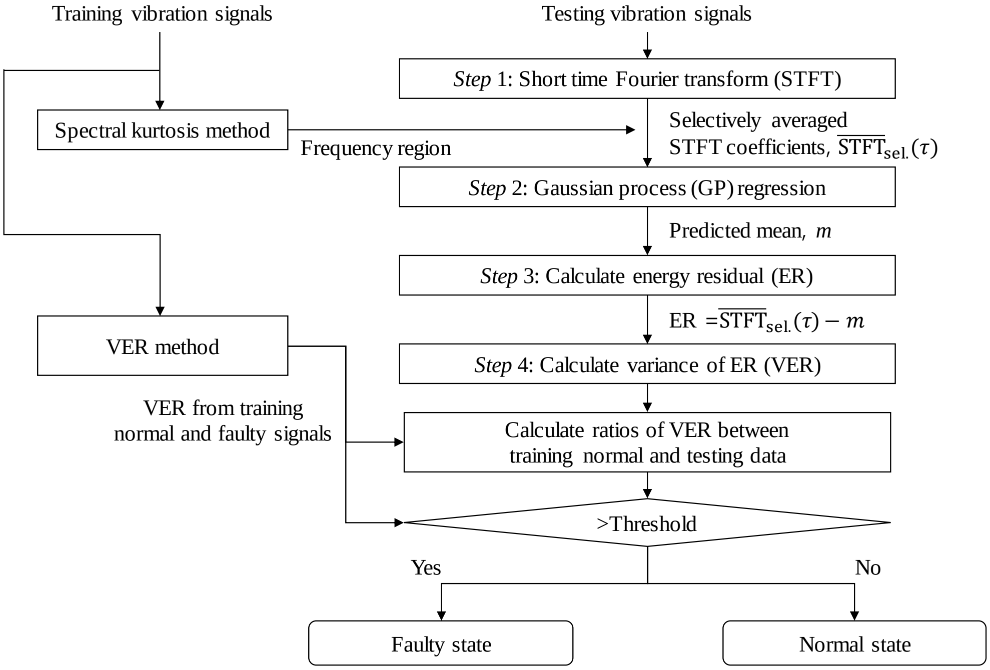

Figure 5-2 A flowchart of the VER method for fault detection of planetary gears under variable-speed conditions

5.2.1. Short-time Fourier Transform

A STFT technique is used to represent the faulty symptoms, as well as the time-varying behaviors of vibrations signals. As noted in Section 5.1, the STFT technique could reduce the computation time of the VER method compared to the WT technique used in the PER method. In this step, the window type and length of the window function need to be selected according to the characteristics of the given signals and systems. Using the window function, as noted in Section 3.1, fault sensitivity reductions could come at the expense of computational efficiency. Therefore, in this research, additional processing is performed to enhance the fault detection performance of STFT. In previous research, the TFA coefficients were averaged from all over the frequency range along time. However, in the proposed VER method, STFT coefficients are averaged only in the selected frequency regions to enhance fault sensitivity, as shown in the equation below,

$$\overline{\mathrm{STFT}}_{\mathrm{sel.}}(t) = \frac{1}{N_e - N_s + 1} \sum_{i=N_s}^{N_e} |\mathrm{STFT}(t, f_i)| \tag{5.2}$$

where N_S and N_e, respectively, are the starting and ending numbers of the sequence for selected frequency range. The frequency ranges that contain the most faulty behaviors are usually near the resonance frequency of the given system, as the resonance frequency is known to be excited under faults in rotating machinery [147]. In the VER method, the frequency ranges are automatically determined using spectral kurtosis. The spectral kurtosis is a method to find the frequency regions with the most non-Gaussian faulty behaviors [23]. Therefore, fault sensitivity could be improved by calculating selectively averaged STFT coefficients $\overline{\mathrm{STFT}}_{\mathrm{sel.}}(t)$, which were determined based on the spectral kurtosis technique. In this study, the kurtogram is used to find the optimal central frequency and bandwidth of the frequency regions [148].

5.2.2. Gaussian Process (GP) Regression

The selectively averaged STFT coefficients calculated in the previous step are used to perform GP regression in this step. A GP could be defined as a stochastic process where each of the components is joint Gaussian distribution. The GP can be formulated as

$$Y(t) \sim \mathrm{GP}(m(t), k(t, t')) \tag{5.3}$$

where $m(t)$ is the mean function $\mathrm{E}[Y(t)]$ and $k(t, t')$ is covariance function $\mathrm{E}[Y(t)Y(t')]$ for stochastic process $Y(t)$ [134]. The objective of the GP regression in the VER method is to estimate the effects of the variable speed in the calculated STFT coefficients; this can be achieved by calculating the mean function $m(t)$ in the predicted GP regression model.

5.2.3. Energy Residual (ER) Computation

In this step, ER is defined to remove the effects of the variable-speed conditions in the calculated STFT coefficients. The ER is calculated by subtracting the estimated mean function $m(t)$ from the selectively averaged STFT coefficients $\overline{\mathrm{STFT}}_{\mathrm{sel.}}(t)$ as

$$\mathrm{ER}(t) = \overline{\mathrm{STFT}}_{\mathrm{sel.}}(t) - m(t) \tag{5.4}$$

As noted in Step 1, the STFT coefficients could represent the time-varying behaviors and faulty information of the vibration signals. In addition, the faulty information could be enhanced by selectively averaging the coefficients. Therefore, subtraction of the estimated mean function could minimize the effects of the time-varying behaviors of the STFT coefficients, and thus highlight the effects of faults in the system.

5.2.4. Variance from the ER Values

The calculated ER values need to be quantified as a fault feature to show the degree of fault severity. Fault features that are commonly used for gear diagnostics include RMS, kurtosis, and Crest Factor, among others [101]. In this step, we use variance for the fault feature of ER, in contrast to kurtosis, which was used for the fault feature in the previous PER method. In the wavelet coefficients, as can be seen in Figure 4-2(b) in Section 4, the fault symptom is characterized as the increase of the coefficients. Therefore, kurtosis is able to effectively quantify the degree of the faults in the signals, because kurtosis measures the thickness of the tail in the distribution, or outliers in the data [149]. In the VER method, however, variance of the data is used for the fault feature as

$$\text{variance} = \frac{1}{M-1}\sum_{i=1}^{M}|a_i - \mu|^2 \tag{5.5}$$

where μ and M are the mean and total number of data samples ai. In STFT, the fault symptom of the calculated coefficient is represented as spread in all the frequency regions, as noted in Section 3.1. Therefore, variance is used to quantify the degree of faults in the ER values.

Table 5-1 shows the comparison between the proposed VER method and the previous PER method. First, the PER method uses WT as TFA to enhance fault sensitivity. The VER method uses STFT to reduce computation time by selecting appropriate window sizes. However, the fault sensitivity of the STFT could be smaller than WT. Therefore, the VER method selectively averages the TFA coefficients in the sensitive frequency range, which can be determined automatically using spectral kurtosis. The details of the spectral kurtosis methods could be found in literature [23, 150-153]. In the PER method, the whole frequency ranges are used to obtain the TFA coefficients. Finally, the previous PER method used kurtosis as a fault feature because fault symptom appears as increases of the wavelet coefficients. In the VER method, however, we uses the variance as the fault feature because fault symptom appears as spread in the whole frequency region. Therefore, in the VER method, we could reduce the computation time for the fault detection method while maintaining faulty sensitivity.

Table 5-1. Comparison between the VER and PER methods

	PER (Positive energy residual)	**VER (Variance of Energy residual)**
Time-frequency analysis (TFA)	Wavelet transform	Short-time Fourier transform
Frequency range	Whole frequency region	Selected automatically by spectral kurtosis
Fault feature	Kurtosis	Variance

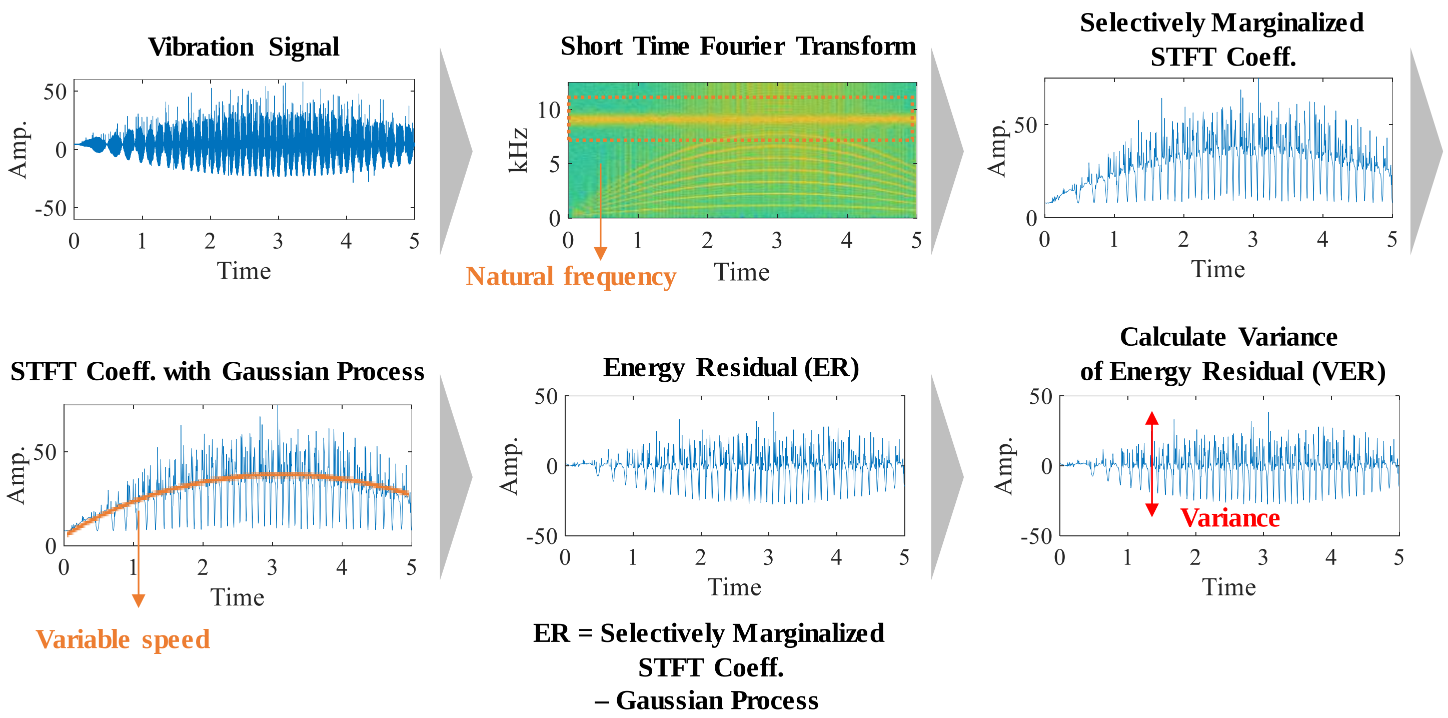

Figure 5-3 Overall procedure of the proposed VER method

5.3. Case Studies

5.3.1. Case Study with the Simulation Model

Figure 5-4 shows all of the procedures of the VER method when the method is applied to the simulated vibration signals shown in Figure 3-4. First, the time-varying behaviors of the vibration signals are represented using the STFT technique shown in Figure 5-4(a). The STFT is also able to reveal faulty information from the spread of STFT coefficients over the frequency axis at each time. A hamming window of 0.1 seconds in length was used with 0.05 seconds of overlap in this case. Next, the STFT coefficients are averaged over the selected frequency range over time, as shown in Figure 5-4(b). The selected frequency range for fault sensitivity enhancement is 4kHz around the resonance frequency, 10 kHz, which was calculated from the spectral kurtosis method. As can be seen in Figure 5-4(b), small fluctuations of the averaged coefficients get larger as the fault level gets larger. In addition, the large fluctuations represent the effects of the variable-speed condition on the STFT coefficient, which will be achieved by the predicted mean values of GP in Figure 5-4(c). By subtracting the predicted mean values from the averaged STFT coefficients, ER values are achieved, as shown in Figure 5-4(d). Finally, variances of ER (VER) values are calculated for each state to quantify the degree of faults.

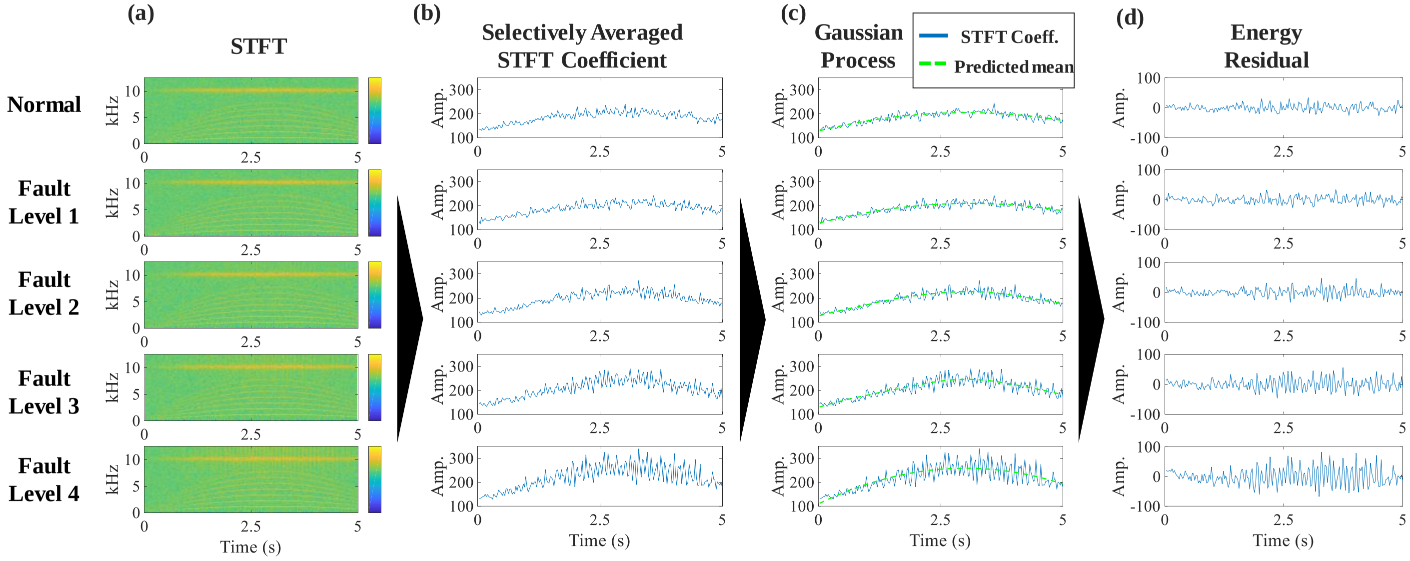

Figure 5-4 Procedures for the VER method for the simulated signals of a normal state and for four levels of faulty states: (a) STFT, (b) averaged wavelet coefficients, (c) GP regression, and (d) ER

Figure 5-5 shows the results of the VER methods (i.e., Figure 5-4(d)) compared with the PER method and variance values calculated from the selectively averaged STFT coefficients (i.e., Figure 6(b)) in terms of fault sensitivity and calculation time. Figure 7(a) shows the fault sensitivity results; these were achieved using the ratios of features from each fault state and the normal state. Figure 7(b) shows the calculation time result; it was based on 5 seconds of vibration signals. The sensitivity values are 1.07, 1.70, 2.86, and 4.35 for the PER method; 1.18, 1.61, 2.95, and 4.98 for the variance of the STFT coefficients; and 1.21, 1.46, 3.07, and 7.95 for the VER method used to examine fault levels one to four. As can be seen, the VER method showed the best fault sensitivity among the three methods for all fault levels. The calculation time of the PER method is about 140 and 11 times more than the variance of the STFT coefficients and the VER method. Although the variance of the STFT coefficients shows a smaller calculation time than the proposed VER method, the fault sensitivity is smaller than the PER method. In addition, the result from the variance of the STFT coefficients could be distorted because the effect of variable-speed conditions was not removed in the method.

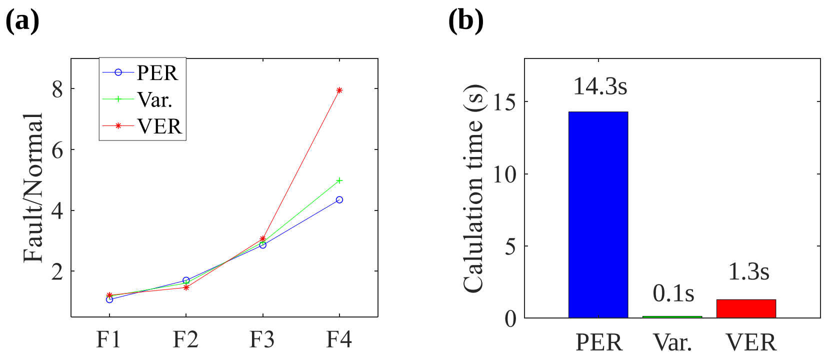

Figure 5-5 Performance of PER, Variance, and VER for simulated vibration signals: (a) fault sensitivity and (b) calculation time

We also compared the performance of the VER method with the order-tracking method. Figure 5-6 shows how the faulty raw signals could be transformed into resampled signals using the order-tracking method. As can be seen, the time- and frequency-domain signals were resampled in the sun gear rotation- and order-domain from Figures 5-6(a) and (b) to Figures 5-6(c) and (d). We could find that the speed variabilities of the signals in Figures 5-6(a) and (b) were removed in the resampled signals in Figures 5-6(c) and (d). Figure 5-7 shows the faulty sensitivity results of the order-tracking method and the proposed VER method. The sensitivity of the order-tracking method was calculated using the variance values of the averaged STFT coefficients from the resampled signals. The sensitivity values of the order-tracking method were 1.00, 0.96, 1.09, and 1.46 for the four levels of fault. From the results, we could find that the VER method have better performance in highlighting the faulty characteristics of the signals than the order-tracking method.

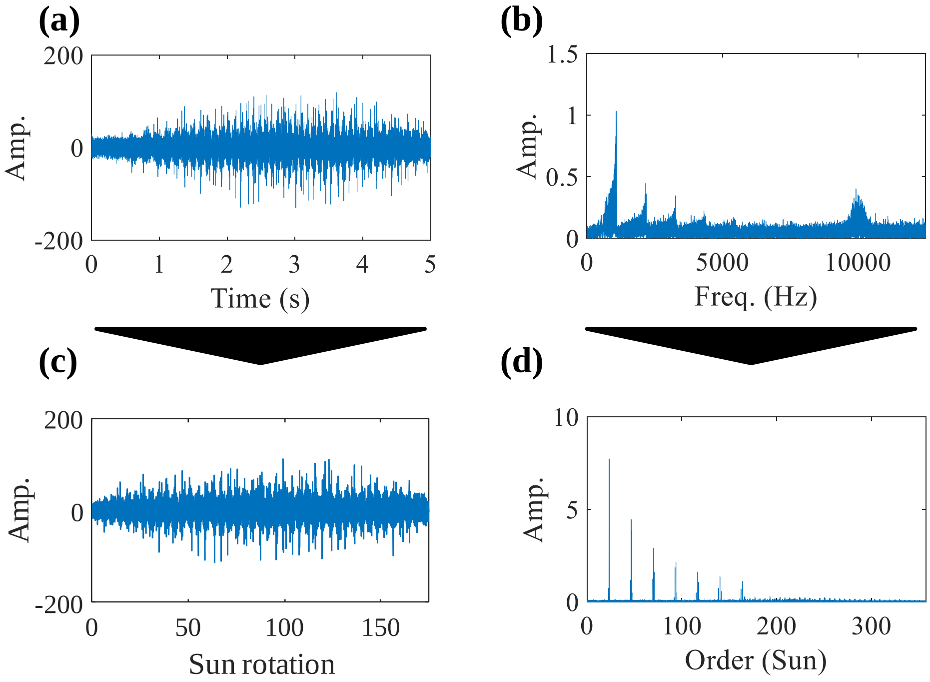

Figure 5-6 Transformation of the faulty simulated raw vibration signals into the resampled signals using the order-tracking method: (a) raw signals in time-domain, (b) raw signals in frequency-domain, (c) resampled signals in sun gear rotation-domain, and (d) resampled signals in order-domain

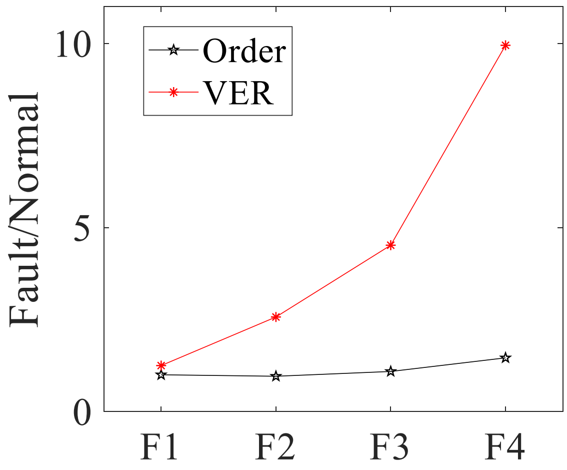

Figure 5-7 Fault sensitivity results of the order-tracking method and the proposed VER method for simulated vibration signals

Figure 5-8 shows ratios of VER values between normal and each fault level under different noise levels. We could see that the proposed VER method shows similar results under noise levels 1 and 2, and sensitivity gets lower under noise level 3. .

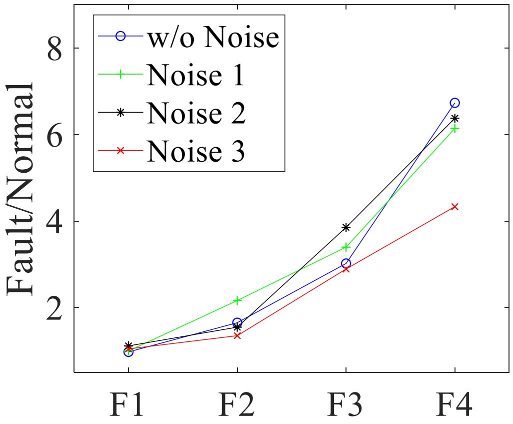

Figure 5-8 Ratios of VER values between normal and each fault level with simulation signals under different noise levels

5.3.2. Case Study with the Experiment Data

Figure 5-9 shows how the proposed VER method was applied to the experimental vibration signals. In Figure 5-9(a), the vibration signals from the STFT results show time-varying behaviors due to the variable-speed condition. A hamming window with a 0.05-second length and a 0.025-second of overlap was used in this case. In the STFT results, the system responded sensitively near 7 kHz. Therefore, in this part of the experiment, we chose 2 kHz near the 7 kHz to cover the frequency ranges that showed sensitive behaviors for selective averaging based on the spectral kurtosis method. In Figure 5-9(b), the selectively averaged STFT coefficients fluctuated along the variable-speed condition, while peaked behaviors became more severe as the fault level increased. The modulated behaviors of the STFT coefficients are predicted by the mean values of the GP regression, as shown in Figure 5-9(c). Next, the ER values were calculated by subtracting the predicted mean values from the

STFT coefficients, as shown in Figure 5-9(d). The variance values were calculated for each ER value (i.e., VER) to quantify the degree of faults in the signals of the planetary gear under variable-speed conditions.

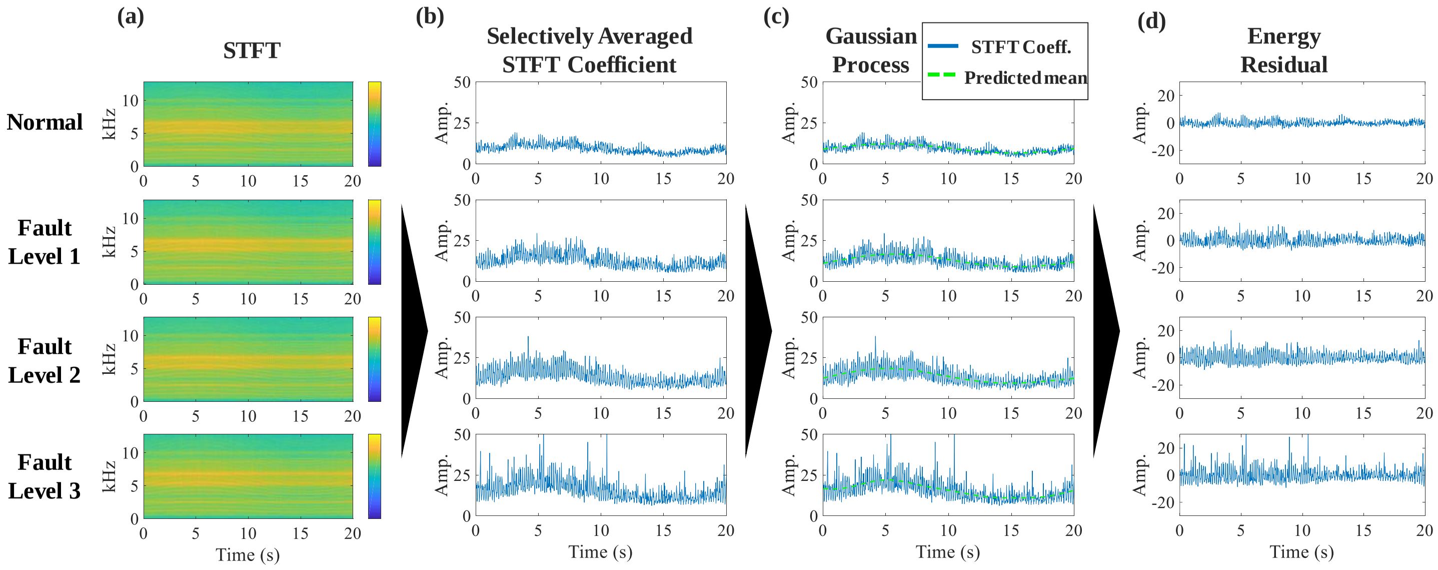

Figure 5-9 The results of the proposed PER method using the sinusoidal speed signals from the experiment in a normal and three levels of faulty states: (a) averaged wavelet coefficients, (b) GP regression, (c) ER, and (d) PER

The fault sensitivity of the proposed VER method is given in Figure 5-10(a), along with the PER method and the variance of the STFT coefficients. To calculate the fault sensitivity, we computed the average of the fault features using 10 samples of the 20-second vibration data. The sensitivity values are 1.19, 1.81, and 5.37 for the PER method; 2.58, 3.61, and 5.65 for the variance of the STFT coefficients; and 3.03, 4.46, and 7.66 for the VER method for fault levels one to three. The proposed VER method performs the best for each fault level in terms of fault sensitivity. Figure 5-10(b) shows the calculation time required for each method, which is based on 20 seconds of normal and faulty experimental vibration signals. As can be seen in Figure 5-10(b), the previous PER method showed the largest required computation time. The proposed VER method showed much better computation efficiency than the PER method; in fact, it required about 33 times less computation time. Although the variance of the STFT coefficients showed reduced computation time compared to the VER method, the variance values showed less fault sensitivity than the VER method. In addition, the effect of the variable-speed condition is not removed in the variance of the STFT coefficients.

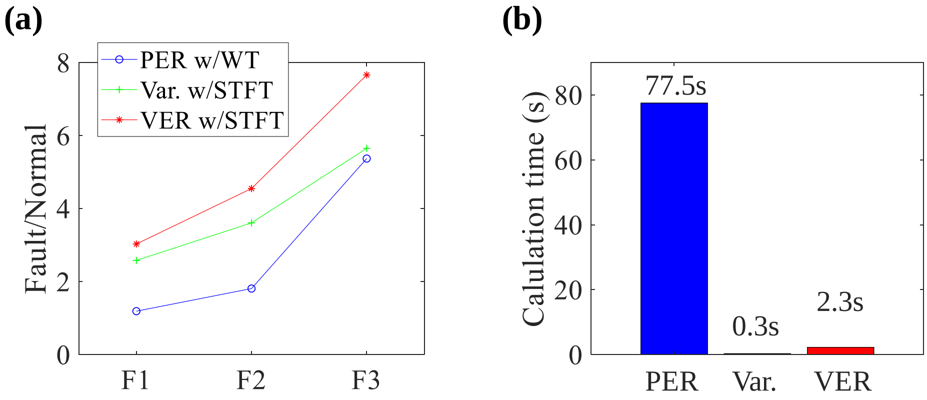

Figure 5-10 Performance of PER, Variance, and VER for experiment vibration signals: (a) fault sensitivity and (b) calculation time signals: (a) fault sensitivity and (b) calculation time

Again, we compared the fault sensitivity results of the VER method with the order-tracking method. In Figure 5-11, we could see how the faulty experiment raw signals could be resampled based on the order-tracking method. We could find that variabilities of speed in the measured signals in Figures 5-11(a) and (b) were removed after the order-tracking method as can be seen in Figures 5-11(c) and (d). Then, we calculated fault sensitivity of the order-tracking method. Figure 5-12 shows the fault sensitivity values of the order-tracking method along with the proposed VER method. In the figure, we could find that the proposed VER method shows better fault detection performance than the order-tracking method. Figure 5-13 shows ratios of kurtosis between normal and each fault level using the proposed VER methods under different noise levels. We could see that the proposed VER method shows similar results under noise levels 1 and 2, and sensitivity gets lower under noise level 3.

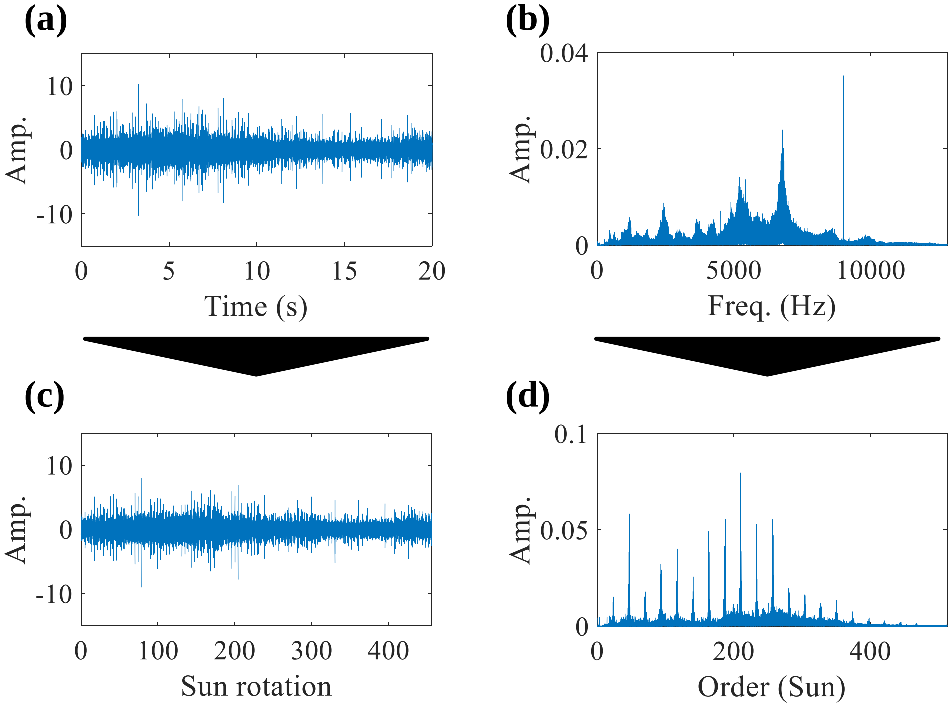

Figure 5-11 Transformation of the faulty experiment raw vibration signals into the resampled signals using the order-tracking method: (a) raw signals in time-domain, (b) raw signals in frequency-domain, (c) resampled signals in sun gear rotation-domain, and (d) resampled signals in order-domain

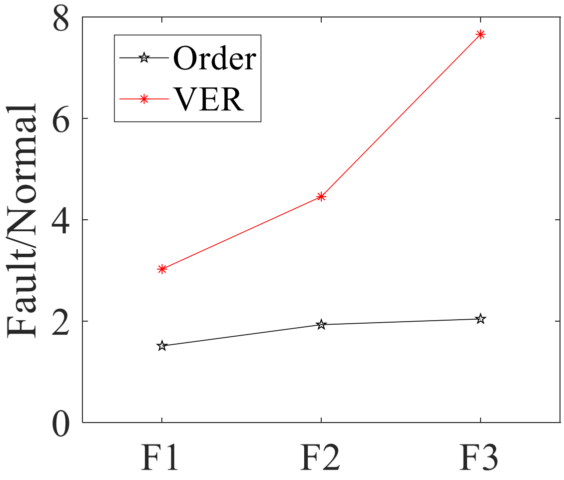

Figure 5-12 Fault sensitivity results of the order-tracking method and the proposed VER method for experiment vibration signals

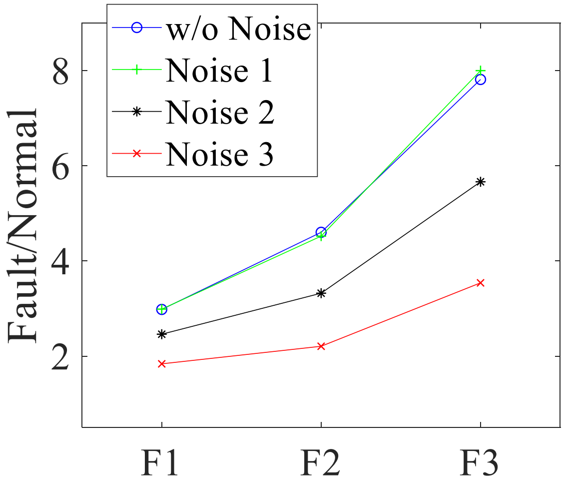

Figure 5-13 Ratios of VER values between normal and each fault level with experiment signals under different noise levels

5.4. Summary and Discussion

This chapter proposed an efficient method for fault detection of a planetary gear under variable-speed conditions. In the proposed method, first, we used STFT to express time-varying behaviors of vibration signals measured from a planetary gear. In STFT, the faulty behaviors could also be represented as the spread in the frequency domain. Next, STFT coefficients were averaged over time based on selected frequency ranges to enhance fault sensitivity. The frequency ranges were automatically selected based on the spectral kurtosis method, which find the frequency regions with the most non-Gaussian signals. Then, we used GP regression to predict the mean values of the STFT coefficients, which represent the effects of the variable-speed condition. The predicted mean values were subtracted from STFT coefficients, which results in the energy residual (ER). Finally, variance of ER (VER) was used as a fault feature to quantify the spread of the STFT coefficients in the frequency domain. The proposed VER method was found to be more efficient than other methods because the method does not use angular information, which requires an additional measuring device and further signal processing. In addition, the VER method requires less computational cost by using the STFT technique, rather than the WT technique used in the previous PER method. The calculation time of the proposed VER method was about three times less than the target signals, while the previous PER method took three time more than the target signals. From this result, we could expect the VER method would be easily applicable to online condition monitoring, which provide continuous fault detection using the measured signals. In conclusion, the proposed VER method offers the potential to reduce the computation time of the previous PER method, while showing better fault sensitivity performance. However, one drawback of the proposed method is that system characteristics must be consistent to determine the frequency range of selectively averaged STFT coefficients. Therefore, future work related to this study will include development of the VER method for the continuously varying system characteristics. In addition, we will also apply the VER method to other rotating machinery, including bearings, motors, and rotors; as well as to other variable-speed conditions like random speed fluctuations and linearly time-varying conditions. In addition, in the PER and VER methods, we need to estimate the variable-speed conditions using GP. However, the estimated speed condition could be accurate if the speed profiles are too complex. Therefore, in next chapter, we will develop a fault diagnosis method that also can be applied to complex speed profiles.

Sections of this chapter have been published as the following journal articles:

1) **J. Park**, Y. Kim, K. Na, and B. D. Youn, "Variance of energy residual (VER): An efficient method for planetary gear fault detection under variable-speed conditions," Journal of Sound and Vibration, vol. 453, pp. 253-267, 2019.

Chapter 6

Image-based Fault Feature for Complex Speed Profiles

As described in the previous section, speed estimation is performed using the GP technique in the PER and VER methods. However, the estimated speed profiles could not be accurate if the speed profile is too complex. It could lead to inaccurate fault diagnosis results. Therefore, in this chapter, I will develop the image-based fault feature which can be applied for complex speed profiles. We will first review how the time-frequency image data are represented for normal and faulty planetary gears. Then, the 2-dimensional (2-D) Fourier transform technique, which we used in the proposed fault diagnosis method, will be explained. Then, I will propose the fault feature, which can be extracted time-frequency image data. The performance of the proposed fault feature would be demonstrated using the simulation model and experiment data.

6.1. Time-frequency Image from Normal and Faulty Planetary Gears

In this section, we first analyze the time-frequency analysis results of the normal and faulty planetary gears, and compare the results. Therefore, we could investigate the faulty characteristics of the time-frequency analysis of the experiment data. Figure 6-1 shows the time-frequency analysis results of the planetary gears under variable-speed conditions. In the data, we used STFT for the time-frequency analysis, and the variable-speed profile was as described in Chapter 3.2. Although, the data is based on time- and frequency-domains, we could consider the results as 2-D image data. In the figure, we could first notice that there are sinusoidal fluctuation of the components including harmonics due to the variable-speed conditions. Next, there are natural frequency regions near 6kHz. One thing of particular note is that the vertical lines in the faulty time-frequency image data. Figure 6-2 shows the principle of the vertical lines in the time-frequency image data of the faulty vibration signals. Figure 6-2(a) shows how an impulse signal in time domain would be transformed into frequency domain by Fourier transform. As can be seen, the impulse signal is transformed into a horizontal line in the frequency domain. It can be formulated as

$$\boldsymbol{X}(f) = \int_{-\infty}^{\infty} \delta(t) e^{-i2\pi f t} dt = e^{-i2\pi f 0} = 1 \tag{6.1}$$

where $\delta(t)$ is a Dirac delta function.

Figure 6-2(b) shows how an impulse signal in time domain would be transformed into time-frequency domain by time-frequency analysis. As can be seen, the impulse signals are transformed into vertical lines in the time- frequency domain. It can be formulated as

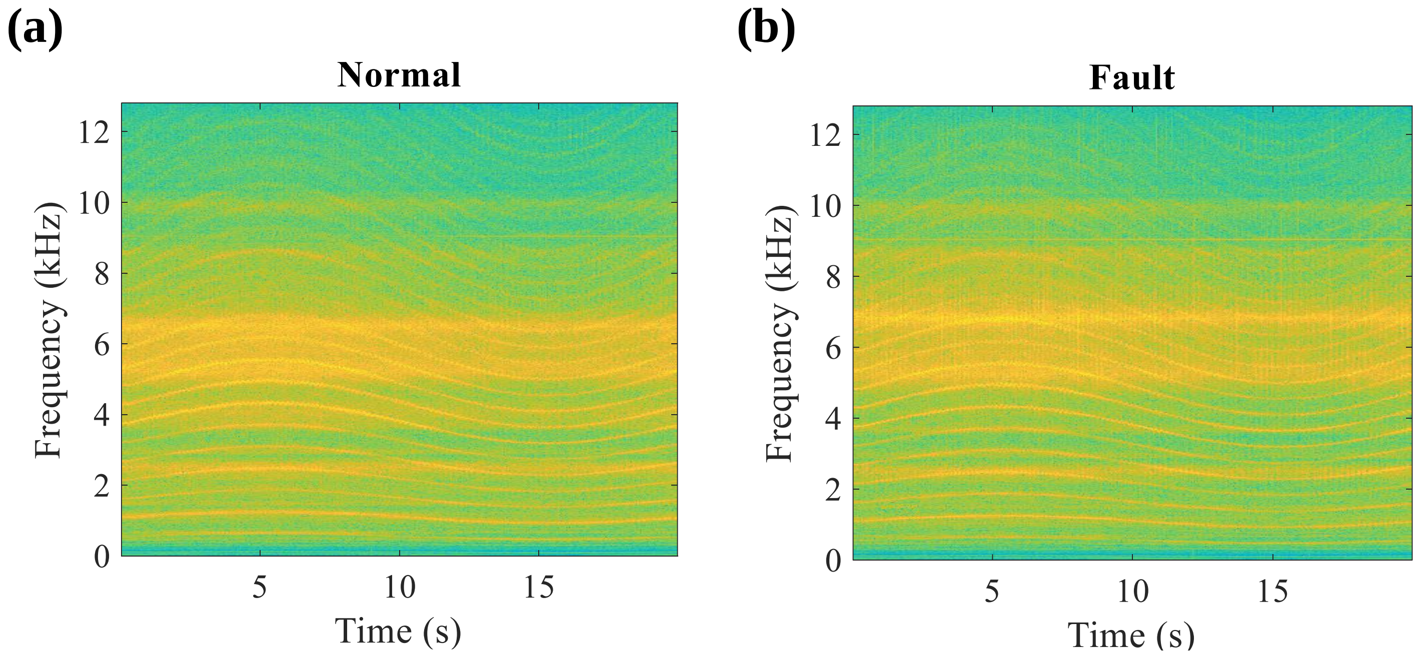

Figure 6-1 Time-frequency image data of normal and faulty planetary gears

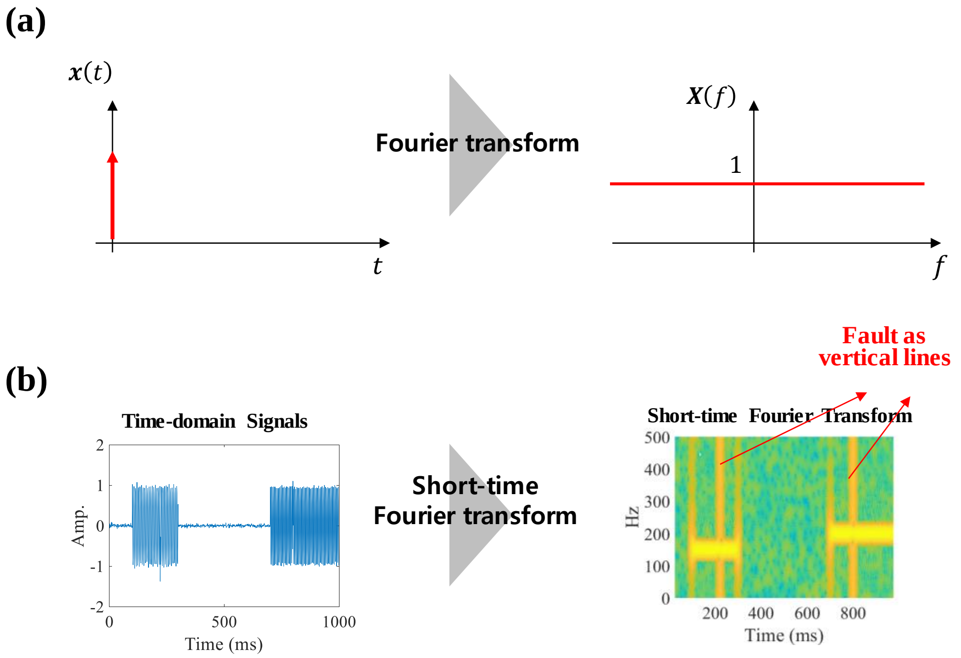

Figure 6-2 Principles of the vertical lines in time-frequency image data of faulty vibration signals: (a) Impulse signals in frequency domain, and (b) impulse signals in time-frequency domain

$$\mathrm{STFT}(\tau, f) = \int_{-\infty}^{\infty} \{x(t) + \delta(t)\} g(t-\tau) e^{-i2\pi f t} dt \tag{6.2}$$

The horizontal lines in the frequency domain would be represented as vertical lines in time-frequency domain because frequency axis is in the y-axis in the time-frequency domain. From the results, we could find that the impulsive signals in the time-domain would appear as a horizontal line in frequency domain, and vertical lines in time domain, respectively. Therefore, we could know that we need to quantify the vertical lines in the time-frequency image data to extract fault-related features in the data.

6.2. Review of 2-D Fourier Transform

In this chapter, we review the 2-D Fourier transform which we will use to quantify the vertical lines in time-frequency image data. 2-D Fourier transform is basically expansion of previous 1-D Fourier transform to two dimensions. The 2-D Fourier transform could be formulated as

$$F(u,v) = \int_{-\infty}^{\infty} f(x,y) e^{-2\pi i(ux+vy)} dxdy \tag{6.3}$$

where $f(x,y)$ is image data in x and y-domain, and *u* and *v* are spatial frequencies in *x* and *y*-domain. Thus, 2-D FT could quantify spatial frequencies in image data. Common application examples of 2-D FT are image filtering and detection [154, 155]. In Figure 6-3, we could see that the periodical patterns in background of forensic image data are represented in peaks in spatial frequency domain. Therefore, removal of these peaks could clarify the forensic original data.

Then, we will investigate how the vertical lines of image data could be transformed using the 2-D Fourier transform technique. Figure 6-4 shows how the vertical lines of image data are represented in spatial frequency domain after 2-D FT

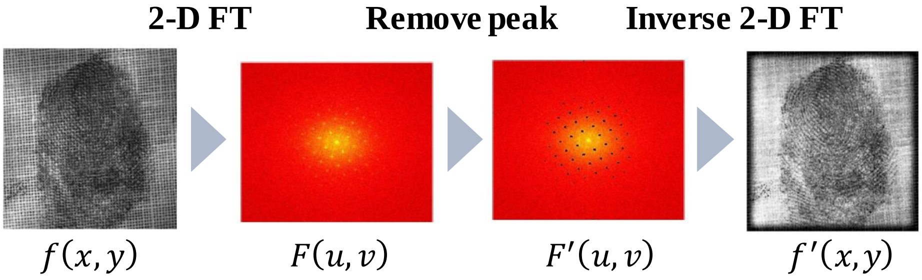

Figure 6-3 Background image filtering in forensic analysis by 2-d FT

in various situations. In Figures 6-4(a) and (b), we could observe that vertical lines could make horizontal lines in the center of spatial frequency domain while shorter length of lines could make the vertical lines more blurred in vertical direction of spatial frequency domain. Figures 6-4(c) and (d) shows how multiple vertical lines in image data are represented in spatial frequency domain. In Figure 6-4(c), we could observe that periodic multiple vertical lines make the discrete components in the horizontal center of spatial frequency domain. In Figure 6-4(d), we could observe that the discrete horizontal components get more continuous as the periodic multiple vertical lines get non-periodic. Therefore, we could find that the vertical lines in faulty gear image data could be transformed into horizontal center components in the spatial frequency domain. And, in Figure 6-5, we could know that the transformation would not be affected by other components like noises. Mathematical derivation about transformation of the vertical line images into central horizontal regions is given in Appendix.

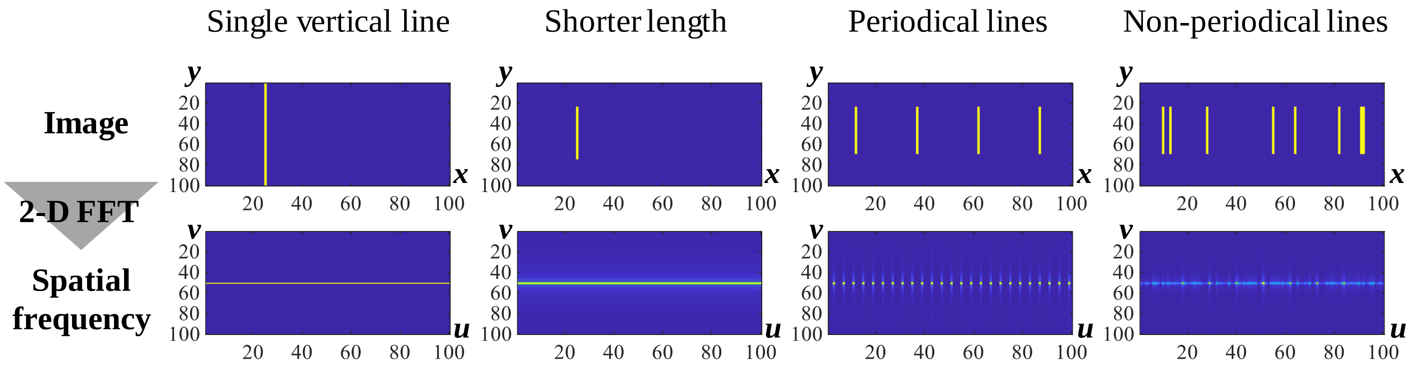

Figure 6-4 Application of 2-D FT in image data for vertical lines: (a) single vertical line, (b) single vertical line with shorter length, (c) multiple vertical lines with periodic distances, and (d) multiple vertical lines with non-periodic distances

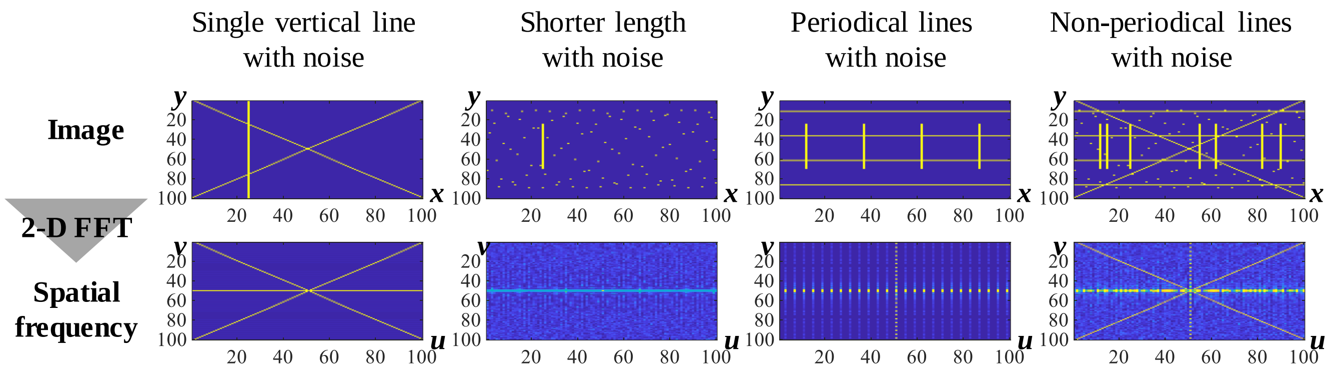

Figure 6-5 Application of 2-D FT in image data for vertical lines under noise components: (a) single vertical line with x-shaped noise, (b) single vertical line of shorter length with random noises, (c) multiple vertical lines of periodic distances with periodic horizontal line noises, and (d) multiple vertical lines of non-periodic distances with noises from (a), (b), and (c)distances

6.3. The Proposed Image-based Fault Feature

In this chapter, we will describe the proposed image-based fault feature, which uses 2-D Fourier transform to extract faulty characteristics in time-frequency image data. The method is composed of three steps, and designed to extract fault features efficiently, while not being affected by other components. The proposed fault feature is describe detailedly as follows.

6.3.1. Short-time Fourier Transform

Figure 6-6 shows the procedures of the proposed fault detection method for planetary gears under variable-speed conditions. As can be seen in the figure, first, the vibration signals are measured from normal and faulty planetary gears. We could observe that the vibration signals are modulated due to variable speed conditions. Next, time-frequency analysis is performed for the measured vibration signals to observe the change of the spectral information along the time. In this research, we used short-time Fourier transform to represent time-varying behaviors of the vibration signals. The vertical lines would appear in the short-time Fourier transform results of faulty vibration signals as fault features.

6.3.2. 2-D Fourier Transform of the Time-frequency Coefficients

Then, 2-D Fourier transform is performed for the time-frequency image data of the vibration signals. The main objective of 2-D Fourier transform in this step is to efficiently quantify vertical lines in the time-frequency image data. By using 2-D Fourier transform, the vertical lines in the time-frequency image data are transformed into horizontal center components in the spatial frequency domain as shown in Figure 6-6. And, the transformation would not be affected by other components.

6.3.3. Mean Square in the Horizontal Center Regions

Finally, the horizontal center components in the spatial frequency domain are calculated to quantify vertical lines in the time-frequency image data. For quantification, we used mean square value. We calculate ratios of mean square values between normal and each fault level, and compare the results with Haralick and LBP features to see the performance of the proposed method.

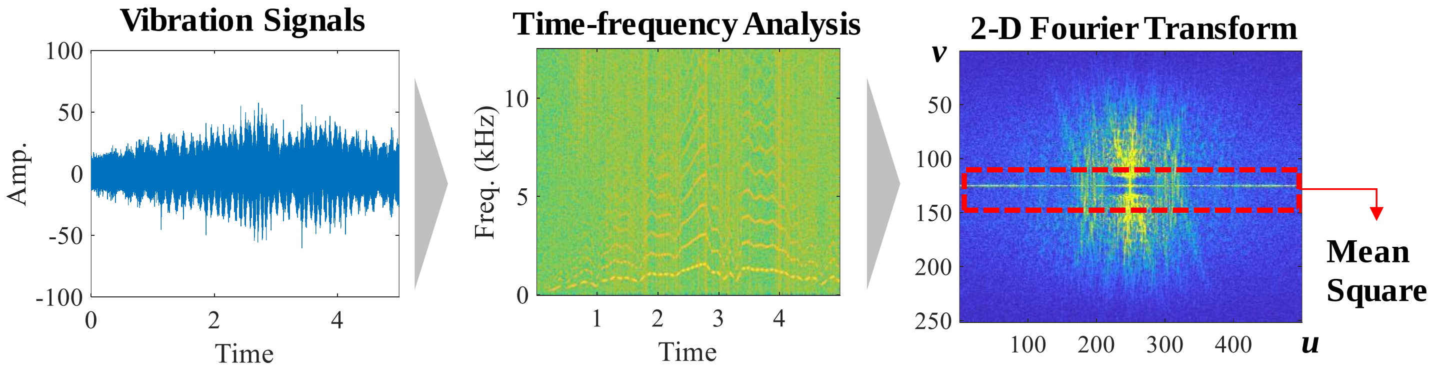

Figure 6-6 Proposed fault feature for planetary gears under variable- speed conditions using time-frequency image data

6.4. Case Studies

6.4.1. Case Study with the Simulation Model

In this section, we will validate the proposed fault feature using the simulation model. We will used the complex speed profiles as shown in Figure 6-7. As can be seen, the profiles show more complex behaviors than the speed profiles used in the previous sections. The simulated vibration signals for the normal and four different levels of faults from the speed profiles are shown in Figure 6-8. Then, we applied the proposed fault feature for the simulated signals.

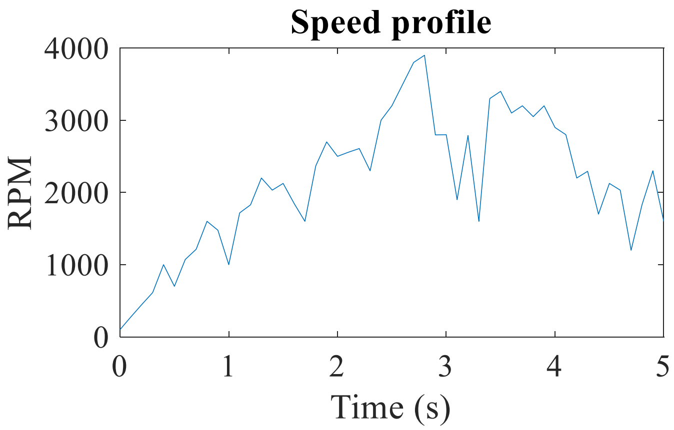

Figure 6-7 Complex speed profiles used in the simulation study

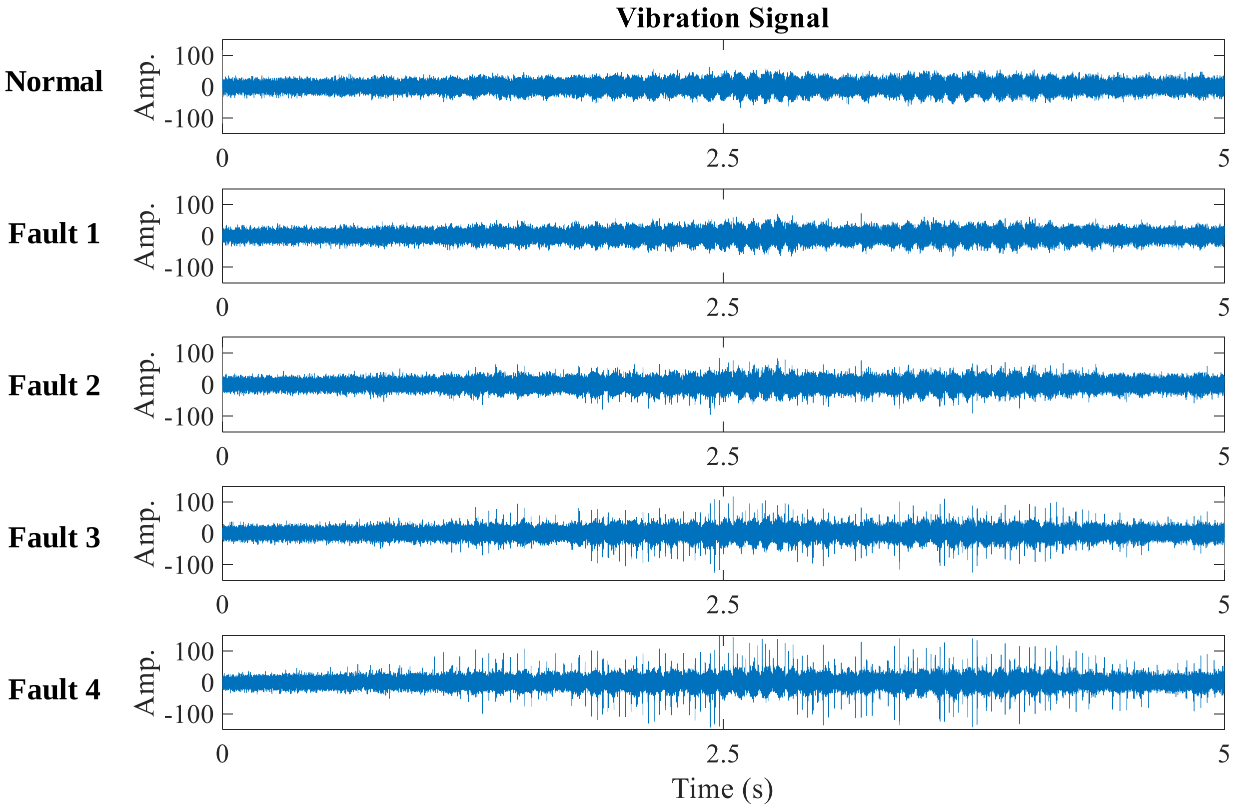

Figure 6-8 Simulated vibration signals for complex speed profiles

Figure 6-9 shows how the proposed fault feature could be extracted based on the proposed method. First, short-time Fourier transform could be performed for the vibration signals under normal and four different levels of faults. Accordingly, time-varying spectral behaviors could be represented as can be seen in the figure. Additionally, as stated in Section 6.1, the faulty behaviors are represented as the vertical lines in time-frequency domain. We could find that the vertical lines get more clear as the fault levels go higher. Then, 2-D Fourier transform is performed for the time-frequency image data. The objective of 2-D Fourier transform is to extract the faulty information in the time-frequency image data. After 2-D Fourier transform, the faulty vertical lines in time-frequency image data could be transformed into central horizontal regions in the spatial frequency domain. We could notice that the central horizontal lines get more distinct in the higher fault levels. Then, mean square values are calculated in the central horizontal regions to quantify the fault severity.

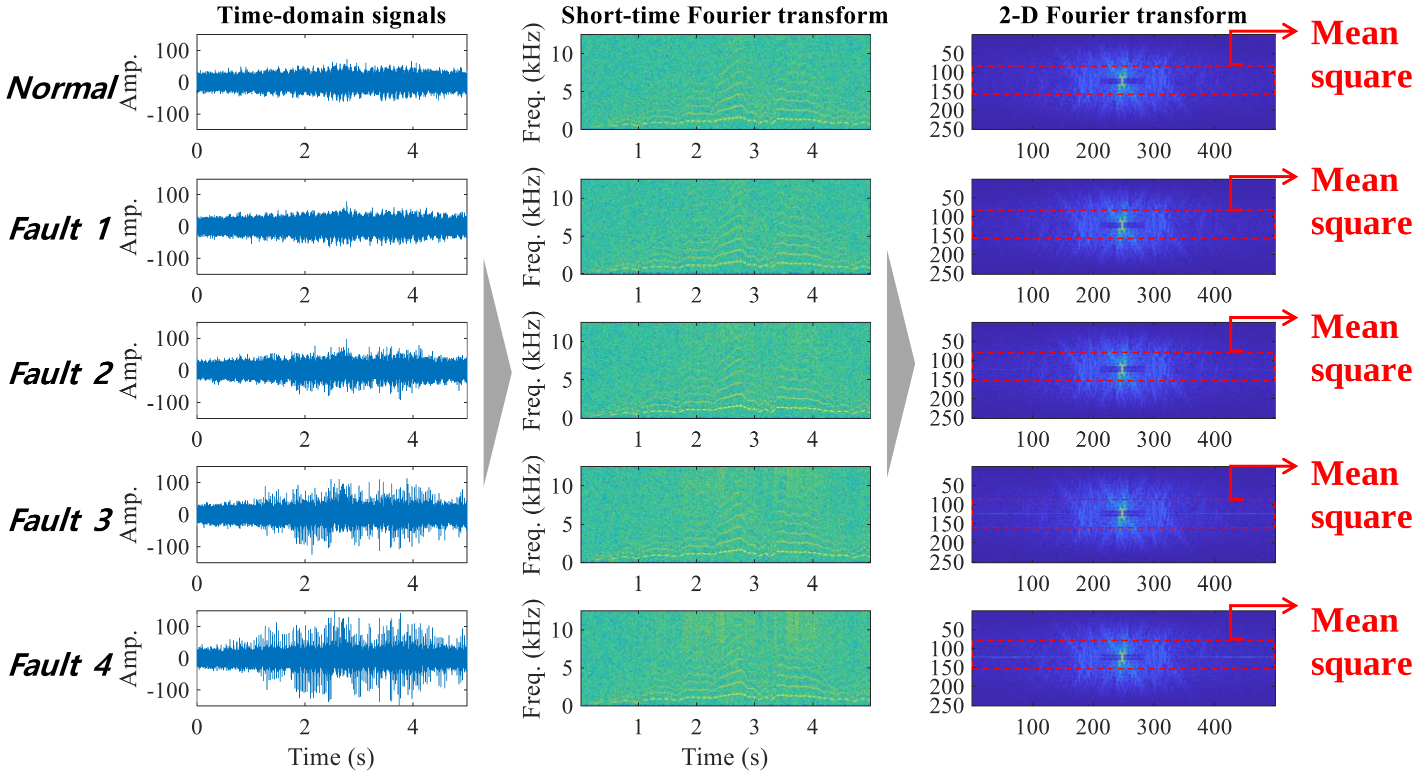

Figure 6-9 Proposed fault feature extraction for the simulated vibration signals from the complex variable-speed conditions

Figure 6-10 shows the fault sensitivity results of the proposed image-based feature along with the previous VER method results. We only used the VER results for comparison because the VER method is also based on the short-time Fourier transform results. As can be seen in the figure, we could find that the previous VER method shows non-linear results as the fault levels get higher. The non-linearity happened due to incorrect speed estimation in the VER method.

Figure 6-11 shows fault sensitivity of the proposed image-based fault feature compared with the previous texture-based feature, Haralick and LBP features. As can be seen in the figure, the proposed image-based feature shows better fault sensitivity results than the previous feature.

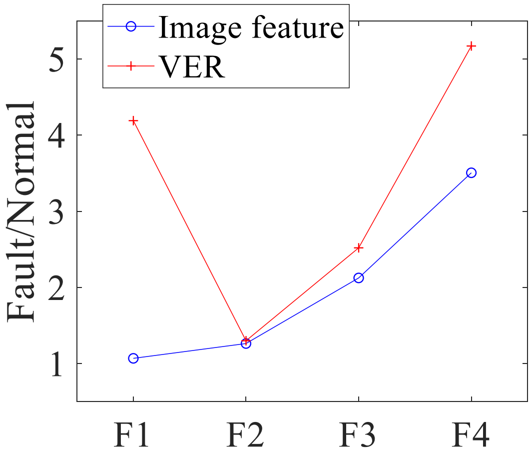

Figure 6-10 Fault sensitivity results of the image-based feature and the previous VER method for complex speed profiles used in the simulation study

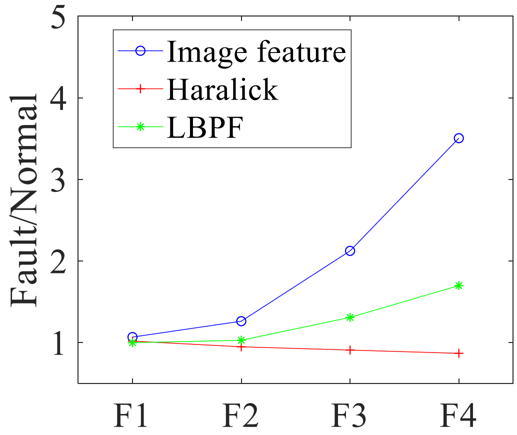

Figure 6-11 Fault sensitivity results of the image-based feature with the previous texture-based features, LBP and Haralick features

Figure 6-12 shows ratios of image feature values between normal and each fault level under different noise levels. We could see that the proposed image feature shows similar results under noise levels 1, 2, and 3.

6.4.2. Case Study with the Experiment Data

In this chapter, we will validate the proposed image-based feature using the experiment data described in Section 3.2. However, we used the different speed profiles from the one in Section 3.2 to simulate the complex speed profile. Figure 6-13 shows the speed profile we used for the experiment. As can be seen, we could find that the profile shows more fluctuation than the previous sinusoidal speed profile shown in Figure 3-7. The measured vibration signals are shown in Figure 6-14.

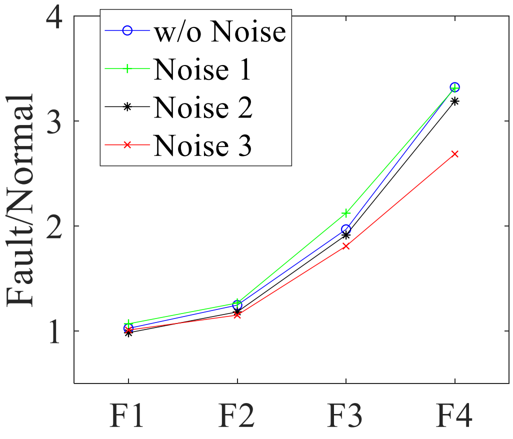

Figure 6-12 Ratios of image feature values between normal and each fault level with simulation signals under different noise levels

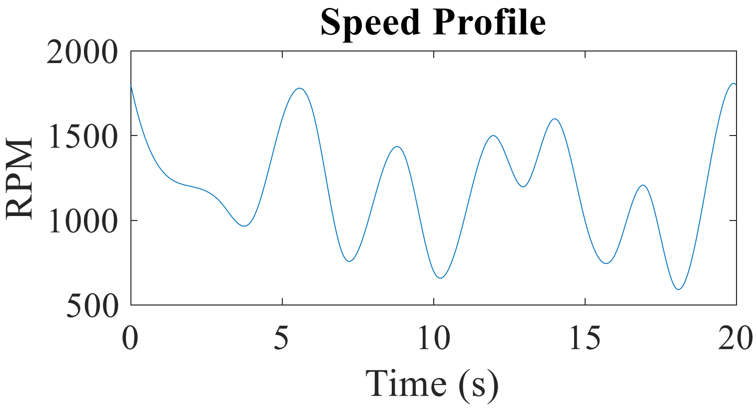

Figure 6-13 Complex speed profiles used in the experiment study

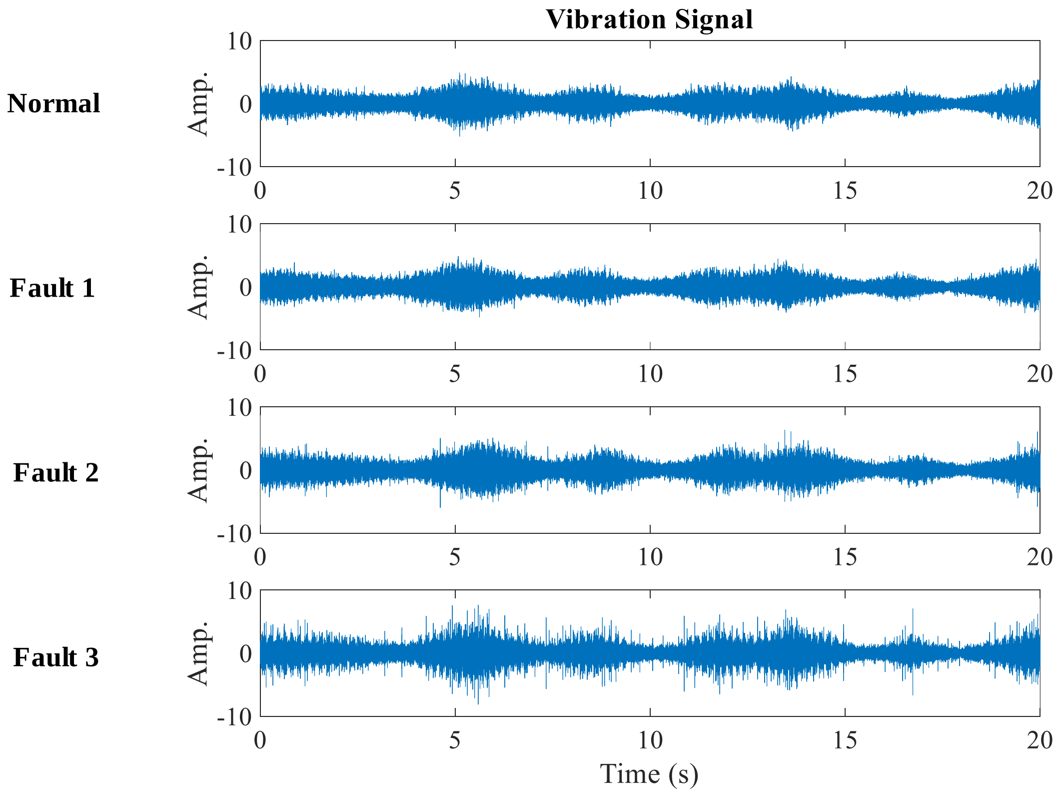

Figure 6-14 Measured experiment vibration signals under complex speed profiles for normal and three different fault levels

As can be seen in the figure, we could find that the measured vibration signals show complex behaviors. The difference between normal and fault level 1 vibration signals is not significant, but the peaked behaviors get severe as the fault level gets higher.

Then, Figure 6-15 shows the procedures of the proposed image-based fault feature for the experiment vibration signals. As explained in Section 6.3, first, short-time Fourier transform is performed for the each level of the vibration signals. In this regard, we could analyze how the spectral behaviors change along the time. In addition, the faulty behaviors in the vibration signals could be represented as vertical lines in short-time Fourier transform results. Then, 2-D Fourier transform is performed for the time-frequency image data. The 2-D Fourier transform could extract faulty information in the time-frequency image data, which is represented as vertical lines. Finally, mean square components in the central horizontal regions of the spatial frequency domain are calculated to quantify the fault severity.

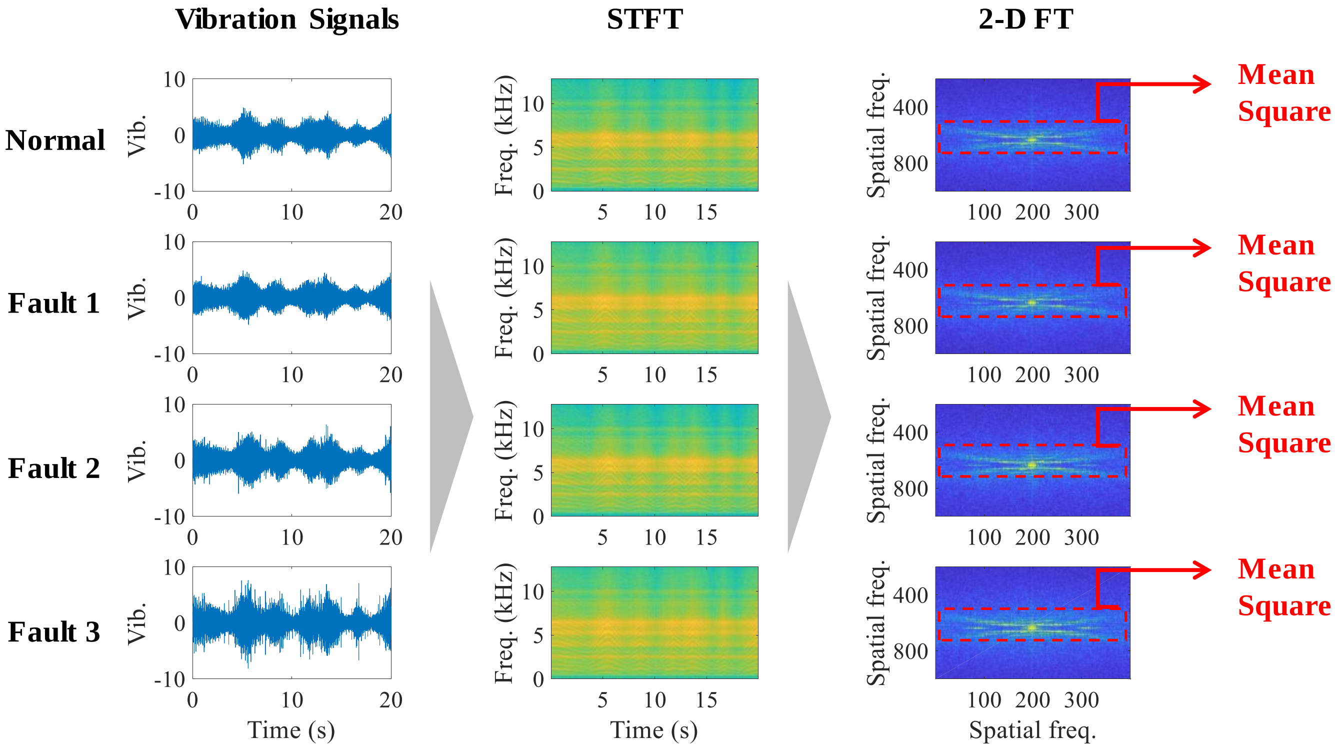

Figure 6-15 Proposed fault feature extraction for the experiment vibration signals from the complex variable-speed conditions

Figure 6-16 shows the fault sensitivity result of the proposed image-based fault feature. The values are averaged values of five 20 seconds data. As can be seen, the previous VER method shows fault sensitivity results under one at fault levels 1 and 2, which means the method could not detect the fault. This is because the speed estimation was not correct in the method. However, the proposed image-based feature shows linear behavior along the fault level as can be seen in the figure.

Then, Figure 6-17 shows fault sensitivity results of the proposed image-based feature along with previous texture-based features, LBP and Haralick features. As can be seen, the proposed feature shows better fault sensitivity results at each level.

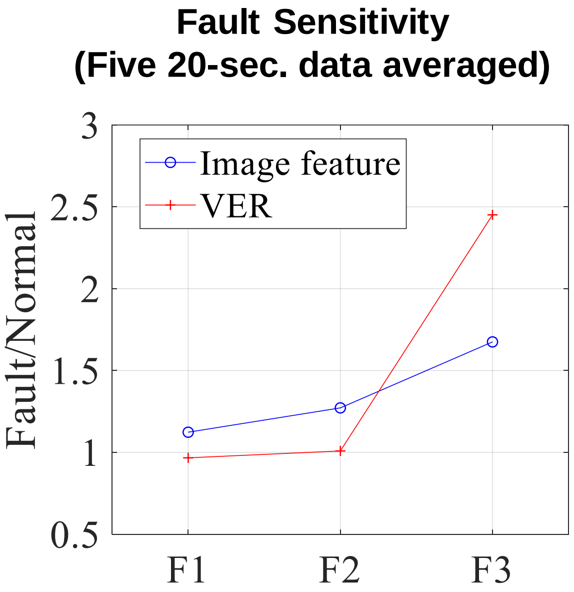

Figure 6-16 Complex speed profiles used in the experiment study

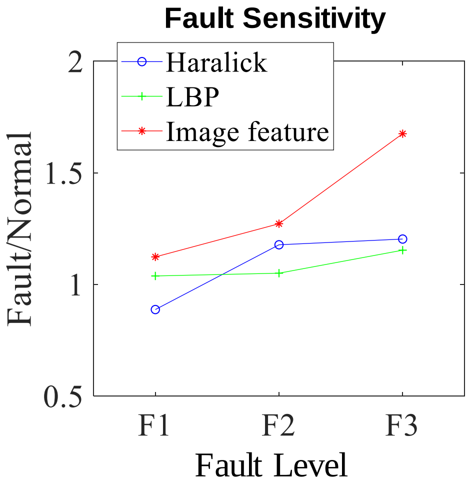

Figure 6-17 Fault sensitivity results of the image-based feature with the previous texture-based features, LBP and Haralick features for experiment signals

Figure 6-18 shows ratios of image feature values between normal and each fault level under different noise levels. We could see that the proposed image feature shows similar results under noise levels 1,2, and 3.

6.5. Summary and Discussion

In this section, we proposed the image-based fault feature for fault diagnosis of the planetary gear under complex speed profiles. The previous VER and PER methods could not be applied to the planetary gear under complex speed profiles because speed estimation in the method could not be accurate. Therefore, in this method, we developed the fault feature based on the time-frequency image data.

In the time-frequency image data, the faulty behaviors are represented as vertical

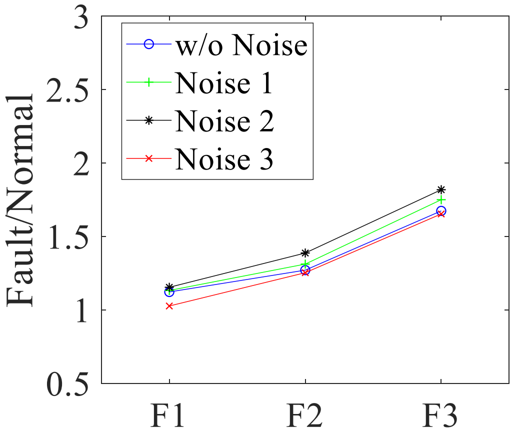

Figure 6-18 Ratios of image feature values between normal and each fault level with experiment signals under different noise levels

lines. Therefore, we used 2-D Fourier transform to efficiently extract the faulty behaviors, where the vertical lines are transformed into central horizontal lines in the spatial frequency domain. Then, mean square values are calculated to quantify the faulty severity of the planetary gears.

However, as noted in Figure 6-2, this method would be only applicable to the faults with impact signals. Therefore, future works of the method would include development of the fault features, which could be applied to other types of faults like crack and shaft error. In addition, we will apply the proposed method to other applications like other rotating machinery and medical signals.

Chapter 7

Conclusions

7.1. Contributions and Significance

In this dissertation, I proposed fault diagnosis methods for planetary gears under variable-speed conditions using time-frequency analysis. This research is composed of three parts: 1) Positive energy residual (PER) method for enhanced fault sensitivity by minimizing effects of variable-speed conditions, 2) Variance of energy residual (VER) method for computational efficiency using time-efficient time-frequency analysis, 3) Image-based fault feature for complex speed profiles. The contribution and significance of the proposed research can be highlighted as follows.

First, we could enhance fault sensitivity for diagnosis of the planetary gear by minimizing the effects of variable-speed conditions. In the proposed method, the Morlet wavelet transform (WT) could extract faulty information, while representing time-varying spectral behaviors. Then, the Gaussian process (GP) could predict averaged variable speed conditions using the averaged wavelet coefficients. Next, energy residual (ER) could be calculated by subtracting predicted GP components from the averaged wavelet coefficients. Then, the positive portions of the ER (PER) are taken to enhance fault sensitivity. The previous methods developed for constant speed conditions show low fault sensitivity due to time-varying behaviors of the variable-speed conditions. Although the angular resampling technique could reduce the effects from variable-speed conditions, the technique require angular data from an encoder, which needs additional devices and signal processing. However, the proposed PER method does not need other devices but the accelerometer.

Second, we could develop time-efficient diagnostic methods, called a variance of energy residual (VER) method. The WT could require huge computation time to analyze vibration data with wider frequency range, which is a mandatory condition for fault diagnosis. Therefore, in the VER method, short-time Fourier transform (STFT) is used as time-frequency analysis instead of WT. the STFT could reduce computation time by selecting appropriate window lengths for the analysis. However, fault sensitivity could be reduced in using the STFT technique. Therefore, selective regions are used for averaging the time-frequency components to compensate reduced fault sensitivity. The selection could be performed based on spectral kurtosis technique. Finally, variance values are used to quantify fault severity instead of kurtosis because faulty behaviors are represented as spread in the frequency domain in the STFT results. The VER method could reduce computation time from the previous PER method while maintaining fault sensitivity if we have system characteristic information.

Third, we develop an image-based fault feature for complex speed profiles. The previous PER and VER method include a speed estimation step using the GP technique. However, the estimated speed profile could not be accurate if the speed condition have complex profiles. Therefore, we developed the fault feature independent of speed profiles. The method could extract fault feature in time-frequency image data, and not be affected by speed conditions. First, time-frequency analysis is performed for measured vibration signals. The faulty impulsive signals are represented as vertical lines in time-frequency image data. Then, 2-D Fourier transform is performed to quantify the vertical lines in time-frequency image data. Finally, mean square values are used to quantify fault severity of the signals. The image-based feature could show better fault sensitivity than the previous fault features, and robust performance for the planetary gears under complex speed profiles.

In this dissertation, we proposed three different fault diagnosis methods for planetary gears under variable-speed conditions. The PER method could enhance fault sensitivity by minimizing effects from variable-speed conditions. And, the VER method could reduce computation time from the PER method while maintaining fault sensitivity. However, we need to know system characteristics, and the system characteristics is needed to be constant during the operation of the planetary gear. Finally, the image-based fault feature could be applied to the planetary gears with complex speed profiles. In conclusion, we developed the fault diagnosis methods for planetary gears under variable-speed conditions, that best suit each case.

7.2. Suggestions for Future Research

This dissertation proposed three fault diagnostic methods for planetary gears under variable speed conditions for each case. However, there are still some points that can be improved further for the future research.

- Basically, the proposed methods are based on extracting fault features under same speed conditions. In this regard, the proposed methods could not be applied to random fluctuation of speed profiles, or the test signals should have the same speed profiles with the reference normal signals. therefore, we need to develop fault detection and diagnosis methods that can be applied to random speed fluctuation, or different speed profiles of planetary gears.

- In the experimental setup, the only variable in the test was a speed condition. The other conditions like torque, temperature were maintained constant during the tests. However, in real-world situations, the other conditions should also be show highly non-linear behaviors. therefore, we need to develop fault diagnosis methods that also can consider other non-stationary conditions.

- The proposed methods were validated using vibration signals from simulation and well-controlled test-bed data. Accordingly, the performance of the proposed methods was proven to be effective, and linear for each fault level. However, vibration signals measured from real-world conditions should be highly contaminated by noises, and faulty signals could be covered by other components. Therefore, the proposed method should be also validated by using vibration signals of planetary gears measured from real-world applications.

- The proposed methods were validated using the three different levels of planet gear surface faults. However, in the planetary gear, the faults could occur in different gears like sun gear, ring gear, and also carriers. Moreover, the fault types could be different. The other fault types include tooth root crack, misalignment, shaft run-out error, and so on. Therefore, the proposed methods should also be validated using the other types of fault cases.

- The methods used the characteristics of vibration signals under faulty conditions. Specifically, we used the time-frequency behaviors of the impulsive vibration signals. These impulsive faulty vibration signals are usually common in faults in other types of rotating machinery applications. Therefore, we expect the proposed method in this dissertation could be applied to other applications like motors, bearings, rotors, and so on.

- All the methods proposed in this thesis are basically based on the time-frequency analysis, and the data calcualted from the time-frequecy anaylysis are 2-d image data. Recently, extensive research have been performed using image data for classification problems. Especially, deep learning techniques like CNN are known to show outstaning performances for image classification problems. Therefore, fault sensitivity of the proposed methods could be further enhanced by combining the methods with deep learning techqniues.

Appendix

This section will describe mathematical derivation about how the vertical line image data could be transformed into central horizontal regions in the spatial frequency domain, which is given in Figure 6-4. Figure A-1 shows how the single vertical line image could be transformed by 2-D Fourier transform. As can be seen in the figure, the vertical line could be expressed as multiplication of Dirac delta function in the x-domain and horizontal line in the y-domain. Then, Fourier transform of each signal could be transformed into horizontal line and Dirac delta function in frequency domain. Therefore, the single vertical line could be transformed into single horizontal line in the spatial frequency domain.

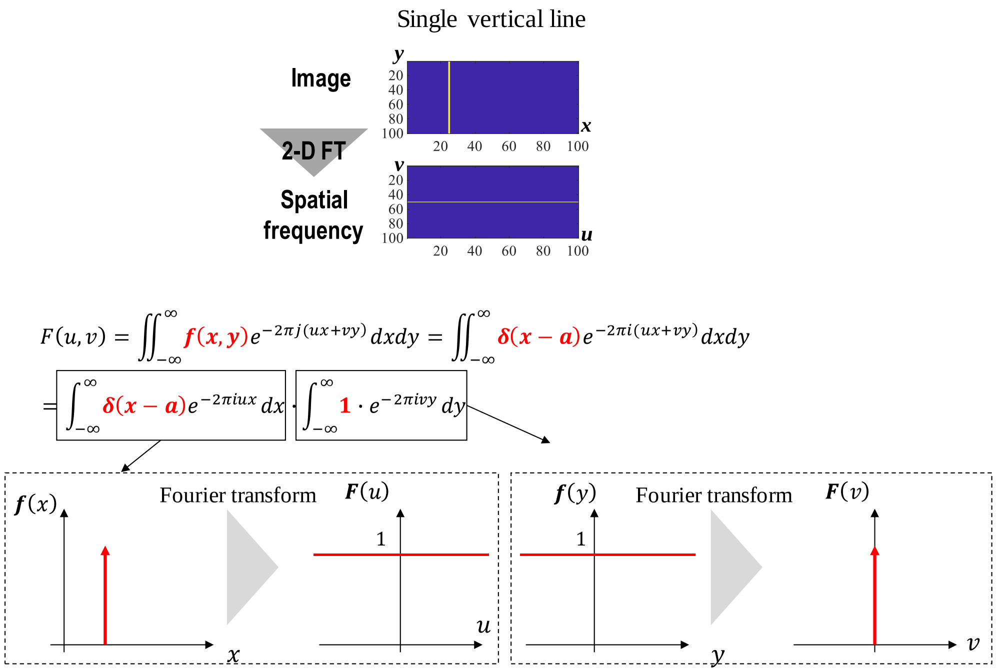

$$F(u,v) = \iint_{-\infty}^{\infty} \boldsymbol{f(x,y)} e^{-2\pi j(ux+vy)}\,dxdy = \iint_{-\infty}^{\infty} \boldsymbol{\delta(x-a)} e^{-2\pi i(ux+vy)}\,dxdy$$

$$= \boxed{\int_{-\infty}^{\infty} \boldsymbol{\delta(x-a)} e^{-2\pi iux}\,dx} \cdot \boxed{\int_{-\infty}^{\infty} \boldsymbol{1} \cdot e^{-2\pi ivy}\,dy}$$

Figure A-1 Mathematical derivation about how the single vertical line could be transformed into spatial frequency domain

Figure A-2 shows how the single vertical line image with shorter length could be transformed by 2-D Fourier transform. As can be seen in the figure, the vertical line could be expressed as multiplication of Dirac delta function in the x-domain and step rectangular function in the y-domain. Then, Fourier transform of each signal could be transformed into horizontal line and sinc function in frequency domain. Therefore, the single vertical line with shorter length could be transformed into central horizontal components in the spatial frequency domain. However, the behaviors are different from the previous single line with full length. Due to the shorter length, the central horizontal regions appear as more blurred images in the spatial frequency domain. Nevertheless, we could know that the vertical line image data with shorter length is also transformed into central horizontal components in spatial frequency domain.

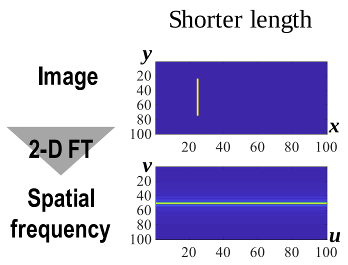

$$F(u,v) = \iint_{-\infty}^{\infty} \boldsymbol{f(x,y)} e^{-2\pi j(ux+vy)}\,dxdy = \iint_{-\infty}^{\infty} \boldsymbol{\delta(x-a)}\mathbf{rect}(\boldsymbol{y}) e^{-2\pi i(ux+vy)}\,dxdy$$

$$= \boxed{\int_{-\infty}^{\infty} \boldsymbol{\delta(x-a)} e^{-2\pi iux}\,dx} \cdot \boxed{\int_{-\infty}^{\infty} \mathbf{rect}(\boldsymbol{y}) \cdot e^{-2\pi ivy}\,dy}$$

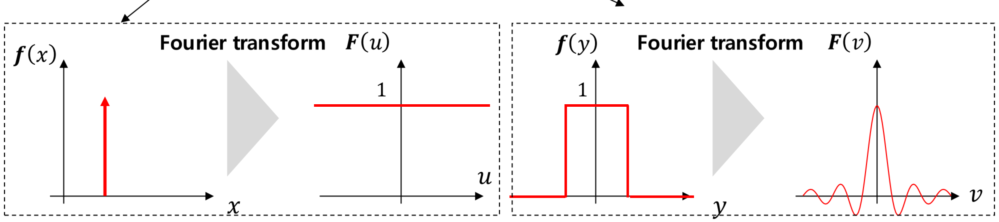

Figure A-2 Mathematical derivation about how the single vertical line with shorter length could be transformed into spatial frequency domain

Figure A-3 shows the periodic vertical lines with shorter length could be transformed by 2-D Fourier transform. The periodical vertical lines could be expressed as multiplication of Dirac comb function in the x-domain and rectangular step function in the y-domain. Then, Fourier transform of each signal could be transformed into Dirac comb function and sinc function in frequency domain. Therefore, the periodic vertical lines with shorter length could be transformed into periodic central horizontal components in the spatial frequency domain. As same as in the previous cases, we could know that the vertical line image data are also transformed into central horizontal components in spatial frequency domain.

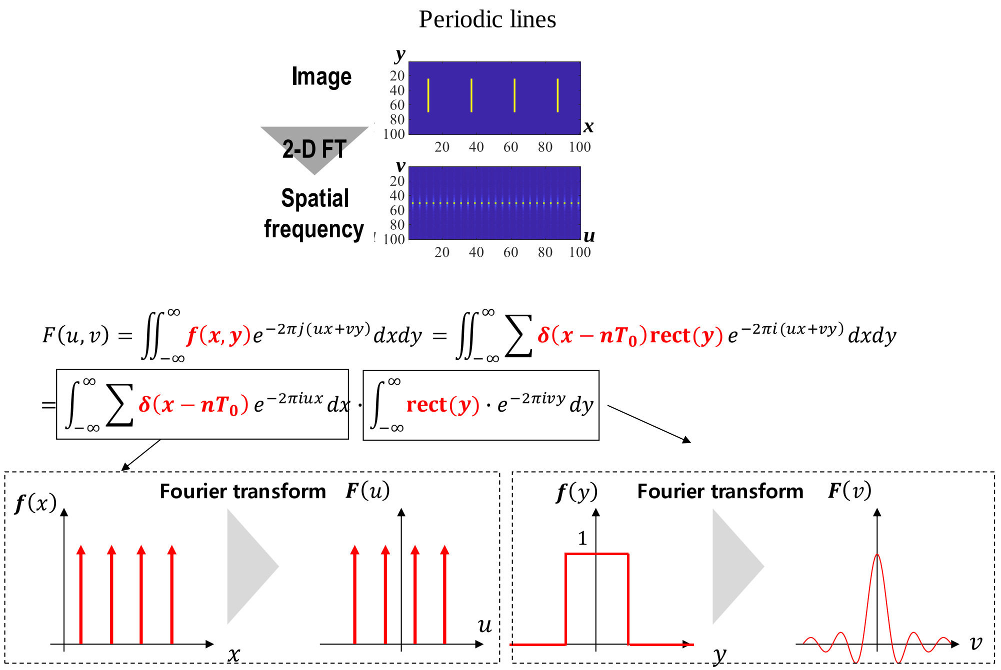

$$F(u,v)=\iint_{-\infty}^{\infty}f(x,y)e^{-2\pi j(ux+vy)}dxdy=\iint_{-\infty}^{\infty}\sum\delta(x-nT_0)\mathbf{rect}(y)\,e^{-2\pi i(ux+vy)}dxdy$$

$$=\boxed{\int_{-\infty}^{\infty}\sum\delta(x-nT_0)\,e^{-2\pi iux}dx}\cdot\boxed{\int_{-\infty}^{\infty}\mathbf{rect}(y)\cdot e^{-2\pi ivy}dy}$$

Figure A-3 Mathematical derivation about how the periodic vertical lines with shorter length could be transformed into spatial frequency domain

Figure A-4 shows the non-periodic vertical lines with shorter length could be transformed by 2-D Fourier transform. The non-periodic vertical lines could expressed as the components between single Dirac delta function and Dirac comb function. Therefore, the Fourier transform of the non-periodic vertical lines should be the components between horizontal lines and Dirac comb function. Therefore, the 2-D Fourier transform results of the non-period line image data should be about blurred image in the central horizontal components in the spatial frequency domain.

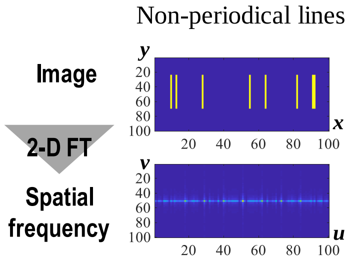

$$F(u,v) = \iint_{-\infty}^{\infty} \boldsymbol{f(x,y)} e^{-2\pi j(ux+vy)}\,dxdy = \iint_{-\infty}^{\infty} \{\boldsymbol{\delta(x-a)} + \boldsymbol{\delta(x-b)} + \cdots\}\mathbf{rect}(\boldsymbol{y}) e^{-2\pi i(ux+vy)}\,dxdy$$

$$= \boxed{\int_{-\infty}^{\infty} \sum \{\boldsymbol{\delta(x-a)} + \boldsymbol{\delta(x-b)} + \cdots\} e^{-2\pi iux}\,dx} \cdot \boxed{\int_{-\infty}^{\infty} \mathbf{rect}(\boldsymbol{y}) \cdot e^{-2\pi ivy}\,dy}$$

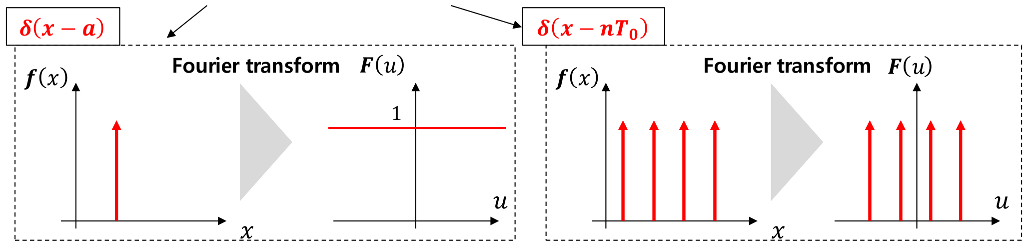

Figure A-4 Mathematical derivation about how the non-periodical vertical lines with shorter length could be transformed into spatial frequency domain

Reference

[1] F. Chaari, T. Fakhfakh, and M. Haddar, "Dynamic analysis of a planetary gear failure caused by tooth pitting and cracking," *Journal of Failure Analysis and Prevention,* vol. 6, pp. 73-78, 2006.

[2] R. Errichello and J. Muller, *Gearbox Reliability Collaborative Gearbox 1: Failure Analysis Report*: National Renewable Energy Laboratory, 2012.

[3] D. G. Astridge, "Helicopter transmissions—Design for safety and reliability," *Proceedings of the Institution of Mechanical Engineers, Part G: Journal of Aerospace Engineering,* vol. 203, pp. 123-138, 1989.

[4] J. Yoon, D. He, and B. Van Hecke, "On the use of a single piezoelectric strain sensor for wind turbine planetary gearbox fault diagnosis," *IEEE Transactions on Industrial Electronics,* vol. 62, pp. 6585-6593, 2015.

[5] J. Park, J. M. Ha, H. Oh, B. D. Youn, J. H. Choi, and N. H. Kim, "Model-based fault diagnosis of a planetary gear: A novel approach using transmission error," *IEEE Transactions on Reliability,* vol. 65, pp. 1830-1841, 2016.

[6] K. R. Al-Balushi and B. Samanta, "Gear fault diagnosis using energy-based features of acoustic emission signals," *Proceedings of the Institution of Mechanical Engineers, Part I: Journal of Systems and Control Engineering,*

vol. 216, pp. 249-263, 2002.

[7] J. Park, J. M. Ha, H. Oh, B. D. Youn, S. Park, and J.-H. Choi, "Experimental Approach for Estimating Mesh Stiffness in Faulty States of Rotating Gear," in *Proc. Annual Conference of the Prognostics and Health Management Society*, Sand Diego, CA, 2015, pp. 618-624.

[8] Y. Lei, D. Kong, J. Lin, and M. J. Zuo, "Fault detection of planetary gearboxes using new diagnostic parameters," *Measurement Science and Technology,* vol. 23, p. 055605, 2012.

[9] D. Remond and J. Mahfoudh, "From transmission error measurements to angular sampling in rotating machines with discrete geometry," *Shock and vibration,* vol. 12, pp. 149-161, 2005.

[10] K. Mao, "An approach for powertrain gear transmission error prediction using the non-linear finite element method," *Proceedings of the Institution of Mechanical Engineers, Part D: Journal of Automobile Engineering,* vol. 220, pp. 1455-1463, 2006.

[11] F. Chaari, W. Baccar, M. S. Abbes, and M. Haddar, "Effect of spalling or tooth breakage on gearmesh stiffness and dynamic response of a one-stage spur gear transmission," *European Journal of Mechanics - A/Solids,* vol. 27, pp. 691-705, 2008.

[12] R. B. Randall, "A new method of modeling gear faults," *Journal of Mechanical Design-Transactions of the ASME,* vol. 104, pp. 259-267, 1982.

[13] W. Wang and A. K. Wong, "Autoregressive model-based gear fault diagnosis," *Journal of vibration and acoustics,* vol. 124, pp. 172-179, 2002.

[14] Z. Man, W. Wang, S. Khoo, and J. Yin, "Optimal sinusoidal modelling of gear mesh vibration signals for gear diagnosis and prognosis," *Mechanical systems and signal processing,* vol. 33, pp. 256-274, 2012.

[15] H. Endo and R. Randall, "Enhancement of autoregressive model based gear tooth fault detection technique by the use of minimum entropy deconvolution filter," *Mechanical Systems and Signal Processing,* vol. 21, pp. 906-919, 2007.

[16] J. M. Ha, B. D. Youn, H. Oh, B. Han, Y. Jung, and J. Park, "Autocorrelation-based time synchronous averaging for condition monitoring of planetary gearboxes in wind turbines," *Mechanical Systems and Signal Processing,* vol. 70-71, pp. 161-175, 2016.

[17] J. M. Ha, J. Park, K. Na, Y. Kim, and B. D. Youn, "Toothwise Fault Identification for a Planetary Gearbox Based on a Health Data Map," *IEEE Transactions on Industrial Electronics,* vol. 65, pp. 5903-5912, 2018.

[18] P. McFadden and J. Smith, "An explanation for the asymmetry of the modulation sidebands about the tooth meshing frequency in epicyclic gear vibration," *Proceedings of the Institution of Mechanical Engineers, Part C: Journal of Mechanical Engineering Science,* vol. 199, pp. 65-70, 1985.

[19] G. Bi, J. Chen, F. Zhou, and J. He, "Application of slice spectral correlation

density to gear defect detection," *Proceedings of the Institution of Mechanical Engineers, Part C: Journal of Mechanical Engineering Science,* vol. 220, pp. 1385-1392, 2006.

[20] W. D. Mark, H. Lee, R. Patrick, and J. D. Coker, "A simple frequency-domain algorithm for early detection of damaged gear teeth," *Mechanical Systems and Signal Processing,* vol. 24, pp. 2807-2823, 2010.

[21] W. D. Mark, "Stationary transducer response to planetary-gear vibration excitation II: Effects of torque modulations," *Mechanical Systems and Signal Processing,* vol. 23, pp. 2253-2259, 2009.

[22] B. Zhang, T. Khawaja, R. Patrick, and G. Vachtsevanos, "Blind deconvolution denoising for helicopter vibration signals," *IEEE/ASME Transactions on Mechatronics,* vol. 13, pp. 558-565, 2008.

[23] T. Barszcz and R. B. Randall, "Application of spectral kurtosis for detection of a tooth crack in the planetary gear of a wind turbine," *Mechanical Systems and Signal Processing,* vol. 23, pp. 1352-1365, 2009.

[24] R. Zimroz and W. Bartelmus, "Gearbox condition estimation using cyclo-stationary properties of vibration signal," in *Key Engineering Materials*, 2009, pp. 471-478.

[25] Y. Lei, D. Han, J. Lin, and Z. He, "Planetary gearbox fault diagnosis using an adaptive stochastic resonance method," *Mechanical Systems and Signal Processing,* vol. 38, pp. 113-124, 2013.

[26] R. Randall, "Detection and diagnosis of incipient bearing failure in helicopter gearboxes," *Engineering Failure Analysis,* vol. 11, pp. 177-190, 2004.

[27] D. M. Blunt and J. A. Keller, "Detection of a fatigue crack in a UH-60A planet gear carrier using vibration analysis," *Mechanical Systems and Signal Processing,* vol. 20, pp. 2095-2111, 2006.

[28] M. E. Orchard and G. J. Vachtsevanos, "A particle filtering approach for on-line failure prognosis in a planetary carrier plate," *International Journal of Fuzzy Logic and Intelligent Systems,* vol. 7, pp. 221-227, 2007.

[29] J. Park, B. Jeon, J. Park, J. Cui, M. Kim, and B. D. Youn, "Failure prediction of a motor-driven gearbox in a pulverizer under external noise and disturbance," *SMART STRUCTURES AND SYSTEMS,* vol. 22, pp. 185-192, 2018.

[30] S. Xue and I. Howard, "Torsional vibration signal analysis as a diagnostic tool for planetary gear fault detection," *Mechanical Systems and Signal Processing,* vol. 100, pp. 706-728, 2/1/ 2018.

[31] C. Liu, G. Cheng, X. Chen, and Y. Pang, "Planetary gears feature extraction and fault diagnosis method based on VMD and CNN," *Sensors,* vol. 18, p. 1523, 2018.

[32] G. D'Elia, E. Mucchi, and M. Cocconcelli, "On the identification of the angular position of gears for the diagnostics of planetary gearboxes,"

Mechanical Systems and Signal Processing, vol. 83, pp. 305-320, 2017/01/15/ 2017.

[33] Z. Feng, X. Chen, and M. Liang, "Joint envelope and frequency order spectrum analysis based on iterative generalized demodulation for planetary gearbox fault diagnosis under nonstationary conditions," *Mechanical Systems and Signal Processing,* vol. 76, pp. 242-264, 2016.

[34] S.-J. Tsai, G.-L. Huang, and S.-Y. Ye, "Gear meshing analysis of planetary gear sets with a floating sun gear," *Mechanism and Machine Theory,* vol. 84, pp. 145-163, 2// 2015.

[35] X. Liang, M. J. Zuo, and L. Liu, "A windowing and mapping strategy for gear tooth fault detection of a planetary gearbox," *Mechanical Systems and Signal Processing,* vol. 80, pp. 445-459, 2016.

[36] J. Parra and C. M. Vicuña, "Two methods for modeling vibrations of planetary gearboxes including faults: Comparison and validation," *Mechanical Systems and Signal Processing,* vol. 92, pp. 213-225, 8// 2017.

[37] X. Liang, M. J. Zuo, and M. Pandey, "Analytically evaluating the influence of crack on the mesh stiffness of a planetary gear set," *Mechanism and Machine Theory,* vol. 76, pp. 20-38, 2014.

[38] Z. Feng and M. J. Zuo, "Vibration signal models for fault diagnosis of planetary gearboxes," *Journal of Sound and Vibration,* vol. 331, pp. 4919-4939, 2012.

[39] Z. Chen and Y. Shao, "Dynamic simulation of planetary gear with tooth root crack in ring gear," *Engineering Failure Analysis,* vol. 31, pp. 8-18, 2013.

[40] Z. Chen and Y. Shao, "Dynamic features of a planetary gear system with tooth crack under different sizes and inclination angles," *Journal of Vibration and Acoustics,* vol. 135, p. 031004, 2013.

[41] A. Singh, "Load sharing behavior in epicyclic gears: physical explanation and generalized formulation," *Mechanism and Machine Theory,* vol. 45, pp. 511-530, 2010.

[42] Z. Feng, X. Chen, and M. J. Zuo, "Induction Motor Stator Current AM-FM Model and Demodulation Analysis for Planetary Gearbox Fault Diagnosis," *IEEE Transactions on Industrial Informatics,* 2018.

[43] Y. Zhang, W. Lu, and F. Chu, "Planet gear fault localization for wind turbine gearbox using acoustic emission signals," *Renewable Energy,* vol. 109, pp. 449-460, 2017.

[44] D. Peng, W. A. Smith, P. Borghesani, R. B. Randall, and Z. Peng, "Comprehensive planet gear diagnostics: Use of transmission error and mesh phasing to distinguish localised fault types and identify faulty gears," *Mechanical Systems and Signal Processing,* vol. 127, pp. 531-550, 2019.

[45] L. Hong and J. S. Dhupia, "A time-domain fault detection method based on an electrical machine stator current measurement for planetary gear-sets," in *2013 IEEE/ASME International Conference on Advanced Intelligent*

Mechatronics, 2013, pp. 1631-1636.

[46] G. He, K. Ding, W. Li, and X. Jiao, "A novel order tracking method for wind turbine planetary gearbox vibration analysis based on discrete spectrum correction technique," *Renewable Energy,* vol. 87, pp. 364-375, 2016.

[47] K. Feng, K. Wang, M. Zhang, Q. Ni, and M. Zuo, "A diagnostic signal selection scheme for planetary gearbox vibration monitoring under non-stationary operational conditions," *Measurement Science and Technology,* 2016.

[48] Y. Li, K. Ding, G. He, and X. Jiao, "Non-stationary vibration feature extraction method based on sparse decomposition and order tracking for gearbox fault diagnosis," *Measurement,* vol. 124, pp. 453-469, 2018.

[49] F. Bonnardot, R. Randall, J. Antoni, and F. Guillet, "Enhanced unsupervised noise cancellation using angular resampling for planetary bearing fault diagnosis," *International journal of acoustics and vibration,* vol. 9, pp. 51-60, 2004.

[50] L. F. Villa, A. Reñones, J. R. Peran, and L. J. de Miguel, "Statistical fault diagnosis based on vibration analysis for gear test-bench under non-stationary conditions of speed and load," *Mechanical Systems and Signal Processing,* vol. 29, pp. 436-446, 2012.

[51] Z. Feng and M. Liang, "Fault diagnosis of wind turbine planetary gearbox under nonstationary conditions via adaptive optimal kernel time–frequency

analysis," *Renewable Energy,* vol. 66, pp. 468-477, 2014.

[52] X. Chen and Z. Feng, "Time-frequency analysis of torsional vibration signals in resonance region for planetary gearbox fault diagnosis under variable speed conditions," *IEEE Access,* vol. 5, pp. 21918-21926, 2017.

[53] Y. Jiang, B. Tang, Y. Qin, and W. Liu, "Feature extraction method of wind turbine based on adaptive Morlet wavelet and SVD," *Renewable energy,* vol. 36, pp. 2146-2153, 2011.

[54] W. Liu, W. Zhang, J. Han, and G. Wang, "A new wind turbine fault diagnosis method based on the local mean decomposition," *Renewable Energy,* vol. 48, pp. 411-415, 2012.

[55] J. Park, M. Hamadache, J. M. Ha, Y. Kim, K. Na, and B. D. Youn, "A positive energy residual (PER) based planetary gear fault detection method under variable speed conditions," *Mechanical Systems and Signal Processing,* vol. 117, pp. 347-360, 2019.

[56] Z. Feng, X. Lin, and M. J. Zuo, "Joint amplitude and frequency demodulation analysis based on intrinsic time-scale decomposition for planetary gearbox fault diagnosis," *Mechanical Systems and Signal Processing,* vol. 72, pp. 223-240, 2016.

[57] Z. Feng, H. Ma, and M. J. Zuo, "Amplitude and frequency demodulation analysis for fault diagnosis of planet bearings," *Journal of Sound and Vibration,* vol. 382, pp. 395-412, 2016.

[58] Y. Li, K. Feng, X. Liang, and M. J. Zuo, "A fault diagnosis method for planetary gearboxes under non-stationary working conditions using improved Vold-Kalman filter and multi-scale sample entropy," *Journal of Sound and Vibration,* vol. 439, pp. 271-286, 2019.

[59] Z. Liu, Y. Jin, M. J. Zuo, and Z. Feng, "Time-frequency representation based on robust local mean decomposition for multicomponent AM-FM signal analysis," *Mechanical Systems and Signal Processing,* vol. 95, pp. 468-487, 2017.

[60] T. Wang, Q. Han, F. Chu, and Z. Feng, "A new SKRgram based demodulation technique for planet bearing fault detection," *Journal of Sound and Vibration,* vol. 385, pp. 330-349, 2016/12/22/ 2016.

[61] Z. Feng and M. Liang, "Complex signal analysis for planetary gearbox fault diagnosis via shift invariant dictionary learning," *Measurement,* vol. 90, pp. 382-395, 2016/08/01/ 2016.

[62] J. Park, Y. Kim, K. Na, and B. D. Youn, "Variance of energy residual (VER): An efficient method for planetary gear fault detection under variable-speed conditions," *Journal of Sound and Vibration,* 2019/04/11/ 2019.

[63] J.-R. R. Ruiz, J. A. Rosero, A. G. Espinosa, and L. Romeral, "Detection of demagnetization faults in permanent-magnet synchronous motors under nonstationary conditions," *IEEE Transactions on Magnetics,* vol. 45, pp. 2961-2969, 2009.

[64] B. Boashash, L. Boubchir, and G. Azemi, "A methodology for time-frequency image processing applied to the classification of non-stationary multichannel signals using instantaneous frequency descriptors with application to newborn EEG signals," *EURASIP Journal on Advances in Signal Processing,* vol. 2012, p. 117, 2012.

[65] B. Boashash and S. Ouelha, "Automatic signal abnormality detection using time-frequency features and machine learning: A newborn EEG seizure case study," *Knowledge-Based Systems,* vol. 106, pp. 38-50, 2016.

[66] B. Boashash, H. Barki, and S. Ouelha, "Performance evaluation of time-frequency image feature sets for improved classification and analysis of non-stationary signals: Application to newborn EEG seizure detection," *Knowledge-Based Systems,* vol. 132, pp. 188-203, 2017.

[67] S. Altunay, Z. Telatar, and O. Erogul, "Epileptic EEG detection using the linear prediction error energy," *Expert Systems with Applications,* vol. 37, pp. 5661-5665, 2010.

[68] A. Subasi, E. Erçelebi, A. Alkan, and E. Koklukaya, "Comparison of subspace-based methods with AR parametric methods in epileptic seizure detection," *Computers in Biology and Medicine,* vol. 36, pp. 195-208, 2006.

[69] B. Boashash, N. A. Khan, and T. Ben-Jabeur, "Time–frequency features for pattern recognition using high-resolution TFDs: A tutorial review," *Digital Signal Processing,* vol. 40, pp. 1-30, 2015.

[70] R. M. Haralick and K. Shanmugam, "Textural features for image classification," *IEEE Transactions on systems, man, and cybernetics,* pp. 610-621, 1973.

[71] T. Ahonen, A. Hadid, and M. Pietikainen, "Face description with local binary patterns: Application to face recognition," *IEEE Transactions on Pattern Analysis & Machine Intelligence,* pp. 2037-2041, 2006.

[72] Y. LeCun, Y. Bengio, and G. Hinton, "Deep learning," *nature,* vol. 521, p. 436, 2015.

[73] I. Goodfellow, Y. Bengio, and A. Courville, *Deep learning*: MIT press, 2016.

[74] I. Goodfellow, J. Pouget-Abadie, M. Mirza, B. Xu, D. Warde-Farley, S. Ozair*, et al.*, "Generative adversarial nets," in *Advances in neural information processing systems*, 2014, pp. 2672-2680.

[75] J. Schmidhuber, "Deep learning in neural networks: An overview," *Neural networks,* vol. 61, pp. 85-117, 2015.

[76] L. Deng and D. Yu, "Deep learning: methods and applications," *Foundations and Trends® in Signal Processing,* vol. 7, pp. 197-387, 2014.

[77] C. Dong, C. C. Loy, K. He, and X. Tang, "Learning a deep convolutional network for image super-resolution," in *European conference on computer vision*, 2014, pp. 184-199.

[78] P. Sermanet, D. Eigen, X. Zhang, M. Mathieu, R. Fergus, and Y. LeCun,

"Overfeat: Integrated recognition, localization and detection using convolutional networks," *arXiv preprint arXiv:1312.6229,* 2013.

[79] Y. LeCun and Y. Bengio, "Convolutional networks for images, speech, and time series," *The handbook of brain theory and neural networks,* vol. 3361, p. 1995, 1995.

[80] M. M. Bronstein, J. Bruna, Y. LeCun, A. Szlam, and P. Vandergheynst, "Geometric deep learning: going beyond euclidean data," *IEEE Signal Processing Magazine,* vol. 34, pp. 18-42, 2017.

[81] M. Zhao, M. Kang, B. Tang, and M. Pecht, "Deep residual networks with dynamically weighted wavelet coefficients for fault diagnosis of planetary gearboxes," *IEEE Transactions on Industrial Electronics,* vol. 65, pp. 4290-4300, 2018.

[82] H. Oh, J. H. Jung, B. C. Jeon, and B. D. Youn, "Scalable and unsupervised feature engineering using vibration-imaging and deep learning for rotor system diagnosis," *IEEE Transactions on Industrial Electronics,* vol. 65, pp. 3539-3549, 2018.

[83] C. Li, R.-V. Sánchez, G. Zurita, M. Cerrada, and D. Cabrera, "Fault diagnosis for rotating machinery using vibration measurement deep statistical feature learning," *Sensors,* vol. 16, p. 895, 2016.

[84] L. Jing, M. Zhao, P. Li, and X. Xu, "A convolutional neural network based feature learning and fault diagnosis method for the condition monitoring of

gearbox," *Measurement,* vol. 111, pp. 1-10, 2017.

[85] L. Jing, T. Wang, M. Zhao, and P. Wang, "An adaptive multi-sensor data fusion method based on deep convolutional neural networks for fault diagnosis of planetary gearbox," *Sensors,* vol. 17, p. 414, 2017.

[86] W. Bartelmus, F. Chaari, R. Zimroz, and M. Haddar, "Modelling of gearbox dynamics under time-varying nonstationary load for distributed fault detection and diagnosis," *European Journal of Mechanics - A/Solids,* vol. 29, pp. 637-646, 2010.

[87] F. Chaari, M. S. Abbes, F. V. Rueda, A. F. del RINCON, and M. Haddar, "Analysis of planetary gear transmission in non-stationary operations," *Frontiers of Mechanical Engineering,* vol. 8, pp. 88-94, 2013.

[88] W. Kim, J. Y. Lee, and J. Chung, "Dynamic analysis for a planetary gear with time-varying pressure angles and contact ratios," *Journal of Sound and Vibration,* vol. 331, pp. 883-901, 2012.

[89] A. Hammami, A. Fernández, F. Chaari, F. Viadero, and M. Haddar, "Dynamic behaviour of two stages planetary gearbox in non-stationary operations," in *Surveillance 7 conference (Oct 2013)*, 2013.

[90] A. F. D. R. A. Hammami, F. Chaari, F. Viadero Rueda and M. Haddar, "Dynamic Behaviour of Back to Back Planetary Gear in Run Up and Run Down Transient Regimes," *Journal of Mechanics,* vol. 31, pp. 481-491, 2015.

[91] P. Srikanth and A. Sekhar, "Dynamic analysis of wind turbine drive train subjected to nonstationary wind load excitation," *Proceedings of the Institution of Mechanical Engineers, Part C: Journal of Mechanical Engineering Science,* vol. 229, pp. 429-446, 2015.

[92] Y. Fang, X. Liang, and M. J. Zuo, "Effect of sliding friction on transient characteristics of a gear transmission under random loading," in *2017 IEEE International Conference on Systems, Man, and Cybernetics (SMC)*, 2017, pp. 2551-2555.

[93] J. T. Yoon, B. D. Youn, M. Yoo, and Y. Kim, "A newly formulated resilience measure that considers false alarms," *Reliability Engineering & System Safety,* vol. 167, pp. 417-427, 2017/11/01/ 2017.

[94] J. H. Jung, B. C. Jeon, B. D. Youn, M. Kim, D. Kim, and Y. Kim, "Omnidirectional regeneration (ODR) of proximity sensor signals for robust diagnosis of journal bearing systems," *Mechanical Systems and Signal Processing,* vol. 90, pp. 189-207, 2017/06/01/ 2017.

[95] J. M. Ha, H. Oh, J. Park, and B. D. Youn, "Classification of operating conditions of wind turbines for a class-wise condition monitoring strategy," *Renewable Energy,* vol. 103, pp. 594-605, 2017/04/01/ 2017.

[96] D. W. Kim, H. Oh, B. D. Youn, and D. Kwon, "Bivariate Lifetime Model for Organic Light-Emitting Diodes," *IEEE Transactions on Industrial Electronics,* vol. 64, pp. 2325-2334, 2017.

[97] T. Kim, H. Oh, H. Kim, and B. D. Youn, "An Online-Applicable Model for Predicting Health Degradation of PEM Fuel Cells With Root Cause Analysis," *IEEE Transactions on Industrial Electronics,* vol. 63, pp. 7094-7103, 2016.

[98] H. Oh, S. Choi, K. Kim, B. D. Youn, and M. Pecht, "An empirical model to describe performance degradation for warranty abuse detection in portable electronics," *Reliability Engineering & System Safety,* vol. 142, pp. 92-99, 2015/10/01/ 2015.

[99] C. Hu, B. D. Youn, T. Kim, and P. Wang, "A co-training-based approach for prediction of remaining useful life utilizing both failure and suspension data," *Mechanical Systems and Signal Processing,* vol. 62–63, pp. 75-90, 10// 2015.

[100] H. Oh, B. Han, P. McCluskey, C. Han, and B. D. Youn, "Physics-of-Failure, Condition Monitoring, and Prognostics of Insulated Gate Bipolar Transistor Modules: A Review," *IEEE Transactions on Power Electronics,* vol. 30, pp. 2413-2426, 2015.

[101] M. Lebold, K. McClintic, R. Campbell, C. Byington, and K. Maynard, "Review of vibration analysis methods for gearbox diagnostics and prognostics," in *Proceedings of the 54th meeting of the society for machinery failure prevention technology*, 2000, p. 16.

[102] P. Večeř, M. Kreidl, and R. Šmíd, "Condition indicators for gearbox condition monitoring systems," *Acta Polytechnica,* vol. 45(6), pp. 35-43,

2005.

[103] J. J. Zakajsek, "A review of transmission diagnostics research at NASA Lewis Research Center," 1994.

[104] A. Aherwar and M. S. Khalid, "Vibration analysis techniques for gearbox diagnostic: a review," *International Journal of Advanced Engineering Technology,* vol. 3, pp. 04-12, 2012.

[105] M. Mosher, A. Pryor, and E. M. Huff, "Evaluation of standard gear metrics in helicopter flight operation," 2002.

[106] O. D. Mohammed, M. Rantatalo, and J.-O. Aidanpää, "Dynamic modelling of a one-stage spur gear system and vibration-based tooth crack detection analysis," *Mechanical Systems and Signal Processing,* vol. 54–55, pp. 293-305, 2015.

[107] X. Fan and M. J. Zuo, "Gearbox fault detection using Hilbert and wavelet packet transform," *Mechanical Systems and Signal Processing,* vol. 20, pp. 966-982, 2006.

[108] S. Choi and C. J. Li, "Estimation of gear tooth transverse crack size from vibration by fusing selected gear condition indices," *Measurement Science and Technology,* vol. 17, pp. 2395-2400, 2006.

[109] S. Sheng, "Investigation of various condition monitoring techniques based on a damaged wind turbine gearbox," National Renewable Energy Lab.(NREL), Golden, CO (United States)2011.

[110] M. K. Kıymık, İ. Güler, A. Dizibüyük, and M. Akın, "Comparison of STFT and wavelet transform methods in determining epileptic seizure activity in EEG signals for real-time application," *Computers in biology and medicine,* vol. 35, pp. 603-616, 2005.

[111] M. Inalpolat and A. Kahraman, "A theoretical and experimental investigation of modulation sidebands of planetary gear sets," *Journal of Sound and Vibration,* vol. 323, pp. 677-696, 2009.

[112] J. Urbanek, T. Barszcz, M. Straczkiewicz, and A. Jablonski, "Normalization of vibration signals generated under highly varying speed and load with application to signal separation," *Mechanical Systems and Signal Processing,* vol. 82, pp. 13-31, 2017.

[113] Z. Feng and M. J. Zuo, "Fault diagnosis of planetary gearboxes via torsional vibration signal analysis," *Mechanical Systems and Signal Processing,* vol. 36, pp. 401-421, 4// 2013.

[114] L. Liu, X. Liang, and M. J. Zuo, "Vibration signal modeling of a planetary gear set with transmission path effect analysis," *Measurement,* vol. 85, pp. 20-31, 2016.

[115] R. Uma Maheswari and R. Umamaheswari, "Trends in non-stationary signal processing techniques applied to vibration analysis of wind turbine drive train – A contemporary survey," *Mechanical Systems and Signal Processing,* vol. 85, pp. 296-311, 2017.

[116] J. Shi, M. Liang, and Y. Guan, "Bearing fault diagnosis under variable rotational speed via the joint application of windowed fractal dimension transform and generalized demodulation: A method free from prefiltering and resampling," *Mechanical Systems and Signal Processing,* vol. 68–69, pp. 15-33, 2// 2016.

[117] V. Sharma and A. Parey, "Frequency domain averaging based experimental evaluation of gear fault without tachometer for fluctuating speed conditions," *Mechanical Systems and Signal Processing,* vol. 85, pp. 278-295, 2017/02/15/ 2017.

[118] V. Sharma and A. Parey, "Gear crack detection using modified TSA and proposed fault indicators for fluctuating speed conditions," *Measurement,* vol. 90, pp. 560-575, 2016/08/01/ 2016.

[119] V. Sharma and A. Parey, "Gearbox fault diagnosis using RMS based probability density function and entropy measures for fluctuating speed conditions," *Structural Health Monitoring,* vol. 16, pp. 682-695, 2017/11/01 2016.

[120] S. Mallat, *A wavelet tour of signal processing*, 3rd ed.: Academic press, 2009.

[121] C. Wang, R. X. Gao, and R. Yan, "Unified time–scale–frequency analysis for machine defect signature extraction: Theoretical framework," *Mechanical Systems and Signal Processing,* vol. 23, pp. 226-235, 2009.

[122] Z. K. Peng and F. L. Chu, "Application of the wavelet transform in machine

condition monitoring and fault diagnostics: a review with bibliography," *Mechanical Systems and Signal Processing,* vol. 18, pp. 199-221, 2004.

[123] R. Q. Yan, R. X. Gao, and X. F. Chen, "Wavelets for fault diagnosis of rotary machines: A review with applications," *Signal Processing,* vol. 96, pp. 1-15, 2014.

[124] J. L. Chen, Z. P. Li, J. Pan, G. G. Chen, Y. Y. Zi, J. Yuan*, et al.*, "Wavelet transform based on inner product in fault diagnosis of rotating machinery: A review," *Mechanical Systems and Signal Processing,* vol. 70-71, pp. 1-35, 2016.

[125] J. Singh, A. K. Darpe, and S. P. Singh, "Rolling element bearing fault diagnosis based on Over-Complete rational dilation wavelet transform and auto-correlation of analytic energy operator," *Mechanical Systems and Signal Processing,* vol. 100, pp. 662-693, 2/1/ 2018.

[126] J. Yuan, Y. Wang, Y. Peng, and C. Wei, "Weak fault detection and health degradation monitoring using customized standard multiwavelets," *Mechanical Systems and Signal Processing,* vol. 94, pp. 384-399, 9/15/ 2017.

[127] C. Mishra, A. K. Samantaray, and G. Chakraborty, "Rolling element bearing defect diagnosis under variable speed operation through angle synchronous averaging of wavelet de-noised estimate," *Mechanical Systems and Signal Processing,* vol. 72–73, pp. 206-222, 5// 2016.

[128] L. Meng, J. Xiang, Y. Wang, Y. Jiang, and H. Gao, "A hybrid fault diagnosis

method using morphological filter–translation invariant wavelet and improved ensemble empirical mode decomposition," *Mechanical Systems and Signal Processing,* vol. 50–51, pp. 101-115, 1// 2015.

[129] W. Q. Wang, F. Ismail, and M. F. Golnaraghi, "Assessment of gear damage monitoring techniques using vibration measurements," *Mechanical Systems and Signal Processing,* vol. 15, pp. 905-922, 2001.

[130] S. Abbasion, A. Rafsanjani, A. Farshidianfar, and N. Irani, "Rolling element bearings multi-fault classification based on the wavelet denoising and support vector machine," *Mechanical Systems and Signal Processing,* vol. 21, pp. 2933-2945, 2007.

[131] Q. Hu, Z. J. He, Z. S. Zhang, and Y. Y. Zi, "Fault diagnosis of rotating machinery based on improved wavelet package transform and SVMs ensemble," *Mechanical Systems and Signal Processing,* vol. 21, pp. 688-705, 2007.

[132] J. D. Wu and C. H. Liu, "An expert system for fault diagnosis in internal combustion engines using wavelet packet transform and neural network," *Expert Systems with Applications,* vol. 36, pp. 4278-4286, 2009.

[133] N. Saravanan and K. I. Ramachandran, "Incipient gear box fault diagnosis using discrete wavelet transform (DWT) for feature extraction and classification using artificial neural network (ANN)," *Expert Systems with Applications,* vol. 37, pp. 4168-4181, 2010.

[134] C. E. Rasmussen, *Gaussian processes for machine learning* vol. 1. Cambridge, Massachusetts, London, England: The MIT Press, 2006.

[135] P. Boškoski, M. Gašperin, D. Petelin, and Đ. Juričić, "Bearing fault prognostics using Rényi entropy based features and Gaussian process models," *Mechanical Systems and Signal Processing,* vol. 52–53, pp. 327-337, 2// 2015.

[136] D. An, N. H. Kim, and J.-H. Choi, "Practical options for selecting data-driven or physics-based prognostics algorithms with reviews," *Reliability Engineering & System Safety,* vol. 133, pp. 223-236, 1// 2015.

[137] S. Choi, M. Jadaliha, J. Choi, and S. Oh, "Distributed gaussian process regression under localization uncertainty," *Journal of Dynamic Systems, Measurement, and Control,* vol. 137, p. 031007, 2015.

[138] D. Kwon, M. H. Azarian, and M. Pecht, "Remaining-Life Prediction of Solder Joints Using RF Impedance Analysis and Gaussian Process Regression," *IEEE Transactions on Components, Packaging and Manufacturing Technology,* vol. 5, pp. 1602-1609, 2015.

[139] P. Boškoski, M. Gašperin, D. Petelin, and Đ. Juričić, "Bearing fault prognostics using Rényi entropy based features and Gaussian process models," *Mechanical Systems and Signal Processing,* vol. 52–53, pp. 327-337, 2// 2015.

[140] I. Bilionis and N. Zabaras, "Multi-output local Gaussian process regression:

Applications to uncertainty quantification," *Journal of Computational Physics,* vol. 231, pp. 5718-5746, 7/1/ 2012.

[141] T. E. Fricker, J. E. Oakley, N. D. Sims, and K. Worden, "Probabilistic uncertainty analysis of an FRF of a structure using a Gaussian process emulator," *Mechanical Systems and Signal Processing,* vol. 25, pp. 2962-2975, 11// 2011.

[142] M. S. Kan, A. C. C. Tan, and J. Mathew, "A review on prognostic techniques for non-stationary and non-linear rotating systems," *Mechanical Systems and Signal Processing,* vol. 62-63, pp. 1-20, 2015.

[143] W. J. Wang and P. D. Mcfadden, "Application of orthogonal wavelets to early gear damage detection," *Mechanical Systems and Signal Processing,* vol. 9, pp. 497-507, 1995.

[144] D. Iatsenko, P. V. E. McClintock, and A. Stefanovska, "Extraction of instantaneous frequencies from ridges in time–frequency representations of signals," *Signal Processing,* vol. 125, pp. 290-303, 2016.

[145] J. J. Włodarz, "On marginalization of phase-space distribution functions," *Physics Letters A,* vol. 264, pp. 18-21, 1999.

[146] A. Aissa-El-Bey, N. Linh-Trung, K. Abed-Meraim, A. Belouchrani, and Y. Grenier, "Underdetermined blind separation of nondisjoint sources in the time-frequency domain," *IEEE Transactions on Signal Processing,* vol. 55, pp. 897-907, 2007.

[147] D. Wang, W. T. Peter, and K. L. Tsui, "An enhanced Kurtogram method for fault diagnosis of rolling element bearings," *Mechanical Systems and Signal Processing,* vol. 35, pp. 176-199, 2013.

[148] J. Antoni and R. B. Randall, "The spectral kurtosis: application to the vibratory surveillance and diagnostics of rotating machines," *Mechanical Systems and Signal Processing,* vol. 20, pp. 308-331, 2006.

[149] P. H. Westfall, "Kurtosis as peakedness, 1905–2014. RIP," *The American Statistician,* vol. 68, pp. 191-195, 2014.

[150] Y. Wang, J. Xiang, R. Markert, and M. Liang, "Spectral kurtosis for fault detection, diagnosis and prognostics of rotating machines: A review with applications," *Mechanical Systems and Signal Processing,* vol. 66–67, pp. 679-698, 1// 2016.

[151] C. Jinglong, Z. Yanyang, H. Zhengjia, and Y. Jing, "Improved spectral kurtosis with adaptive redundant multiwavelet packet and its applications for rotating machinery fault detection," *Measurement Science and Technology,* vol. 23, p. 045608, 2012.

[152] J. Antoni, "Fast computation of the kurtogram for the detection of transient faults," *Mechanical Systems and Signal Processing,* vol. 21, pp. 108-124, 1// 2007.

[153] J. Antoni, "The spectral kurtosis: a useful tool for characterising non-stationary signals," *Mechanical Systems and Signal Processing,* vol. 20, pp.

282-307, 2// 2006.

[154] A. Zisserman. Lecture 2: 2D Fourier transforms and applications in Image Analysis [Online]. Available: http://www.robots.ox.ac.uk/~az/lectures/ia/lect2.pdf

[155] Q. Kemao, "Two-dimensional windowed Fourier transform for fringe pattern analysis: principles, applications and implementations," *Optics and Lasers in Engineering,* vol. 45, pp. 304-317, 2007.

국문 초록

시간-주파수 기법을 활용한 변속 조건 유성기어의 고장 진단 기법 개발

유성기어의 갑작스러운 고장은 큰 재산 피해뿐만 아니라 인명 손실을 일으킬 수 있다. 그래서, 최근 유성기어의 고장을 진단하기 위한 많은 연구들이 수행되어 왔다. 기존의 연구들은 유성기어가 일정한 속도하에서 운행된다는 가정을 바탕으로 하고 있다. 하지만 실제 현장에서의 유성기어는 다양한 변속 조건에서 운행된다. 이 논문에서는 변속조건의 유성기어에도 적용이 가능한 고장 진단법을 개발하고자 한다. 개발 고장 진단법은 시간에 따른 유성기어의 주파수 거동을 살펴보기 위해 시간-주파수 기법을 이용한다. 시간-주파수 기법을 이용하여 고장 진단법을 개발하는데 있어서 1) 고장 민감도, 2) 알고리즘 계산 시간, 3) 복잡한 속도 조건 의 어려움이 존재한다. 이 논문에서는 이러한 어려움을 극복하기 위해 세가지 연구 주제를 제안한다. 먼저, 첫 번째 연구 주제에서는 민감도가 향상된 고장 진단 기술을 개발하고자 한다. 제안 방법은 시간-주파수 기법을 이용하여 변속 조건에서 오는 영향도를 최소화함으로써 고장 진단법의 민감도를 향상시키고자 하였다. 또한, 시간 주파수 분석 결과에서 있는 고장 신호를 강조함으로써 민감도를

더욱 높였다. 두번째 연구주제에서는 기존 방법 대비 알고리즘 계산 시간을 줄이고자 하였다. 그래서, 계산 시간이 상대적으로 적게 걸리는 시간-주파수 방법을 사용하였다. 하지만 해당 방법은 기존 방법 대비 고장 민감도가 감소한다는 단점이 있다. 그래서 신호와 시스템의 특징을 활용함으로써 줄어든 민감도를 보상하는 기법을 개발하였다. 세번째 연구 주제에서는 속도 조건에 관계없이 고장 관련 성분을 추출할 수 있는 특질 인자를 개발하였다. 해당 방법에서는 시간-주파수 이미지 데이터로부터 고장으로 인해 발생한 성분만을 추출하게 된다. 그래서 추출된 인자는 고장 외의 다른 성분에는 영향을 받지 않는다. 그러므로 해당 고장 특질인자는 복잡한 속도 조건을 갖는 유성기어에 적용 가능하다. 제안 방법은 해석 모델로부터 얻은 유성 기어 신호와 실험으로부터 측정된 유성 기어 신호를 이용하여 검증하였다. 이 논문에서 제안된 제안된 동기, 고장 민감도 향상, 알고리즘 계산 시간, 복잡한 운행 조건에 맞게 변속 조건의 유성기어에 적용될 수 있을 것이다.

주제어: 고장 진단
유성 기어
변속 조건
시간-주파수 분석
신호 분석
고장 예측 및 관리

학 번: 2012-23166

This research is supported by the International Research & Development Program of the National Research Foundation of Korea funded by the Ministry of Science, ICT & Future Planning (Grant number: 2017K1A3A1A12034682).